The GFDL Variable-Resolution Global Chemistry-Climate Model for Research at the Nexus of US Climate and Air Quality Extremes

Meiyun Lin[1*], Larry W. Horowitz[1], Ming Zhao[1], Lucas Harris[1], Paul Ginoux[1], John Dunne[1], Sergey Malyshev[1], Elena Shevliakova[1], Hamza Ahsan[2], Steve Garner[1], Fabien Paulot[1], Arman Pouyaei[3], Steven J. Smith[2], Yuanyu Xie[4], Niki Zadeh[1], Linjiong Zhou[3]

[1] NOAA Geophysical Fluid Dynamics Laboratory, Princeton, NJ, USA
[2] Joint Global Change Research Institute, Pacific Northwest National Laboratory, College Park, MD, USA
[3] Cooperative Institute for Modeling the Earth System, Princeton University, Princeton, NJ, USA
[4] Princeton School of Public and International Affairs, Princeton University, Princeton, NJ, USA

*Corresponding author: Meiyun Lin (Meiyun.Lin@noaa.gov)

AGU Journal of Advances in Modeling Earth Systems, submitted on August-21-2023, revised on Dec 4th, 2023, https://doi.org/10.1029/2023MS003984

Key Points:

1) A new variable-resolution global chemistry-climate model has been developed for research at the nexus of US climate and air quality extremes
2) This model unifies component advances in physics, chemistry and land-atmosphere interactions within a seamless variable-resolution framework
3) This model features much improved US regional precipitation, drought, and air quality extremes compared to previous models

Abstract. We present a variable-resolution global chemistry-climate model (AM4VR) developed at NOAA's Geophysical Fluid Dynamics Laboratory (GFDL) for research at the nexus of US climate and air quality extremes. AM4VR has a horizontal resolution of 13 km over the US, allowing it to resolve urban-to-rural chemical regimes, mesoscale convective systems, and land-surface heterogeneity. With the resolution gradually reducing to 100 km over the Indian Ocean, we achieve multi-decadal simulations driven by observed sea surface temperatures at 50% of the computational cost for a 25-km uniform-resolution model. In contrast with GFDL's AM4.1 contributing to the sixth Coupled Model Intercomparison Project at 100-km resolution, AM4VR features much improved US climate mean patterns and variability. In particular, AM4VR shows improved representation of: precipitation seasonal-to-diurnal cycles and extremes, notably reducing the central US dry-and-warm bias; western US snowpack and summer drought, with implications for wildfires; and the North American monsoon, affecting dust storms. AM4VR exhibits excellent representation of winter precipitation, summer drought, and air pollution meteorology in California with complex terrain, enabling skillful prediction of both extreme summer ozone pollution and winter haze events in the Central Valley. AM4VR also provides vast improvements in the process-level representations of biogenic volatile organic compound emissions, interactive dust emissions from land, and removal of air pollutants by terrestrial ecosystems. We highlight the value of increased model resolution in representing climate–air quality interactions through land-biosphere feedbacks. AM4VR offers a novel opportunity to study global dimensions to US air quality, especially the role of Earth system feedbacks in a changing climate.

Plain Language Summary. NOAA's Geophysical Fluid Dynamics Laboratory has developed a new variable-resolution global chemistry-climate model for research at the nexus of US climate and air quality extremes. In contrast with the global models contributing to the latest Intergovernmental Panel on Climate Change Report, this model features more than 10 times finer spatial resolution over the contiguous US, allowing it to better resolve cities, mountain valleys, thunderstorms, and urban-to-rural air quality variations. This model features much improved representation of regional rainfall extremes, drought, and severe air pollution events in diverse US air basins, including California. Notably, this model reduces the central US dry-and-warm bias that has persisted in many generations of climate models. As global climate change leads to more hot and dry weather, the resulting droughts are creating dust-prone bare lands or stressing plants, making them less able to remove ozone pollution from the air. These effects are included in this model, with particular focus on integrating physical, chemical, and biological components at high spatial resolution to understand Earth system feedbacks to US air quality extremes in a changing climate.

1. Introduction

Earth system interactions of air quality with weather and climate operate across time scales from hours to decades and across spatial scales from hundreds of meters to thousands of kilometers. Climate change influences air quality globally, including by altering the frequency, severity, and duration of air stagnation events, heat waves, precipitation, and other meteorology conducive to pollutant accumulation in populated regions [e.g., Fiore et al., 2015]. In particular, compound heatwaves and drought events exacerbate air pollution through land-biosphere feedbacks, such as reducing ozone removal by drought-stressed vegetation [e.g. Lin et al., 2019; Lin et al., 2020], increasing wildfire and dust emissions [Xie et al., 2022; Pu et al., 2022; Yu et al., 2022], and altering biogenic volatile organic compound (BVOC) emissions from plants [Sharkey and Monson, 2014; Lin et al., 2017]. Some regions may be particularly vulnerable to large feedbacks from natural sources of aerosol and ozone precursors, such as semi-arid western US regions with topography ranging from below sea level to over 4 km above sea level. Representing Earth system feedbacks requires advances in current global chemistry-climate models, especially increased coupling and interactivity of atmospheric composition with the biosphere, improved representation of surface heterogeneity in land-atmosphere coupling, and increased resolution to better represent extreme heat, drought and air pollution events in regions over complex terrain. Here we aim to address these challenges by integrating physical, chemical, and biological components in a variable-resolution global chemistry-climate model.

In the US, air pollution regulation is complicated by contributions from multiple sources including background sources like stratospheric ozone intrusions, dust storms, wildfires, transported pollution, and biogenic precursors, in addition to US anthropogenic sources [Lin et al., 2012ab; Ginoux et al., 2012; US EPA 2016; Lin et al., 2017; Jaffe et al., 2018]. Air pollution events are often initiated by changes in large-scale atmospheric dynamics that can be resolved by global models, but assessing their ultimate impacts on surface air quality requires high-resolution models. For example, model resolution plays a critical role in representing: the fine-scale filamentary structure of the stratospheric ozone intrusions that penetrate deeper into the troposphere [Lin et al., 2012a; Lin et al., 2015; Langford et al., 2017; Zhang et al., 2020]; the offshore downslope Santa Ana and Diablo winds that often result in increased wildfire danger in California [Mass and Owen, 2019; Goss et al., 2020]; and ozone pollution episodes caused by the complex chemical mixing of wildfire plumes with urban emissions in intermountain valleys [Jaffe et al., 2020] and by lake breezes at coastal counties around Lake Michigan [Dye et al., 1995; Stanier et al., 2021]. High-resolution models are also needed to better represent

surface heterogeneity of dust source locations, surface wind gusts and mesoscale convective systems that trigger extreme dust storms such as haboobs [Ginoux et al, 2012; UNEP 2016; Kim et al., 2017].

Home to over 39 million people and America's most productive farmlands surrounded by mountain ranges, California is particularly susceptible to extreme climate and air pollution events [OEHHA 2022]. Despite decades of progress in air quality regulation, ozone is still among the most widespread and significant air pollution health threats in California. Seven of the ten cities in the US with the worst ozone pollution were consistently in California during the last decade [American Lung Association, 2023]. Not only notorious for ozone pollution, California's Bakersfield, Visalia, and Fresno in the Central Valley also ranked the top three cities in the US with the highest year-round concentration of $PM_{2.5}$ (American Lung Association, 2023). With more frequent hot and dry weather expected in the coming decades [e.g., Lau et al., 2012], accurate projection of future air quality in California can provide valuable information to air quality managers as they develop abatement strategies. However, current global chemistry-climate models typically have a spatial resolution of 100–300 km in the atmosphere [Thornhill et al., 2021], too coarse to resolve diverse air basins in California and other US regions, limiting their usefulness for local and regional policymakers.

Statistical downscaling has been widely used to refine projections of future climate, but it requires the assumption that the statistical relationships used to transform global climate model fields during a historical period hold for the novel environments under climate change ("stationarity"), of which the validity is difficult to assess [Lanzante et al., 2018]. High-resolution regional models such as the Weather Research & Forecasting model with Chemistry (WRF-Chem) and the Community Multiscale Air Quality Modeling System (CMAQ) [US EPA 2022] provide an alternate approach, but they require prescribed atmospheric boundaries from other models. There are substantial issues with imposing global model boundary conditions in a regional model, due to inconsistencies in the physical and chemical schemes and vertical resolution among models, and the neglect of climate feedbacks from regional environments to the global system [e.g., Lin et al., 2009; Lin et al., 2010; Gao et al., 2013; Pfister et al., 2014; Hogrefe et al., 2018; Liu et al., 2018]. Furthermore, regional air quality models typically rely on prescribed vegetation characteristics (e.g., Foroutan et al., 2017), limiting their ability to study the impacts of future climate change on vegetation dynamics and feedbacks to air quality. Accurate projection of future climate and air quality at scales relevant to local and regional stakeholders requires a seamless modeling system that can provide detailed information over a targeted region, while still integrating the global Earth system components in a computationally efficient manner.

Continuing increases in computing power have enabled development of global high-resolution (25-50 km) physical climate models, which have been shown to improve representation of atmospheric rivers and rainfall extremes [e.g., Roberts et al., 2020; Haarsma et al., 2020; Zhao, 2022; Jong et al., 2023]. However, accurately simulating the central US warm-season precipitation and its diurnal cycle remains a serious challenge, even in models at 25 km resolution [e.g., Tang et al., 2019; Dong et al., 2023]. These physical climate models typically have minimal representation of aerosols by prescribing ozone and other oxidants, but avoid the high computational cost of interactive atmospheric chemistry. The desire to maintain both comprehensive chemistry and high resolution for air quality research has motivated several variable-resolution model development efforts. The US National Center for Atmospheric Research (NCAR) is developing the Multi-Scale Infrastructure for Chemistry and Aerosols (MUSICA) using the spectral element dynamical core [Pfister et al., 2020]. With horizontal winds and temperature nudged to reanalysis, Schwantes et al. [2022] and Tang et al. [2023] evaluated several

one-year simulations of MUSICA version 0 with 32 vertical layers and horizontal mesh refinement down to 14 km over the continental US (CONUS). GEOS-Chem, a global chemical transport model with prescribed meteorology, recently has also developed grid-stretching capability [Bindle et al., 2021]. These short-term simulations with nudged or prescribed meteorology have demonstrated the value of regional grid refinement for simulating atmospheric trace constituents.

Here we present multi-decadal simulations of a new variable-resolution global chemistry-climate model developed at NOAA's Geophysical Fluid Dynamics Laboratory (GFDL AM4VR), with particular focus on integrating physical, chemical, and biological components for research at the nexus of US climate and air quality extremes. AM4VR builds upon a variable-resolution version of the GFDL Finite–Volume Cubed-Sphere Dynamical Core (FV3) with regional grid refinements of 13 km over CONUS [*Harris et al., 2016*] and the GFDL AM4.1 global chemistry-climate models with 49 vertical levels [*Horowitz et al., 2020*]. Many global and regional atmospheric chemistry models calculate dry deposition of gases to vegetation using the Wesely (1989) scheme, which does not account for stomatal closure induced by soil drying or rising atmospheric CO_2 concentrations [Rydsaa et al., 2016; Kavassalis et al., 2017; Galmarini et al., 2021]. In contrast, AM4VR incorporates a new mechanistic scheme with dry deposition of ozone, reactive nitrogen, and their precursors responding to hydroclimate and photosynthesis in a dynamic vegetation land model [Lin et al., 2019], which has been shown to improve representation of ozone extremes during drought and of climate-driven surface ozone trends [*Lin et al., 2020*]. AM4VR also includes substantial improvements in the representation of interactive BVOC emissions, the response of dust emissions to dynamic vegetation cover, and wildfire plume chemistry and injection height. Development of such a comprehensive model, with meteorology-chemistry coupling, feedbacks, and interactions across space and time is particularly challenging.

The focus of the present study is to provide an overview of the AM4VR performance in AMIP (Atmospheric Model Intercomparison Project) mode, driven by observed sea surface temperature (SST) and sea ice distributions, historical anthropogenic emissions, land use and atmospheric radiative forcing agents over 1988-2020. Section 2 provides a detailed description of the grid structure, physical and chemical model formulations, and forcing datasets as distinguished from the AM4.1 configuration used in simulations for the sixth Coupled Model Intercomparison Project (CMIP6) [Horowitz et al., 2020]. In Section 3, we evaluate the physical climate simulation with AM4VR: including global distributions of precipitation patterns and radiative fluxes, and surface air temperature, drought, and rainfall extremes over the US. After a brief evaluation of atmospheric composition simulation (Section 4), we then focus our analysis on US climate–air quality interactions (Section 5). We summarize in Section 6 the strengths and potential applications of AM4VR and discuss future development plans.

2. Model Description

2.1 Grid Structure

[Figure 1 about here]

AM4VR is built using the GFDL FV3 Dynamical Core [Putman and Lin 2007] on a stretched c256 grid [Harris et al. 2016; Harris et al., 2019; Zhou et al., 2019], providing a horizontal resolution of approximately 13 km over the contiguous US (**Fig.1**). In contrast with AM4.1 using the c96 (~100 km) uniform-resolution grid, AM4VR features eight times finer horizontal resolution over the contiguous US,

allowing it to better resolve cities, mountain-valleys, urban-to-rural chemical regimes, mesoscale convective systems, fire weather and air pollution meteorology over California's complex terrain (**Fig.S1**). With the resolution gradually reducing to 100 km over the Indian Ocean on the opposite face of the FV3 cube, we achieve computational efficiency for seamless assessment across daily to multi-decadal time scales. In contrast with the C384 (25 km) uniform-resolution grid, AM4VR shows 50% reduction of computational burden while doubling resolution over North America (Supporting **Text S1**). In contrast with MUSICA-v0 [Schwantes et al., 2022; Tang et al., 2023], which has a horizontal resolution of 14 km over the contiguous US, quickly transitioning to 111 km over the rest of the globe, AM4VR with the FV3 dynamical core features a less radically-stretched grid structure with resolution gradually reducing from 13 km over CONUS to 25-50 km over Europe, 50-100 km over Asia, and 100 km over the Indian Ocean. This allows for better representation of the general circulation and upstream chemical processes over much of the Earth, and a less-severe discontinuity outside of the highest-resolution region.

AM4VR uses an update to the GFDL Land Model version 4.0 that was used as the land component in the AM4.0 physical climate and aerosol model [Zhao et al., 2018ab] for CMIP6 simulations, not the GFDL Land Model version 4.1 used by the full-chemistry AM4.1 atmospheric model [Horowitz et al., 2020] and the ESM4.1 coupled Earth System Model [Dunne et al., 2020]. The land model employs the same grid structure as the atmospheric model, but represents small-scale heterogeneity of land surface cover in each grid cell using a mosaic approach, with a combination of subgrid tiles in four land use categories: lands undisturbed by human activity (i.e., "natural"), lands harvested at least once (i.e., "secondary"), croplands, and pastures [Shevliakova et al., 2009; Malyshev et al., 2015; **Fig.S2**]. Transitions among the four land-use types are prescribed from the historical reconstruction at 0.25^{o}x0.25^{o} resolution used in CMIP6 [Hurtt et al., 2020]. Land initial conditions for AM4VR are remapped from GFDL's seasonal prediction model at 25 km resolution [Delworth et al., 2020]. The time step for atmospheric chemistry and physics and land is reduced from 30 min in AM4.1 to 10 min in AM4VR for increased numerical stability.

For this study, we evaluate the AMIP configuration of AM4VR and document the differences in results between AM4VR and two uniform-resolution C96 AMIP experiments: (1) The CMIP6 configuration of AM4.1; (2) An experiment with emissions, atmospheric chemistry, land model component, and dry deposition schemes updated as in AM4VR (Sections 2.3-2.5), but retaining the physical model formulation as in AM4.1 (Section 2.2). To demonstrate the benefit of refining the model resolution from 25 to 13 km, we also analyze a 7-year C384 uniform-resolution experiment. Table S1 provides a list of model experiments analyzed in this study.

2.2 Physical Model Formulation

The physical formulation of AM4VR is similar to that of AM4.1, but with some changes in the configuration of the dynamical core and physics retuning for the convection scheme and cloud microphysics. Our goal and tuning strategy for AM4VR is to achieve marked improvements in mean climate and variability over the US, while maintaining a good simulation of global-scale circulation and climate comparable to AM4.1 at C96 resolution. One significant change in the configuration of the dynamics in AM4VR is the use of a fourth-order divergence damping rather than the sixth-order damping used in AM4.0 and AM4.1. Increased divergence damping in the model can result in increased tropical cyclone frequency, decreased convective updrafts, and a broadened precipitation distribution and larger

extreme values [Zhao et al., 2012; Anber et al., 2018]. Using lower-order divergence damping is more justifiable for higher-resolution simulations to reduce grid-scale noise, enhance numerical stability, and improve the simulation of organized convection [Zhao, 2022]. The vertical resolution of AM4VR is the same as that for AM4.1, including 49 vertical levels, ranging in thickness from 30 m near the Earth's surface to 1-1.5 km near the tropopause and 2-3 km in much of the stratosphere with model top at 1 Pa (~80 km altitude). Unlike in AM4.1, a sponge layer extending down to 15 Pa is applied in the top five model layers in AM4VR to control numerical noise for increased stability [Harris et al., 2021].

Since a model's ability to accurately simulate the global distribution of precipitation given observed sea ice and SST distributions is important to the model's overall quality in simulating the atmospheric general circulation, temperature, clouds, vegetation, and sources and sinks of atmospheric pollutants, we have considered it as a high priority during model development. In principle, it would be preferable to resolve convective precipitation rather than rely on parameterization. But given that AM4VR's resolution, even over North America, is still too coarse to resolve deep convection, it must still rely on convective parameterization to some extent. In an initial 10-year AMIP simulation with AM4VR before any retuning of the physics from the AM4.1 settings, precipitation shifted markedly from parameterized to resolved-scale (explicit) convection due to the increased resolution over North America. We find this deteriorates model-simulated mean climate because excessive resolved-scale convection tends to distort convection towards unrealistically large scales. Over the southeast US during summer, for example, the fraction of resolved-scale precipitation increases from ~42% in AM4.1 to ~81% in this initial AM4VR simulation, with simulated precipitation peaking at nighttime as opposed to the observed afternoon peak. These results are broadly consistent with many prior studies suggesting that the model-simulated mean state can deteriorate dramatically when parameterized deep convection is overly inhibited [Zhao et al., 2018b, Freitas et al., 2020, and references therein], highlighting the need for further work on scale-aware convection as well as the explicit cloud parameterization.

We are able to ameliorate some of these issues by retuning several of the moist physics parameterizations. Specifically, we increase parameterized precipitation in AM4VR by modifying the strength of the deep plume lateral mixing rate in the double plume convection scheme (ε_1 in Equation 1 of Zhao et al., 2018b). We conduct two 10-year AMIP sensitivity simulations (2008-2017) with ε_1 decreasing from the AM4.1 default value of 0.9 km^{-1} to 0.7 and 0.5 km^{-1}, and evaluate the global distribution of precipitation and radiation at the top of the atmosphere (TOA) with observational estimates. **Fig.S3** shows comparisons of US annual precipitation patterns and seasonal cycles. As ε_1 decreases to 0.5 km^{-1}, the fraction of large-scale precipitation over the Southeast US during June-September decreases to 60%, compared to 81% with ε_1 = 0.9 km^{-1} (72% with ε_1 = 0.7 km^{-1}), along with reductions in wintertime precipitation, leading to marked improvements in the simulated precipitation season cycle (r^2 = 0.86 versus 0.60). A lower ε_1 value generally decreases US land precipitation, reducing the wet bias in the Southeast while increasing the dry bias in the central US during nighttime. The deep plume lateral mixing rate also influences model-simulated tropical transient activity, which decreases with increased convective parameterization [Zhao et al., 2018b]. We choose to use ε_1 = 0.5 km^{-1} as our baseline model configuration for AM4VR, but also discuss results from an alternate configuration with ε_1 = 0.6 km^{-1} in Sections 3 and 4, after compromising between the mean state and internal atmospheric variability.

We also adjust a liquid cloud microphysics parameter, referred to as the critical cloud drop radius (r_{thresh}), above which liquid water in large-scale clouds is converted to rain [Golaz et al., 2013]. For a given cloud

liquid water content and droplet number, an increase of r_{thresh} makes it harder for the liquid cloud to precipitate and therefore increases cloud liquid water content, especially in the extratropics where large-scale stratiform clouds dominate. We increase r_{thresh} from 8.5 μm in AM4.1 to 9.5 μm in AM4VR, which is more consistent with satellite observations [Suzuki et al., 2013], to reduce positive biases in net shortwave downward radiative flux in AM4VR.

2.3 Atmospheric Chemistry, Aerosol, and Vegetation Feedbacks

AM4VR includes interactive tropospheric and stratospheric gas-phase and aerosol chemistry. The bulk aerosol scheme includes 18 transported aerosol tracers, and the gas-phase chemistry scheme represents the NO_x–HO_x–O_x–CO–VOCs system with ~100 chemical tracers, 190 gas-phase kinetic reactions, 43 photolysis reactions, and 15 heterogeneous reactions [Horowitz et al., 2020]. Heterogeneous chemistry is slightly updated from AM4.1. AM4VR corrects an error in the simulated hygroscopic growth of the surface area of organic aerosols. The reaction probabilities (γ values) of N_2O_5 and NO_3 on aerosol surfaces have been reduced from their values in AM4.1, from γN_2O_5=0.02 to 0.01, and γNO_3=0.02 to 0.001, on the basis of recent observational data (see Table S1 of Holmes et al., 2019). The optical properties of aerosol, extinction efficiency, single scattering albedo and asymmetry parameter, are calculated at 40 wavelengths from 174 nm to 40 micrometers using a Mie code (**Text S2**).

One significant change in the configuration of atmospheric chemistry for AM4VR is the use of an interactive dry deposition scheme, coupled to dynamic vegetation in LM4.0, for reactive nitrogen species [Paulot et al., 2018], SO_2, volatile organic compounds (VOCs), and ozone [Lin et al., 2019; Lin et al., 2020]. Unlike AM4VR, dry deposition velocities for all gases in AM4.1 are prescribed from a monthly climatology [Silva & Heald, 2018]. AM4VR includes a mechanistic simulation of tracer dry deposition to vegetation depending on photosynthesis, soil water stress, atmospheric CO_2 concentration and vapor pressure deficit [Lin et al., 2019; 2020]. The scheme includes a correction to double counting of reduced stomatal deposition on the wet part of the leaf noted by Clifton et al. [2020]. The LM4.0 dry deposition scheme described in Lin et al. [2019, 2020] was driven by observation-based atmospheric forcings, and used the CMIP5 settings for soil types, soil parameter values, and land use. The scheme in the AM4VR configuration instead uses the LM4.0 CMIP6 settings and is coupled to the atmospheric model. This enables investigation of how the improved representation of precipitation and drought influences air quality simulation through land-biosphere feedbacks.

Dust emissions are calculated dynamically online in the land component, LM4.0. The emissions and dry deposition of dust are calculated separately on each sub-grid tile (i.e. pasture, cropland, natural and secondary vegetation) of LM4.0. Net dust flux (emission minus deposition) is transferred to the atmosphere through the model's coupler. Dust emission is initiated when the surface wind speed reaches a specified minimum threshold necessary to start the sand blasting process lifting clay and silt particles. Dust emission is parameterized following Ginoux et al. (2001) with adaptation to the GFDL previous version of the dynamic land model LM3 by Evans et al. (2016). To consider the preferential location of dust sources in topographic depressions, dust emission is proportional to the source function S (Eq. 1 of Ginoux et al., 2001). The threshold of wind erosion is minimum for dry and bare surfaces, and is given a specific value for each land use type. Higher values are used for cropland (6 m/s) and pasture (4 m/s) compared to natural and secondary vegetation (1 m/s) to consider surface littering by agricultural waste. Surface bareness is assumed to decrease exponentially as the sum of the Leaf Area

Index (LAI) and ten times the Stem Area Index (SAI) increases, with maximum values of LAI (0.2) and SAI (0.015), beyond which emissions are completely suppressed. Dust emissions are also suppressed when the following parameters exceed the stated maximum values: snow cover (0.01 kg/m^2), soil wetness (0.3) and soil iceness (0.025) averaged over the first 15 cm below the surface. Note that our simulations do not include scaling of the threshold wind velocity with soil moisture (Ginoux et al., 2001, Eq. 3), beyond the soil wetness threshold mentioned above. Following Kok et al. (2014), the soil mass fraction in AM4VR is distributed with mass fraction of 0.05, 0.15, 0.3, 0.27 and 0.23 for the size classes 0.1-1 μm, 1-2 μm, 2-3 μm, 3-6 μm, and 6-10 μm, respectively. The dimensional global emission factor C (Eq. 2 of Ginoux et al., 2001) has been increased to 2.5 μg s^{-2} m^{-5} in AM4VR from 1.0 μg s^{-2} m^{-5} in Ginoux et al. [2001] to improve agreement of simulated surface concentrations with observations. **Table S2** provides a list of dust model parameters in AM4VR and C96 calculated from LM4.0, in comparison to those in AM4.1/LM4.1.

Lightning NO emissions are calculated interactively as a function of subgrid convection in the model, as diagnosed by the double-plume convection scheme (Zhao et al., 2018b). A shift from parameterized convective precipitation to resolved large-scale precipitation with increasing grid resolution poses a challenge for estimating lightning flash rate and lightning NO emission in a variable-resolution model. We were able to ameliorate this issue by using a global scaling factor to have AM4VR produce a similar magnitude of total lightning NO emissions over North America as in AM4.1. The global total production of NO by lightning is 3.26 TgN/yr (400.5 GgN/yr over North America) in AM4.1 and 4.28 TgN/yr (375.1 GgN/yr over North America) in AM4VR (**Fig.S4**). The larger production of lightning NO in AM4VR is located around the Indian Ocean, which has little direct impact on air quality episodes in the US but may have some influence on the global background ozone by modulating methane lifetime. We find that the methane lifetime against loss by reaction with tropospheric OH is 0.5 years shorter in AM4VR than AM4.1 (**Fig.S5**). Future development efforts should include a scale-aware lightning parameterization to account for the shift from parameterized to resolved convective updrafts as the model resolution increases. At high spatial resolutions, scaling using a "calibration factor" such as proposed by Price and Rind (1994) is insufficient to account for resolved-scale convection. Instead, a scale-aware lightning parameterization may be approached by comparing grid-box mean vertical pressure velocities (omega) and the parameterized convective mass fluxes. As the model resolution increases, the grid-box mean vertical pressure velocities increase while parameterized convective mass flux decreases. One can use vertical pressure velocity to determine the magnitude and depth of resolved-scale convection. The hydrometeor contents and convective available potential energy can be combined with the convective depth to infer the lightning parameterization associated with resolved-scale convection.

2.4 Interactive BVOC Emissions

Biogenic emissions of isoprene and monoterpenes are calculated online using the PCEEA (Parameterized Canopy Environment Emission Activity) algorithm [Guenther et al., 2006] in the Model of Emissions of Gases and Aerosols from Nature (MEGAN v2.1; Guenther et al., 2012) as a function of emission potentials, land cover, leaf area index, and simulated air temperature and shortwave radiative fluxes. In this work, we implement high-resolution emission potential (EP) data and satellite-derived land cover maps to improve representation of urban-to-rural variations in BVOC emissions. The vegetation types and leaf area indices used in MEGAN are independent of those simulated by the LM4.0 dynamic vegetation model, due to a lack of urban land use in LM4.0 and a lack of coupling between the

dynamic vegetation properties simulated by LM4.0 and the atmospheric emissions module. MEGAN has three options for EP definition: (1) EP maps at 0.5°x0.5° resolution for five vegetation types: needle trees, broadleaf trees, crops, shrubs, and grass [Emmons et al., 2010]; (2) EP calculated from prescribed Plant Functional Type (PFT) distributions with each of the 16 MEGAN PFTs assigned a single emission factor value regardless of species composition; (3) detailed EP maps with high spatial resolution (1x1 km^2), combining information on land cover, species composition with species-specific emission factors, and above-canopy flux measurements where available [Guenther et al., 2012]. The second option, with EP calculated from PFT coverage, is inaccurate, especially for broadleaf deciduous forest, which can consist of tree species such as maples, which are low isoprene emitters, and tree species such as oaks, which are strong isoprene emitters. AM4.1 adopted the first option for isoprene and the second option for monoterpene emissions.

We have made the following changes to the original implementation of MEGAN2.1 in GFDL models described by Rasmussen et al. [2012]: (1) fixing an error in the mapping of PFT distributions to croplands and shrublands for calculating isoprene emissions with the first EP definition option adopted by AM4.1; (2) updating global PFT data from 0.5°x0.5° to 3min x 3min spatial resolution [https://bai.ess.uci.edu/megan/data-and-code/megan21]; (3) modifying codes to allow land cover change using inter-annually varying PFT and LAI datasets; (4) including the CO_2 inhibition effect on isoprene emissions [Possell and Hewitt 2011; Tai et al.,2013]; (5) implementing global 0.1°x0.1° MODIS LAI data reprocessed to mitigate noise and gaps [Yuan et al., 2011; 2020]; (6) using different factors for direct (4.0 μmol photons per Joule) and diffuse light (4.6 μmol photons per Joule) to convert solar radiation in W m^{-2} to Photosynthetic Photon Flux Density in μmol photons m^{-2} s^{-1} [Guenther et al., 2012]; (7) implementing an additional algorithm to use detailed EP maps (i.e., the third EP option) for isoprene and the main monoterpenes (α-pinene, β-pinene, myrcene, sabinene, limonene, trans-β-ocimene, Δ^3-carene; https://bai.ess.uci.edu/megan/data-and-code/megan21; all monoterpene emissions are treated as α-pinene in the chemistry scheme). The AM4VR simulations in the present study adopt this new algorithm (third EP option) for both isoprene and monoterpene emission calculations. Updates (1) to (3) implemented for the first EP option are not used in the AM4VR simulations presented here, but these updates will allow future efforts to explore the role of land cover changes. All input datasets are regridded to the model grid during runtime using a conservative remapping approach.

[Figures 2 and 3 about here]

Figure 2a-b displays comparisons of MEGAN isoprene emission fluxes over CONUS computed in the AMIP simulations with AM4.1 and AM4VR. AM4VR calculates 50-80% lower isoprene emissions over crop-dominated regions, such as the Central Valley of California, the US Great Plains and Midwest regions (**Fig.2a-b**), the North China Plain, northern India, and central Europe (**Fig.S6**). The higher isoprene emissions over these regions estimated by AM4.1 is caused by mis-assigning the EP values between croplands and shrublands. The PFT mapping fix reduces isoprene emissions by ~50% in the cropland dominated regions and by ~20% globally in AM4.1 (**Fig.S6**). The global total isoprene emissions from vegetation are 491.5 Tg/yr in AM4.1 and 336.3 Tg/yr in AM4VR for the 2000-2014 period **(Fig.S6)**. Another major difference between AM4.1 and AM4VR is the Southeast US isoprene emission maximum, which is focused in the Upper South (Kentucky/Virginia) and the Ozark Plateau (Missouri) in AM4.1, while AM4VR simulates elevated emissions extending to the Deep South. Comparison with a high-resolution (0.25°x0.3125°) inversion of OMI (Ozone Monitoring Instrument) HCHO columns available for the Southeast US in August-September 2013 [Kaiser et al., 2018] shows that simulated isoprene emissions from AM4VR exhibit significant spatial coherence with the OMI-based estimates on

ecosystem-relevant scales (**Fig.3**). Total isoprene emissions for the Southeast US in August-September 2013 are 2.3 TgC from the OMI inversion and 2.7 TgC in AM4VR, while emissions in AM4.1 (4.5 TgC) are too high by a factor of 2. The spatial difference in simulated isoprene emissions between AM4.1 and AM4VR partly reflects the difference in the fraction of broadleaf deciduous trees in the underlying land use datasets for MEGAN. AM4.1 uses the PFT distributions from the NCAR Community Land Model, while the land cover dataset used to generate detailed EP maps for AM4VR adjusts vegetation coverage using ground truth data from the US Forest Service [Millet et al., 2008].

Figure 2c-d compares biogenic emissions of monoterpenes computed in AM4.1 with EP calculated from PFT coverage and in AM4VR with EP detailed maps accounting for species composition. AM4VR calculates higher monoterpene emissions from western Ponderosa Pine forests and midwestern American Elm forests, while estimating lower emissions from subtropical forests in the Southeast. The global total emissions of monoterpenes from vegetation are 132 Tg/yr in AM4.1 and 96 Tg/yr in AM4VR **(Fig.S7).** Lower monoterpenes emissions calculated in AM4VR for the tropics are consistent with the findings of Sindelarova et al. [2022], who showed that α-pinene emissions calculated from the PFT coverage are 70% higher when compared to emissions calculated from the EP maps. Emissions of other BVOCs from vegetation are also updated (**Fig.2e-f, Fig.S8, and Text S3**). AM4VR assumes a 5% per-carbon yield of secondary organic aerosols (SOA) from biogenic isoprene emissions, decreased from 10% in AM4.1. The SOA yield from monoterpenes is the same (10%) between AM4.1 and AM4VR. In the longer-term, we would like to implement a process-based scheme to allow coupling between anthropogenic and biogenic emissions for biogenic SOA production [e.g., Zheng et al., 2023].

2.5 Anthropogenic and Biomass Burning Emissions

[Figure 4 about here]

We implement new high-resolution datasets for anthropogenic emissions in AM4VR. Interannually varying time series of monthly anthropogenic emissions at 0.1° x 0.1° horizontal resolution for the period 1980-2020 are obtained from the Community Emissions Data System (CEDS) version 2021-04-21 (https://doi.org/10.25584/PNNLDataHub/1779095). The AM4.1 CMIP6 simulations used anthropogenic emissions from an earlier version (v2017-05-18) of CEDS [Hoesly et al., 2018]. Notably, the new CEDS inventory estimates strong reductions of emissions in China for SO_2 since 2005, NO_x since 2011, and organic matter (OM) and black carbon (BC) aerosols since 2000 (**Fig.4a-d**), consistent with emission control regulations and broader technological changes in China (e.g. fuel shifts away from biofuels in the residential sector and closing of traditional beehive coke ovens) [Zhang et al., 2017; McDuffie et al., 2020; Kanaya et al., 2020]. In the US, total anthropogenic NMVOCs emissions considered in AM4VR are higher than AM4.1 by 17% during the 2000-2014 period (**Fig.4e**). While the differences between the two CEDS inventories for the other US emissions are small, we find that estimates of US anthropogenic OM emissions from the EPA National Emission Inventory for 2017 (NEI2017) are two times higher than the CEDS estimates (purple star versus green lines in Fig.4b). This will be discussed further in Section 4 when evaluating model simulations of organic aerosols.

Interannually varying time series of monthly biomass burning emissions in AM4VR for 1997-2020 are from the Global Fire Emission Database version 4 with small fires (GFED4s) at 0.25°x0.25° resolution (https://www.globalfiredata.org/). Biomass burning emissions before 1997 are from the data set of van Marle et al. [2017] developed in support of CMIP6, as used in the AM4.1 CMIP6 simulations. Wildfire emissions in AM4VR are distributed vertically between the surface and 6 km, with seasonally and

geographically varying, biome-dependent (0.25°x0.25°) wildfire smoke injection heights derived from space-based multi-angle imaging (MISR 2008-2010; Val Martin et al., 2018), different from the six biome-specific vertical profiles of Dentener et al. [2006] used in AM4.1. In North America during summer, the percentage of total wildfire emissions injected above 2 km altitude in AM4VR is 25-50% over boreal forests, 10-25% over temperate forests, 5-10% over grasslands, and 1-5% over croplands, compared to 60% north of 45°N (0% south of 45°N) over North America for all seasons in AM4.1. MISR provides more realistic spatiotemporal variation of wildfire smoke injection heights, although we acknowledge that the 10:30 AM MISR overpass is well before the afternoon peak in fire activity at most locations, so may underestimate injection heights. To account for rapid chemistry in fire plumes, we use recent field measurements of western US fire plumes [Calahorrano et al., 2021, Xu et al., 2021] to partition oxidized reactive nitrogen (NO_y) emissions from biomass burning into PAN (37%), NO (36%), and HNO_3 (27%) in AM4VR, rather than emitting only NO as in AM4.1. While observations show enhancements in particulate nitrate with nearly no enhancement in nitric acid (HNO_3) [Calahorrano et al., 2021], HNO_3 and aerosol nitrate are repartitioned basically instantaneously through the ISORROPIA thermodynamic model [Fountoukis & Nenes, 2007]. The NO_y partitioning reduces excessive ozone production close to the fires while increasing their downwind impact. Other updates, including changes in biomass burning emissions of oxygenated VOCs (**Fig.4f**), alkanes, alkenes (**Fig.S9**), and SOA yield, are described in **Text S4**.

3. Results: Physical Climate Simulation

3.1 Global Distributions of Precipitation and Radiation

[Figures 5 about here]

We examine the role of model resolution on physical climate simulation given observed SSTs by comparing the AM4VR and C96 AMIP experiments with the same configuration of land, atmospheric chemistry and aerosol forcings (**Table S1**). **Figure 5a-f** shows the comparison of long-term annual mean precipitation from AM4VR and C96 with observational estimates from the Global Precipitation Climatology Project (GPCP v2.3) at 1°x1° resolution [Adler et al. 2003] and the Integrated Multi-satellitE Retrievals for Global Precipitation Measurement (IMERG) at 0.1°x0.1° resolution [Huffman et al., 2019]. The global areal mean, the Pearson pattern correlation coefficient (*r*), and overall root mean square errors (*RMSE*) against GPCP estimates are slightly degraded in AM4VR versus C96, but there are significant improvements in simulated precipitation on regional scales. The most notable improvements in AM4VR (with ε_1 = 0.5 km^{-1}) relative to C96 (with ε_1 = 0.9 km^{-1}) are a reduction of excessive precipitation bias over the Philippine Sea and a reduction of dry bias across the equatorial Indian Ocean to Western Indonesia and over the Gulf of Mexico and the US Great Plains, the South Atlantic Convergence Zone, and the Southeast Amazon. A slight degradation of the wet bias is found in parts of the Maritime Continent and Central America, although some of the discrepancies may reflect limitations of the coarse-resolution GPCP data in resolving precipitation in regions with complex geographical features. Supporting this statement, the IMERG satellite product at 0.1°x0.1° resolution estimates higher precipitation in these regions than GPCP. The simulated differences in regional precipitation reflect the combined effects of higher spatial resolution and physics retuning in AM4VR, modulating the partitioning of total precipitation between parameterized deep convective precipitation and resolved large-scale precipitation, along with associated changes in atmospheric circulation (**Fig.5g-h**). The zonal mean ratio of parameterized convective to total precipitation in the tropics (20°S-

20°N) decreases from 0.66 in C96 to 0.61 in AM4VR with ε_1 = 0.5 km^{-1} and to 0.57 with ε_1 = 0.6 km^{-1} (**Fig.S10**), bringing it closer to ~0.45 from satellite estimates [Chen et al., 2021].

[Figure 6 about here]

We evaluate patterns of TOA longwave, shortwave, and net radiation fluxes in comparison with satellite estimates (CERES EBAF Edition 4.2; Loeb et al., 2018; https://ceres.larc.nasa.gov/). Comparison of TOA outgoing longwave radiation (**Fig.6a-b**) illustrates a low spatial bias and RMSE with a similar pattern to AM4.0 and AM4.1 at C96 resolution reported previously [Zhao et al., 2018a; Horowitz et al., 2020]. Comparison of TOA shortwave absorption and net radiation (**Fig.6c-f**) exhibits reduced bias (10-20 W/m^2 compared to 20-60 W/m^2 in AM4.1) over the ocean in the California, Peru, and Benguela Eastern Boundary Current regions, demonstrating encouraging ability of AM4VR in developing marine stratus clouds with implications for coastal fog formation in these regions [Torregrosa et al., 2014]. A slight degradation is found around the Maritime Continent and over the Southern Ocean, causing an increase of overall RMSE from 7.73 W/m^2 in C96 to 8.80 W/m^2 in AM4VR for shortwave absorption. Over North America, AM4VR shows slightly larger positive biases (< 10 W/m^2) than C96 against satellite estimates of shortwave absorption (**Fig.6c-d**), consistent with the difference in shortwave cloud radiative effects (**Fig.S13**). For these initial AMIP applications we have not made substantial efforts to retune clouds to improve radiative fluxes; such improvements would be essential before using this atmospheric model for coupled ocean-atmosphere simulations. Changes in the deep plume mixing rate have a minor impact on the radiation metrics as scored with the global RMSE (**Figs.S11-S13).** Comparison of annual mean 2m temperature over land with observations illustrates a notable reduction of warm bias over North America in AM4VR, with the geographical pattern of bias for the other regions and overall RMSE similar to the C96 simulation (**Fig.S14**).

3.2 US Precipitation, Snowpack, Temperature and Extremes

[Figure 7 about here]

In this section, we discuss more detailed evaluation of AM4VR performance in mean-state physical climate and extremes over CONUS. Our analyses leverage the high-resolution (4x4 km^2), observation-based estimates of precipitation and 2m temperature over CONUS from PRISM (Parameter-elevation Regressions on Independent Slopes Model) [Daly et al., 2021]. With regional grid refinements to 13 km over CONUS, AM4VR demonstrates marked improvements upon C96 (100 km) resolution in resolving the spatial structure of precipitation over the Cascades – Sierra Nevada Mountains, across the Intermountain West and the Great Plains, in the Northeast, and over the Deep South and the Gulf of Mexico (Fig.7). The Pearson pattern correlation coefficient with observed annual mean precipitation across the US increases from 0.85 in C96 to 0.93 in AM4VR and the overall RMSE decreases from 0.64 mm day^{-1} in C96 to 0.47 mm day^{-1} in AM4VR. The statistics from evaluating seasonal mean precipitation show a similar degree of improvement (**Figs.S15-S18)**. The most notable difference from C96 to AM4VR is an improvement in the dry bias over the central US that has persisted in many generations of weather forecast and climate models [e.g., Y. Lin et al., 2017; Morcrette et al. 2018; Zhang et al., 2018; Sun and Liang, 2023], including the 4th generation of GFDL models participating in CMIP6 [Zhao et al., 2018ab; Horowitz et al., 2020]. AM4VR is able to completely remove the dry bias in the southern Great Plains for spring and fall (**Figs.S15-S17**). During summer (**Fig.S18**), the improvement is noticeable throughout the Great Plains.

[Figure 8 about here]

The majority of annual precipitation in the western US accumulates between November and March, falling as snow in the mountains. We evaluate western US snowpack in March, which plays a critical role in regional hydroclimate, water supply, and wildfire risk in the warm seasons [e.g., Westerling et al., 2006]. We use a 0.25^{o}x0.25^{o} gridded snowpack observation product created by Kapnick et al. [2018] using the monthly first-of-the-month snowpack observations from 1136 stations over 1981-2016. Comparison of March Snow Water Equivalent (SWE) values in **Fig.8** clearly illustrates the improved simulation of snowpack climatology with increasing model resolution, also noted by Kapnick et al. [2018] who compared models at 25 km, 50 km, and 200 km resolution. At 100 km resolution, the narrow mountain ranges of the Washington-Oregon Cascades and Sierra Nevada are not resolved; mountains in the Northern Rockies are smoothed and low (**Fig.S1**), resulting in an underestimated snowpack. AM4VR at 13 km resolution better reproduces fine-scale mountain features with snowpack values approaching observations.

[Figure 9 about here]

Figure 9 shows the seasonal cycle of regional precipitation in the central US (38-50°N, 102-87°W), the Southeast (25-40°N, 90-75°W), the Cascades (38-49°N, 124.5-121.0°W), and the Southwest US (29-40°N, 120-102°W). AM4VR exhibits improved skill in simulating the seasonal cycle of precipitation in all of the key regions, owing to improved representation of mesoscale convective systems and increases in resolved-scale precipitation. AM4VR captures better intense precipitation during the cold seasons (November-March) and drought conditions during the warm seasons (June-September) over the Pacific Northwest (**Fig.9a**). The correlation r^2 between observed and predicted monthly precipitation increases from 0.10 in C96 to 0.85-0.92 in AM4VR for the Southwest, from 0.46 to 0.87-0.93 for the central US, and from 0.24 to 0.7-0.83 for the Southeast (**Fig.9b-d**).

[Figure 10 about here]

Analysis of daily precipitation distribution demonstrates reduced “drizzling” bias (too frequent light precipitation) and increased regional rainfall extremes (**Fig.10a-d**). Compared to C96, precipitation in AM4VR shows a considerable upward shift toward the high tail in the probability density function (PDF) distribution of daily precipitation. Rather than sampling daily precipitation on each grid for the PDF analysis, we have chosen to sample regionally averaged precipitation for each day, as this approach better reflects large-scale controls of precipitation variability and thus is more process-oriented. The median value of daily precipitation averaged over the central US increases from 0.8 mm/day in C96 to 2.0 mm/day in AM4VR, compared with 2.2 mm/day in PRISM observations. The 90th percentile of daily precipitation averaged over the Southeast increases from 6.4 mm/day in C96 to 7.8 mm/day in AM4VR, compared with 8.4 mm/day in PRISM observations.

Comparison of precipitation over the Southwest demonstrates the skill of AM4VR in representing the North American Monsoon, a seasonal change in the atmospheric circulation that brings moisture from the Pacific Ocean and the Gulf of California, resulting in thunderstorms and heavy rains in northwestern Mexico, Arizona, and New Mexico from July to mid-September. Comparison of monthly precipitation climatology over the Southwest reveals a 37% increase in precipitation from resolved mesoscale convective systems (i.e., organized thunderstorms) during July-September in AM4VR when compared to the model at C96 resolution (**Fig.9b**). The C96 model has difficulty simulating the springtime dryness and captures only 27% of summertime monsoon rainfall. The 90th percentile of daily precipitation averaged over the Southwest is 3.4 mm/day in observations and 3.3 mm/day in AM4VR with $\varepsilon_1 = 0.6$ km^{-1}, increasing from 1.8 mm/day in C96 (**Fig.10b**). The impacts of the monsoon go beyond just rainfall

amounts. One recent study found that monsoon rains were important for ending wildfires [Arizpe et al., 2020]. The improved representation of mesoscale convective systems and hydroclimate in the Southwest US also has implications for simulation of dust storms, which we will discuss in Section 5.

In **Fig.10e-f**, we compare the diurnal cycle of warm-season precipitation in the Central and the Southeast US, respectively, from IMERG observations [Huffman et al., 2019] and AM4 simulations at 100 km, 25 km, and 13 km resolution. Over the Central US during summer, eastward-propagating mesoscale convective systems and the low-level jet stream from the Gulf of Mexico bring moisture and precipitation late at night and in the early morning hours according to observations [Schumacher and Rasmussen, 2020]. For comparison, the observed precipitation in the Southeast is driven primarily by the ubiquitous late afternoon thunderstorms and deep convection. Many generations of weather forecasting and climate models fail to simulate the observed nocturnal peak of warm-season precipitation in the Central US [e.g., Y. Lin et al., 2017; Zhao et al., 2018a; Morcrette et al. 2018]. Recently, Tang et al. (2019, 2023) showed that the Department of Energy E3SM model with regional grid refinement of 25 km showed little improvement in the Central US precipitation dry bias. During our AM4VR development process, we find it challenging to accurately simulate the diurnal cycle of precipitation in the Central and the Southeast US simultaneously without a smooth transition between parameterized and resolved-scale convection. For the Southeast, AM4VR at 13 km resolution with ε_1 = 0.5 or 0.6 km^{-1} simulates a local noon peak of precipitation (dominated by parameterized convection) similar to the C96 (100 km) model with ε_1 = 0.9 km^{-1} and the C384 (25 km) model with ε_1 = 0.7 km^{-1}. They all peak too early compared to observations, as in many other climate models [e.g., Dai, A 2006, Lee et al., 2007; Dong et al., 2023]. Over the Central US, increasing resolution from 100 km to 25 km exhibits encouraging skills with simulated precipitation shifting towards nighttime but the magnitude is too weak compared to observations. Doubled resolution in AM4VR brings it closer to observations, increasing nocturnal precipitation in the Central US by ~35% from the 25 km model, while maintaining a comparable diurnal cycle in the Southeast.

[Figure 11 about here]

Reducing the intensity of parameterized convection by increasing ε_1 from 0.5 to 0.6 km^{-1} in AM4VR leads to improved simulation of precipitation in most US regions except for the Southeast (orange versus red lines in **Figs.9-10**). AM4VR with ε_1 = 0.6 km^{-1} simulates increased mean precipitation and larger extreme values over the Southwest during the North American monsoon season. Over the central US in JJAS, a precipitation dry bias exceeding 1 mm/day in the C96 model spans a large area extending across the Great Plains to the Deep South and the Gulf of Mexico. In contrast, the dry bias is confined to the southern Great Plains in AM4VR with ε_1 = 0.5 km^{-1} and further reduced to a smaller area in parts of Texas and Oklahoma with ε_1 = 0.6 km^{-1} (**Fig.11a**). Although AM4VR shows a reduction of dry bias over Florida compared to C96, increasing ε_1 from 0.5 to 0.6 km^{-1} in AM4VR shows little improvement over Florida where late afternoon deep convection occurs at much smaller scales and so needs to be parameterized. Global and regional mean precipitation are also subject to large-scale energy constraints; therefore, their regional distribution is challenging to model and will not simply follow changes in cumulus mixing rate.

Over the Pacific Northwest and California, AM4VR shows improvements upon C96 in representing summer drought. **Fig.11b** compares annual consecutive dry days (CDD), defined as the maximum number of consecutive days with precipitation less than 1 mm at each grid. At C96 resolution, the model underestimates CDD in the Pacific Northwest and has difficulty resolving the observed peak of CDD in

the Central Valley of California. AM4VR with ε_1 = 0.5 km^{-1} captures the spatial structure but overestimates CDD in northern California. AM4VR with ε_1 = 0.6 km^{-1} best represents the spatial variations of CDD over California, with more severe drought conditions developed in the San Joaquin Valley in the south than the Sacramento Valley in the north, consistent with observations.

[Figure 12 about here]

Comparison of JJAS mean daily maximum 2m temperature (T_{max}) shows a reduction of the warm bias from ~4 ºC in C96 to ~1 ºC in AM4VR with ε_1 = 0.6 km^{-1} over the central US, coinciding with a reduction of precipitation dry bias (**Fig.12**). Over the Pacific Northwest, the improved representation of summer drought in AM4VR leads to better representation of summer T_{max}. The Pearson pattern correlation with observed T_{max} across CONUS increases from 0.83 to 0.92 and overall RMSE decreases from 2.49 to 1.72. At 13 km resolution, AM4VR better resolves sharp temperature gradients in western US regions with complex terrain. However, a warm bias of 2–4 ºC in JJAS daily T_{max} is found in the Central Valley of California and the Snake River Plain in Idaho. A similar warm bias in the Central Valley was found in a variable-resolution version of the Community Earth System Model [Huang et al., 2016; Z. Xu et al., 2021]. The warm bias over the western US in AM4VR is consistent with overall larger positive bias, compared to C96 against satellite estimates in TOA net shortwave absorption and shortwave cloud radiative effects (**Figs.S13-S14**). Comparison of effective land surface albedo with satellite estimates suggests too low albedo in the Central Valley for visible shortwave radiation (**Fig.S19**). One possible reason for the model's dry and warm biases over the agriculture-dominated lands (**Fig.S2**) is neglect of agricultural irrigation. Irrigation-induced increases in evapotranspiration have been shown to enhance precipitation and result in net land surface cooling according to several modeling studies [DeAngelis et al., 2010; Thiery et al., 2017; Yao et al., 2022; Zeng et al., 2022]. A recent study by Chen and Dirmeyer [2019] showed that the irrigation-induced reduction of summer T_{max} in the Central Valley ranges from 0.5–2.5 ºC, with higher resolution models estimating larger reductions.

4. Results: Simulation of Atmospheric Composition

4.1 Global distributions of aerosols

[Figure 13 about here]

We compare global distributions of aerosols and their composition simulated by AM4.1, AM4VR, and the C96 experiment with emissions and chemical model formulation updated as in AM4VR (Table S1). Unless otherwise noted, AM4VR results in Sections 4 and 5 are presented from the simulation with ε_1 = 0.6 km^{-1}**. Figure 13** compares simulated regional monthly mean Aerosol Optical Depth (AOD) for 2000-2014 with observations from the MODIS [Sayer et al., 2014] and MISR [Kahn et al., 2009] instruments. AM4VR reduces the AM4.1 high AOD biases over East Asia, owing to the improved representation of aerosol precursor emissions in China (**Fig.4**). The AM4.1 high bias over Europe is also reduced in AM4VR, primarily due to reduced SOA from biogenic isoprene and monoterpenes emissions. AM4VR simulates lower AOD compared to C96 in the Amazon basin and Central Africa, likely due to stronger wet removal resulting from increased precipitation in these regions (**Fig.5**).

[Figure 14 about here]

The wind-driven aerosols such as dust and sea salt are sensitive to model-simulated maximum surface wind speed, which may change as the model horizontal resolution varies. Changes in precipitation and clouds can also modulate wet scavenging of aerosols and influence surface bareness for dust

emissions. **Fig.S20** compares simulated surface concentrations of dust and sea salt sodium from C96 and AM4VR with observations at 28 locations worldwide. AM4VR does not show systematic biases in sea salt and agrees better with observed values (R=0.9) than C96 (R=0.67). For dust, the correlation coefficient R increases from 0.79 in C96 to 0.85 in AM4VR. The two models bracket the observed surface dust concentrations at sites downwind of Australia – the biggest dust source in the Southern Hemisphere. Due to a reduction of precipitation dry bias over Australia (**Fig.5**), AM4VR exhibits substantially lower surface bareness and therefore lower dust emissions from western Australia compared to C96 (**Fig.S21**), consistent with satellite observations the dust sources are mainly located in eastern Australia [Ginoux et al., 2012]. Comparison of dust vertical profiles with the Atmospheric Tomography (ATom) aircraft campaign data [Froyd et al., 2019; 2021] shows that the two models perform similarly in the remote atmosphere over northern midlatitudes and tropics (**Fig.14**). Over southern mid-latitudes, however, lower dust levels simulated in AM4VR agree better with ATom observations (median bias = 0.001 μg/m^3 in AM4VR compared to 0.008 μg/m^3 in C96). Both models show positive biases in the free troposphere, suggesting the need for further work on scale-aware parameterizations for wet scavenging of aerosols in clouds.

4.2 Aerosols over the Continental US

[Fig.15 and Fig.16 about here]

We perform more detailed evaluation of aerosols over CONUS, including regional source characteristics, seasonality, and aerosol composition. **Fig.15** shows a comparison of long-term annual mean AOD (550 nm) with AERONET observations in North America. **Fig.16** displays comparison of monthly AOD climatology with MODIS and MISR satellite retrievals averaged over sub-regions of North America. Observations at AERONET sites are more accurate in magnitude while satellite retrievals provide vast spatiotemporal coverage. Evaluation with AERONET data shows a reduction of positive AOD bias from 25-100% in AM4.1 to within 25% in AM4VR for most southwestern and eastern US sites. The differences in model AOD over the Southwest stem from the differences in simulated dust abundances (comparing brown bars in **Fig.16** versus **Fig.S22**). Over the Great Plains, the Midwest and Southeastern US regions, lower AOD simulated in AM4VR reflects decreased SOA from biogenic isoprene and monoterpenes emissions for the summer months and decreased nitrate aerosol for the non-summer months. The AOD values in AM4VR are within the bounds of uncertainties in the three satellite AOD products [e.g., Kahn et al., 2010; Levy et al., 2018]. The MISR AOD is biased high over the Pacific Ocean when the AOD is very low [Kahn et al., 2010]. Over land in the eastern US during summer, AM4.1 is biased high against all satellite products while AM4VR falls within the bounds of MODIS and MISR retrievals. Some of the discrepancies may also reflect the fact that satellite retrievals are typically only successful for cloud-free pixels.

[Figures 17 and 18 about here]

We evaluate biogenic emissions simulated in AM4VR using tropospheric column densities of formaldehyde (HCHO), a high-yield isoprene oxidation product, retrieved from the TROPOspheric Monitoring Instrument (TROPOMI) (**Fig.17**). Following the approach of Kaiser et al. [2018] based on validation with independent aircraft measurements, we apply a 37% bias correction to monthly TROPOMI data provided by De Smedt et al. [2021] for 2018-2020 (**Text S5**). The TROPOMI comparison, along with the OMI comparison discussed earlier (**Fig.3**), indicates that the spatial distribution and magnitude of biogenic isoprene emissions simulated in AM4VR are in reasonable agreement with the top-down satellite constraints. Comparison with ground-based observations from

the IMPROVE (Interagency Monitoring of Protected Visual Environments) network exhibits significantly reduced biases in surface organic matter (OM) concentrations during summer in AM4VR, due to decreased biogenic SOA (**Fig.18**). AM4.1 overestimates summer OM concentrations by a factor of two across the central and eastern US. Summer OM concentrations over the Southeast decrease from 9.6 $\mu g/m^3$ in AM4.1 to 5.4 $\mu g/m^3$ in AM4VR, compared with 4.0 $\mu g/m^3$ in observations. Comparison of OM monthly climatology for the croplands-dominated Midwest shows a similar reduction of bias in AM4VR for summer (Fig.19a). The spatial distribution of biogenic SOA over the eastern US simulated in AM4VR agrees well with the spatial distribution of tropospheric HCHO columns observed from space (**Fig.17**).

While AM4VR with higher resolution clearly exhibits improvements upon AM4.1 in representing aerosols in urban areas (**Fig.18d** versus **Fig.18h**), all models capture only 50% of observed OM levels during the non-summer months (**Figs.18e** and **19a**). This underestimate is common in CMIP6 models [Turnock et al., 2020] and may reflect the combined effects of model deficiencies in representing SOA from oxidation of VOCs and too low primary OM emissions from anthropogenic and biomass burning sources. Our current chemistry scheme does not consider emissions and chemistry for aromatic hydrocarbons, which are important SOA precursors in urban environments [Wang et al., 2020; Nie et al., 2022]. We find that primary OM emissions from NEI2017 are two times greater than the estimate from the CEDS inventory used in AM4VR (purple star vs green line in **Fig.4b**). Mounting evidence indicates underestimates of biomass burning emissions of carbonaceous aerosols in GFED4s [e.g., Pan et al., 2020; Xie et al., 2020]. All three models using GFED4s underpredicted overall aerosol loading over the Pacific Northwest during July-September when wildfire peaks seasonally (**Figs.16 and 18**). In the Southeast and the Central US, crop-residue fires and prescribed burning are common in the non-summer months [Jaffe et al., 2020]. These prescribed low-intensity or understory burns are harder for satellites to detect but can emit considerable amounts of carbonaceous aerosols [e.g., Nowell et al., 2018]. Using multiple streams of high-resolution remote sensing data, Chen et al. [2023] recently created a new burned area dataset as a component of the GFED version 5 under development. GFED5 estimated burned area in the US is more than two times higher than GFED4s for the non-summer months [Chen et al., 2023].

[Figure 19 about here]

Comparison of ammonium nitrate aerosol (NH_4NO_3) in surface air over the croplands-dominated Midwest exhibits strongly reduced bias in AM4VR compared to AM4.1 (**Fig.19b**). The improvement reflects faster removal of HNO_3 and NH_3 by terrestrial ecosystems represented in AM4VR with an interactive dry deposition scheme coupled to vegetation in LM4.0 (Section 2). Note that dry and wet deposition of NH_4NO_3 aerosol in AM4VR are calculated as in AM4.1 [Horowitz et al., 2020]. During March-April-May, faster removal of HNO_3 and NH_3 by vegetation results in 50% lower NH_4NO_3 aerosol concentrations in AM4VR compared to AM4.1 using prescribed monthly climatology of dry deposition velocities. Evaluation with observations from the US Air Quality System (AQS) shows that AM4VR captures nitrate pollution hotspots in the agriculture-dense areas in the Central Valley, the Midwest, and Pennsylvania (**Fig.19c**). Lower NH_4NO_3 aerosol in AM4VR decreases simulated AOD compared to AM4.1 in late spring. A low-AOD bias is found in AM4VR over the US Pacific Northwest, Mexico, and Northeast Asia (**Figs.13 and 16**). For these regions in late spring, we suggest that the agreement of AM4.1 AOD with MODIS may reflect compensating errors of too high nitrate aerosols and too low organic aerosols from wildfires and prescribed burning. The CEDS inventories used in both models do not sufficiently represent varying seasonality of NH_3 emissions with regional agricultural management

practices [e.g., Paulot et al., 2014; Wang et al., 2020; Beaudor et al., 2023], which may also contribute to seasonal biases in simulated NH_4NO_3 aerosol.

[Figure 20 about here]
Comparison of sulfate aerosol in surface air at IMPROVE sites over the eastern US (**Fig.20**) demonstrates the ability of AM4VR to represent the observed marked reductions (two thirds) of sulfate aerosol in recent decades, which have been shown to strengthen Atlantic hurricane activity [e.g., Murakami, 2022]. AM4.1 underpredicted peak summertime sulfate concentration. Including a bug fix to an error in AM4.1 for calculating aerosol surface area for heterogeneous chemistry, the C96 model is unbiased, but AM4VR is biased high by ~20% in polluted conditions during the earlier period (1995-2009). In the US, especially in states along the Ohio River Valley, tall smokestacks (stacks of 150 - 300 meter) are used at coal power plants to release SO_2 and NO_x emissions high into the atmosphere to help limit the impact of these emissions on local air quality (https://www.gao.gov/assets/gao-11-473.pdf). The AM4VR high-sulfate bias along the Ohio River Valley may reflect the lack of accounting for stack heights and plume rise, as all power plant emissions are placed in the shallow model surface layer (30 m). Ahsan et al. [2023] showed that CMIP6 models are sensitive to the assumptions made about SO_2 injection height. Realistic representation of power plant plume rise may be more important in high-resolution models, in which chemical reactions occur before concentrated emissions are diluted.

[Figure 21 about here]
Finally, we evaluate total $PM_{2.5}$ concentrations in US surface air during summer, using observations from the IMPROVE network, located mostly in national parks and wilderness areas, and from the AQS, which includes IMPROVE sites and additional sites clustered in populated areas (**Fig.21**). For coarse resolution models that do not resolve urban areas, it makes more sense to compare with IMPROVE data. The Pearson correlation coefficient with IMPROVE observations at sites across the US increases from 0.7 for AM4.1 to 0.9 for the C96 model with AM4VR aerosol physics and emissions. Mean $PM_{2.5}$ levels at IMPROVE sites decreased from 10.4 $\mu g/m^3$ in AM4.1 to 7.5 $\mu g/m^3$, compared to 7.0 $\mu g/m^3$ from observations. Compared to the C96 model, AM4VR shows higher $PM_{2.5}$ at AQS sites along the Ohio River Valley, due in part to overestimated sulfate. AM4VR at 13 km resolution better captures the observed $PM_{2.5}$ pollution at AQS sites in the Los Angeles Basin, Southeast cities such as Birmingham, Alabama and Atlanta, Georgia, and the Northeast mega-cities such as Baltimore, Maryland and Philadelphia, Pennsylvania.

5. Results: US Climate - Air Quality Connections

5.1 Seamless Prediction of Local to Intercontinental Sources of Dust

[Figure 22 about here]
Comparison of surface fine dust concentrations at IMPROVE sites in Arizona demonstrates improved representation of Southwest US dustiness and seasonality in AM4VR (**Fig.22**). The correlation coefficient r^2 between observed and predicted monthly fine dust concentrations over Arizona increases from 0.23 in AM4.1 and 0.06 in C96 to 0.38 in AM4VR. Fine dust concentrations simulated in AM4.1 with the LM4.1 dynamic vegetation model are three times too high compared to observations (**Fig.22a**). AM4.1/LM4.1 used lower LAI and SAI thresholds and lower global emission factor than AM4VR/LM4.0 (**Table S2**), which therefore cannot explain increased dust emissions in AM4.1. One possible explanation for excessive dust abundances in AM4.1 is that LM4.1 estimated greater surface bareness and drier soils in the major dust source areas, such as the Mojave Desert, the Sonoran Desert and

Texas, compared to LM4.0 (**Fig.S23**). LM4.1 inclusion of daily dynamic fires may also increase dust emission by decreasing LAI and SAI. Improving dust emissions in AM4.1/LM4.1 is a subject of ongoing research at GFDL.

Comparing AM4VR and C96 with dust emissions calculated from LM4.0, we next focus our discussion on the extent to which the improved model representation of Southwest US springtime dryness, the North American monsoon, and associated mesoscale convective systems in AM4VR influence simulated dust. Comparison of soil moisture integrated over the top 15 cm of soil exhibits a difference of as large as $\pm$12 mm ($\pm$20%) between the two models in the Southwest, with AM4VR simulating drier soils during March and April but wetter soils during July and August (**Fig.22b**), consistent with the difference in simulated precipitation (**Fig.9b**). The LAI and SAI thresholds for erodible surface are the key controlling factors of dust emissions in semi-arid regions. In C96 with excessive precipitation and soil moisture during spring, simulated LAI and SAI are high enough to suppress dust emissions. Despite raising the LAI and SAI thresholds from 0.2 and 0.015 used in AM4VR to 0.35 and 0.05 for C96 (**Table S2**), the C96 model simulates too low springtime dustiness with little interannual variability. Improved representation of springtime dryness in AM4VR, along with greater maximum wind speeds with increased spatial resolution, raises Southwest US springtime dustiness in AM4VR, as evidenced by increases in both mean values and interannual variability.

During July and August when the North American monsoon peaks, strong winds flowing out of a collapsing thunderstorm can create severe dust storms called “haboobs”, most commonly in Arizona, where they have caused fatal highway accidents by reducing visibility but are extremely difficult to forecast [e.g., Kim et al., 2017]. Stronger winds associated with improved representation of mesoscale convective systems (i.e., thunderstorms) during the North American monsoon raise dust levels in AM4VR compared to C96, but simulated dust variations are too strong compared to observations. One possible explanation is that our current dust scheme does not account for the influence of soil moisture on wind erosion potential, which decreases with increasing soil moisture [Fécan et al., 1998]. Soil moisture at the surface can efficiently shut down dust emission for several hours after precipitation even in arid regions [Okin, 2022]. The improved representation of soil moisture seasonality in AM4VR provides a basis for future implementation of the influence of soil moisture on wind erosion threshold, which would hopefully further improve the simulation of Southwest US dust seasonality.

[Figure 23 about here]

In contrast to the semi-arid Southwest US where dust is primarily driven by local sources, dust abundances in the Southeast US are largely driven by trans-Atlantic transport of dust from the Sahara Desert in Africa [Prospero et al., 1996]. This typically happens during the months of June, July, and August, as observed and simulated by the AM4VR AMIP simulation (**Fig.23a-b**). The correlation coefficient r^2 between observed and predicted monthly fine dust concentrations in the Southeast increases from 0.44 in AM4.1 to 0.81 in C96 and 0.87 in AM4VR. In **Fig.23c**, we illustrate a massive African dust intrusion into the Gulf of Mexico and the Southeast US in June 2020, pushing observed surface $PM_{2.5}$ concentrations to a level (35 – 50 $\mu g/m^3$) exceeding the US National Ambient Air Quality Standard (35 $\mu g/m^3$ for 24-h average). This record-setting African dust intrusion episode, nicknamed Godzilla, was caused by convection-generated haboobs over the Sahara and an anomalously strong African easterly jet [Francis et al., 2020; Pu et al., 2021; Yu et al., 2021; https://svs.gsfc.nasa.gov/4849]. With horizontal winds nudged to GFS analyses (regridded to 1.4°x1.4°), AM4VR captures this African dust intrusion event, with simulated 24-h $PM_{2.5}$ concentrations approaching 35 $\mu g/m^3$ along the dust

plume track in the Southeast US on June 26-27, 2020. Unlike a regional model, AM4VR with a seamless variable-resolution grid structure accounts for such air quality degradation events in the US from upstream sources and intercontinental transport.

5.2 Ozone Air Quality and Land-biosphere Feedbacks

[Figure 24 about here]

In this section, we examine the extent to which the improved representation of emissions, physical climate, air pollution meteorology, and land-biosphere feedback affects simulation of ozone air quality. Comparison of long-term JJA mean daily maximum 8-hour average (MDA8) surface ozone concentrations in the northern hemisphere exhibits reduced bias in AM4VR (**Fig.24**). Note that surface ozone concentrations for both AM4.1 and AM4VR used in this study are output prior to adding the deposition, emissions, and chemistry tendencies, avoiding the numerical issues reducing surface ozone concentrations in the AM4.1 result reported in Horowitz et al. [2020] (**Text S6**). Observations are compiled from the US AQS (1990-present), China's Ministry of Ecology and Environment surface ozone monitoring network (2013-present; archived at https://quotsoft.net), and the Tropospheric Ozone Assessment Report (1990-2014, Schultz et al., 2017). The JJA mean biases in MDA8 ozone averaged across sites in the Northern Hemisphere were reduced by 6 ppb and RMSE decreased from 15 ppb in AM4.1 to 11 ppb in AM4VR. The improvement in boreal regions (above 45°N) reflects faster ozone removal by vegetation simulated in the dynamic dry deposition scheme in AM4VR, compared to the monthly dry deposition climatology used by AM4.1, as discussed in greater detail by Lin et al. [2019]. Over the high-NO_x regions such as the North China Plain, Northern India, and the Midwest US where ozone formation is VOC-limited, summer MDA8 ozone biases were reduced by 10-20 ppb in AM4VR, due to more realistic estimates of biogenic isoprene emissions (**Fig.2 and Fig.S6**).

[Figures 25 about here]

Over the CONUS region (**Fig.25**), the differences in simulated surface ozone reflect the combined effects of changes in dry deposition, BVOC emissions, anthropogenic emissions, and model resolution. We compare differences from AM4.1 for US summer mean MDA8 ozone in AM4VR and in the C96 experiment using AM4VR emissions, chemistry, and deposition schemes but at the same coarse resolution as in AM4.1. Compared to AM4.1, the C96 experiment shows reductions in surface ozone over the Pacific Northwest caused by faster ozone dry deposition velocities ($V_{d,O3}$) and over the high-NO_x eastern US regions caused by lower BVOC emissions (**Fig.2**), while increases in surface ozone are simulated for the Southwest and the central US (**Fig.25a**). AM4VR shows higher MDA8 ozone over California and in urban areas, but unlike the C96 model, AM4VR does not simulate broad-scale ozone increases in the central US compared to AM4.1 (**Fig.25b**). Comparison of summer daytime $V_{d,O3}$ simulated in C96 and AM4VR indicates that increases in surface ozone over the central US in C96 are caused by the precipitation dry bias leading to slower ozone removal by vegetation due to less vegetation and decreased stomatal conductance (**Fig.25c**). With improved simulation of precipitation, AM4VR captures the salient features of $V_{d,O3}$ derived from ozone flux measurements over forests, croplands, and pastures (**Fig.25d; see Fig.S24** for each land cover type and Table 1 of Lin et al. 2019 for measurement data). Improved representation of summer drought in the Pacific Northwest and Northern California in AM4VR leads to reductions in ozone removal by vegetation and therefore increases in surface ozone concentrations compared to C96. The broad-scale pattern of differences in surface MDA8 ozone concentrations between C96 and AM4VR (comparing **Fig.25a** and **Fig.25b**) generally follows the pattern of differences in simulated precipitation and $V_{d,O3}$. Another effect of higher

model resolution is a refinement of the slower ozone removal over the Great Lakes, due to low surface roughness, which combined with improved representation of lake breeze meteorology may enable simulation of the observed high-O_3 pollution events at coastal counties around Lake Michigan [Dye et al., 1995; Stanier et al., 2022].

Measurements of ambient ozone concentrations are typically collected at a few meters above the Earth's surface, where a lower ozone mixing ratio is expected due to the effects of vegetation canopies [e.g., Makar et al., 2017], while simulated ozone reflects concentrations in the 30-m model surface layer. To address this representativeness issue, we calculate ozone at the 2m level based on interpolation between the lowest model layer and the surface fluxes in AM4VR, considering surface roughness and atmospheric stability (**Text S7**). Summer mean MDA8 ozone computed at the 2m level is 3-10 ppb lower than that in the lowest model layer over forested areas in the eastern US (**Fig.S25**). The effects in the Central Valley and the sparsely-vegetated areas are small (< 2 ppb). Calculated MDA8 ozone at the 2m level in AM4VR exhibits reduced bias against the EPA AQS observations (**Fig.25e-f**).

[Figure 26 about here]
Zoomed into the US West Coast, **Fig.26a** demonstrates an improved representation of summer ozone pollution in AM4VR relative to AM4.1. AM4.1 overpredicts ozone in the Pacific Northwest and at coastal sites, and has difficulty simulating the observed ozone pollution hotspots in the Central Valley and Southern California. AM4VR exhibits reduced ozone bias in the Pacific Northwest, attributed primarily to the interactive dry deposition scheme. Over California, AM4VR at 13 km resolution shows the skill of resolving sharp gradients in urban-to-rural ozone formation regimes, such as capturing the observed low ozone within the Los Angeles Basin, where ozone formation is NO_x-saturated, and the sharp ozone increases in the downwind regions, where ozone formation is more NO_x-limited. The Pearson pattern correlation coefficient with observations increases from 0.6 for AM4.1 to 0.8 for AM4VR. Both models overpredict ozone in Northern California, which may reflect insufficient treatment of wildfire plume height and chemistry [Paugam et al., 2016; Li et al., 2023], overestimates of NO_x emissions, underestimates of aerosols from wildfires that influence heterogeneous chemistry [Pan et al., 2020; Xie et al., 2020; Jaffe et al., 2020], and the model's dry and warm biases affecting simulated BVOC emissions and ozone removal by vegetation. Comparison of the probability distribution of JJA daily MDA8 ozone (**Fig. 26**b) highlights the skill of AM4VR in simulating high-ozone pollution extremes in the San Joaquin Valley and Southern California. The percentage of site-days with MDA8 ozone above the US National Ambient Air Quality Standard (70 ppb) increases from 13% in AM4.1 to 32% in AM4VR, compared to 31% in observations. The 90th percentile of MDA8 ozone increases from 72 ppb in AM4.1 to 84 ppb in AM4VR, compared to 87 ppb in observations. The standard deviation (σ) of daily MDA8 ozone nearly doubled in AM4VR from AM4.1.

[Figure 27 about here]
Comparison of 24-h average surface NO_2 and ozone concentrations **(Fig.27)** further illustrates that AM4VR at 13 km resolution captures the spatiotemporal variations in sources, formation regimes, chemical and depositional sinks of ozone pollution across California. During winter, strong temperature inversions trap NO_x emissions from industries, road traffic, and agriculture at ground level in the San Francisco Bay Area, the Central Valley, and the Los Angeles Basin, as observed and simulated in AM4VR. The abundance of NO_x in surface air and the lack of radiation result in very low ozone levels in these air basins during winter, while the surrounding mountain ranges experience higher ozone concentrations due in part to stratospheric influence [Lin et al., 2012ab]. During summer, plentiful

radiation enhances HO_x supply and BVOC emissions. The ozone production regime in the Central Valley transitions from VOC-limited in winter to NO_x-limited in summer. The observed summer mean ozone levels across California show a sharp urban-to-rural gradient: below 30 ppb in the urban centers of the San Francisco Bay Area and the Los Angeles Basin, 30-50 ppb in urban and suburban areas, while above 60 ppb in suburban and rural areas downwind of the Sacramento Valley, the San Joaquin Valley, and the Los Angeles Basin. At 100 km resolution in AM4.1, the diverse air basins of California are not resolved, resulting in overestimates of ozone in winter while underpredicting peak ozone concentrations in suburban and rural areas during summer. AM4VR's marked improvements in representing ozone air pollution over California reflect several key factors: (1) improved representation of NO_x-rich urban environments through the high-resolution grid and anthropogenic emissions inventory; (2) sharp urban-to-rural increases in BVOC emissions through MEGAN driven by high-resolution satellite land cover datasets (**Fig.2**); (3) improved representation of air pollution meteorology conducive to pollution accumulation in mountain valleys; and (4) improved representation of summer drought in the Central Valley leading to reduced ozone removal by vegetation (**Figs.11 and 25**).

5.3 Winter Haze and Fog Formation in Mountain Valleys

[Figures 28 and 29 about here]

Following the enactment of the US Clean Air Act, pollution control regulations and cleaner technologies have steadily improved $PM_{2.5}$ air quality in the US. But some valleys in the western US, such as California's Central Valley and Utah's Salt Lake Valley, still experience wintertime $PM_{2.5}$ pollution exceeding national air quality standards [e.g., Franchin et al., 2018; Womack et al., 2019]. Strong temperature inversions in these mountain valleys during wintertime trap pollution at ground level to form NH_4NO_3 aerosol. AM4VR captures the observed key characteristics of NH_4NO_3-dominated haze pollution in the Central Valley during winter, more severe in the San Joaquin Valley in the south (**Fig.28**). In contrast, the observed $PM_{2.5}$ and NH_4NO_3 pollution hotspot in the Central Valley is absent in the C96 experiment, in which the $PM_{2.5}$ peak is much weaker and confined to the Bay Area. Comparing observations at Fresno and Visalia in the San Joaquin Valley for the 2001-2010 versus 2011-2020 periods, we find ~20% reductions in wintertime NH_4NO_3 aerosol during the last decade (**Fig.29**). AM4VR captures the magnitude, year-to-year variability, and decadal trends of NH_4NO_3 aerosol in the San Joaquin Valley, but simulates only 66% of total $PM_{2.5}$ levels, due to underestimates of organic aerosols as discussed in Section 4. The absence of regulation on NH_3 emissions from agricultural practices in the US has led to an increase of NH_3 emissions [Warner et al., 2017]. The decreasing trend of NH_4NO_3 aerosol in the San Joaquin Valley is driven by reductions of NO_x and VOC emissions (**Fig.4**), which undergo complex chemical oxidation reactions, forming HNO_3 that reacts with gas-phase NH_3 to form NH_4NO_3 aerosol [e.g., Womack et al., 2019].

[**Figure 30 about here**]

Ammonium nitrate is extremely hygroscopic, making it an ideal cloud condensation nuclei (CCN) for fog formation at low supersaturation [e.g., Mazoyer et al., 2019]. California's Central Valley is known for dense wintertime ground fog, called Tule fog, which can significantly reduce visibility, resulting in deadly multi-vehicle accidents on roadways, while helping provide nut and fruit trees with the "winter chill" required to improve productivity [e.g., Baldocchi et al., 2014]. Central Valley fog frequency exhibits a pronounced north-south gradient, with fog occurring more frequently in southern latitudes than northern [Gray et al., 2019]. This pattern is consistent with more NH_4NO_3 aerosol available in the San Joaquin Valley as a CCN for fog formation. The formation of fog droplets requires aerosol, humidity, and cooling

[Lakra and Avishek, 2022]. Observations and AM4VR simulations show that the Sacramento Valley in the north consistently receives more rain than the San Joaquin Valley in the south, whereas the 2 m relative humidity is higher in the San Joaquin Valley (**Fig.30**). The fact that fog occurs more frequently in the warmer and drier San Joaquin Valley suggests that the saturation value needed for fog formation is likely brought down by increased aerosol number concentration [Mazoyer et al. 2019]. Ammonium nitrate aerosol is typically not represented in physical climate–focused models, such as GFDL AM4.0 [Zhao et al., 2018], as representing its formation requires inclusion of complex atmospheric chemistry and thermodynamics. Our analyses demonstrate the value of including comprehensive atmospheric chemistry in high-resolution climate models to understand haze and fog frequency in agriculture air basins, offering research opportunities for predicting such events under climate change, which has implications not only for the health of outdoor farmworkers but also for agricultural productivity.

6. Conclusions and Future Directions

The GFDL AM4VR variable-resolution global chemistry-climate model, with horizontal resolution of 13 km over the US, shows marked improvements, over the previous 100-km uniform resolution AM4.1, in US mean climate, storminess, and air quality extremes while maintaining a comparable or improved simulation of global-scale circulation and climate. Compared to the 25-km uniform resolution model, AM4VR shows ~50% reduction of computational burden and doubled resolution in the US enables improved simulation of the mesoscale convective systems driving the central US warm-season precipitation. With a seamless variable-resolution grid structure, AM4VR allows for US-focused research in regions with complex geographical features (e.g. intermountain valleys), accounting for the impacts from global climate change and Earth system feedbacks, while avoiding inconsistencies associated with imposing boundary conditions in a regional model. While several studies have previously evaluated variable-resolution atmospheric chemistry simulations with prescribed meteorology [e.g. Bindle et al., 2021; Schwantes et al., 2022], here we highlight the value of regional grid refinements in representing US climate–air quality interactions through interactive meteorology-chemistry coupling and land-biosphere feedbacks.

Specifically, we use a suite of 33-year AMIP simulations to show that: (1) reducing the long-standing climate model bias of precipitation deficiency in the US Great Plains increases ozone removal by vegetation and reduces model bias in surface ozone concentrations; (2) improved representation of springtime drought, vegetation cover, and summertime mesoscale convective systems during the North American monsoon improves simulation of Southwest US dustiness; (3) representing reactive nitrogen deposition to croplands in a dynamic vegetation land model improves simulation of ammonium nitrate aerosol in agriculture air basins. Through the considerably improved representation of hydroclimate and increased biosphere-atmosphere interactions at high spatial resolution, AM4VR provides vastly superior fidelity over AM4.1 in simulating atmospheric chemical composition, including natural aerosols, surface $PM_{2.5}$ and ozone air quality over the US. In contrast to regional air quality models with prescribed land cover and vegetation characteristics, AM4VR offers novel opportunities to study changes in vegetation dynamics and feedback to atmospheric composition in future climate with rising temperatures and shifting rainfall patterns. A future global and regional model intercomparison project focusing on atmosphere–biosphere–air quality interactions will benefit the community and will improve understanding how these interactions contribute to air quality extremes and trends.

AM4VR exhibits excellent representation of winter precipitation extremes, summer drought, air pollution meteorology, and urban-to-rural chemical regimes over California with complex terrain. These improvements modulate accumulation, sources and sinks of atmospheric pollutants through interactive natural emissions and pollution removal by vegetation, enabling skillful prediction of both extreme summertime ozone pollution and ammonium-dominated winter haze events in the Central Valley. These capabilities have important applications for public health and transportation safety. Representing severe winter haze in the San Joaquin Valley also has implications for prediction of Tule fog and its effects on agriculture, as ammonium nitrate aerosol may be critical CCN for fog dynamics [Gray et al., 2019]. While regional air quality models with prescribed meteorology may represent these features, the ability to represent fine-scale air quality–meteorology interactions in a global chemistry-climate model offers novel opportunities to understand and contextualize the influence of large-scale atmospheric circulation patterns and climate change. For instance, hydroclimate variability and extreme heat in California and other parts of US lands are linked to the El Niño - Southern Oscillation and the Pacific Decadal Oscillation. Future multi-ensemble AM4VR simulations would improve understanding of the response of US hydroclimate and air quality extremes to ocean variability with implications for seasonal air quality forecasting.

Moving forward, we prioritize future model development in scale-aware parameterizations of convection and clouds, wet scavenging of aerosols in clouds, lightning, and power plant plume rise. Efforts are also needed to improve simulations of organic aerosols from anthropogenic, biomass burning, and biogenic sources, including better emission inventories for primary organic carbon emissions and improved representation of oxidation of VOCs. Priority future developments to enhance land-atmosphere coupling and feedback include: incorporating a dynamic urban canopy model to represent urban heat island effects [Li et al., 2016a, 2016b; Liao et al., 2021], treatment of irrigation [Zeng et al., 2022], prognostic daily fires [Rabin et al., 2015; Ward et al., 2016; Ward et al., 2018] with dynamic plume rise and interaction with atmospheric chemistry, and coupling BVOC emissions to the dynamic vegetation land model. Incorporating these ongoing developments at GFDL into AM4VR, with improved representation of hydroclimate (e.g., western US drought) as demonstrated in the present study, would greatly enhance our ability to understand Earth system feedbacks in a changing climate and promote the development of improved air quality forecasting with applications to public safety, transportation, and agriculture.

Acknowledgments: We thank William Cooke for providing LM4.0 land initial conditions from GFDL SPEAR, Lin Pu for updating SST and sea ice data, Isabelle De Smedt for providing TROPOMI HCHO data, and Maria Val Martin for providing MISR wildfire smoke injection height data. We are grateful for helpful conversations on emission uncertainties with Brian McDonald and Colin Harkins at NOAA Chemical Science Laboratory. We thank Songmiao Fan and Xiaosong Yang for helpful comments and suggestions.

Open Research.

Lin, M. (2023). Supporting Data for the GFDL Variable-Resolution Global Chemistry-Climate Model for Research at the Nexus of US Climate and Air Quality Extremes [Dataset]. https://doi.org/10.34770/azw8-7g66.

Lin, M. (2023). Source code of GFDL AM4VR [Software]. https://zenodo.org/records/10257866.

References:

Adler, R., Huffman, G., Chang, A., Ferraro, R., Xie, P., Janowiak, J., et al. (2003). The version 2 global precipitation climatology project (GPCP) monthly precipitation analysis (1979-present). Journal of Hydrometeorology, 4, 1147–1167. https://www.esrl.noaa.gov/psd/data/gridded/data.gpcp.html

American Lung Association (2023), State of the Air 2023, Available at https://www.lung.org/getmedia/338b0c3c-6bf8-480f-9e6e-b93868c6c476/SOTA-2023.pdf

Anber, U. M., Jeevanjee, N., Harris, L. M.,& Held, I. M. (2018). Sensitivity of radiative-convective equilibrium to divergence damping inGFDL-FV3-based cloud-resolving model simulations. Journal of Advances inModeling Earth Systems,10, 1527–1536. https://doi.org/10.1029/2017MS001225

Arizpe AH, Falk DA, Woodhouse CA, Swetnam TW (2020). Widespread fire years in the US–Mexico Sky Islands are contingent on both winter and monsoon precipitation. International Journal of Wildland Fire 29, 1072–1087.

Ahsan, H., Wang, H., Wu, J., Wu, M., Smith, S. J., Bauer, S., Suchyta, H., Olivié, D., Myhre, G., Matsui, H., Bian, H., Lamarque, J.-F., Carslaw, K., Horowitz, L., Regayre, L., Chin, M., Schulz, M., Skeie, R. B., Takemura, T., and Naik, V.: The Emissions Model Intercomparison Project (Emissions-MIP): quantifying model sensitivity to emission characteristics, EGUsphere [preprint], https://doi.org/10.5194/egusphere-2023-604, 2023.

Baldocchi, D., and E. Waller (2014),Winter fog is decreasing in the fruit growing region of the Central Valley of California,Geophys. Res. Lett.,41,3251–3256, doi:10.1002/2014GL06001

Beaudor, M., Vuichard, N., Lathière, J., Evangeliou, N., Van Damme, M., Clarisse, L., and Hauglustaine, D.: Global agricultural ammonia emissions simulated with the ORCHIDEE land surface model, Geosci. Model Dev., 16, 1053–1081, https://doi.org/10.5194/gmd-16-1053-2023, 2023

Bindle, L., Martin, R. V., Cooper, M. J., Lundgren, E. W., Eastham, S. D., Auer, B. M., et al. (2021). Grid-stretching capability for the GEOS-Chem 13.0.0 atmospheric chemistry model. Geoscientific Model Development, 14(10), 5977–5997. https://doi.org/10.5194/gmd-14-5977-2021

Calahorrano, Juncosa, J. F., Lindaas, J., O'Dell, K., Palm, B. B., Peng, Q., Flocke, F., et al. (2021). Daytime oxidized reactive nitrogen partitioning in western U.S. wildfire smoke plumes. Journal of Geophysical Research: Atmospheres, 126, e2020JD033484. https://doi.org/10.1029/2020JD033484

Chen, D., Aiguo Dai, Alex Hall (2021): The Convective-To-Total Precipitation Ratio and the “Drizzling” Bias in Climate Models. https://doi.org/10.1029/2020JD034198

Chen, L., & Dirmeyer, P. A. (2019). Global observed and modeled impacts of irrigation on surface temperature. International Journal of Climatology, 39(5), 2587– 2600. https://doi.org/10.1002/joc.5973

Chen, Y., Hall, J., van Wees, D., Andela, N., Hantson, S., Giglio, L., van der Werf, G. R., Morton, D. C., and Randerson, J. T.: Multi-decadal trends and variability in burned area from the 5th version of the Global Fire Emissions Database (GFED5), Earth Syst. Sci. Data Discuss. [preprint], https://doi.org/10.5194/essd-2023-182, in review, 2023.

Clifton, O., Paulot, F., Fiore, A., Horowitz, L., Correa, G., Baublitz, C., et al. (2020). Influence of dynamic ozone dry deposition on ozone pollution. Journal of Geophysical Research: Atmospheres, 125(8), e2020JD032398. https://doi.org/10.1029/2020JD032398

Dai, A. (2006). Precipitation characteristics in 18 coupled climate models. Journal of Climate, 9, 4605-4630.

Daly, C., Doggett, M.K., Smith, J.I., Olson, K.V., Halbleib, M.D., Dimcovic, Z., Keon, D., Loiselle, R.A., Steinberg, B., Ryan, A.D., Pancake, C.M., and E.M. Kaspar. 2021 Challenges in observation-based mapping of daily precipitation across the conterminous United States. Journal of Atmospheric and Oceanic Technology, 38, 1979-1992. https://doi.org/10.1175/JTECH-D-21-0054.1

DeAngelis, A., F. Dominguez, Y. Fan, A. Robock, M. D. Kustu, and D. Robinson (2010), Evidence of enhanced precipitation due to irrigation over the Great Plains of the United States,J. Geophys. Res.,115, D15115,doi:10.1029/2010JD013892.

Delworth, T. L., Cooke, W. F., Adcroft, A., Bushuk, M., Chen, J.-H., Dunne, K.A., Ginoux, P., Gudgel, R., Hallberg, R. W., Harris, L., Harrison, M. J., Johnson, N., Kapnick, S. B., Lin, S.-J., Lu, F., Malyshev, S., Milly, P. C., Murakami, H., Naik, V., Pascale, S., Paynter, D., Rosati, A., Schwarzkopf, M.D., Shevliakova, E., Underwood, S., Wittenberg, A. T., Xiang, B., Yang, X., Zeng, F., Zhang, H., Zhang, L., & Zhao, M. (2020). SPEAR: The Next Generation GFDL Modeling System for Seasonal to Multidecadal Prediction and Projection. Journal of Advances in Modeling Earth Systems, 12, e2019MS001895. https://doi.org/10.1029/2019MS001895

Dentener, F., Kinne, S., Bond, T., Boucher, O., Cofala, J., Generoso, S., Ginoux, P., Gong, S., Hoelzemann, J. J., Ito, A., Marelli, L., Penner, J. E., Putaud, J.-P., Textor, C., Schulz, M., van derWerf, G. R., & Wilson, J. (2006). Emissions of primary aerosol and precursor gases in the years 2000 and 1750 prescribed data-sets for AeroCom. Atmospheric Chemistry and Physics, 6(12), 4321– 4344. https://doi.org/10.5194/acp-6-4321-2006

De Smedt, I., Pinardi, G., Vigouroux, C., Compernolle, S., Bais, A., Benavent, N., Boersma, F., Chan, K.-L., Donner, S., Eichmann, K.-U., Hedelt, P., Hendrick, F., Irie, H., Kumar, V., Lambert, J.-C., Langerock, B., Lerot, C., Liu, C., Loyola, D., Piters, A., Richter, A., Rivera Cárdenas, C., Romahn, F., Ryan, R. G., Sinha, V., Theys, N., Vlietinck, J., Wagner, T., Wang, T., Yu, H., and Van Roozendael, M.: Comparative assessment of TROPOMI and OMI formaldehyde observations and validation against MAX-DOAS network column measurements, Atmos. Chem. Phys., 21, 12561–12593, https://doi.org/10.5194/acp-21-12561-2021, 2021.

Dong, W., J. P. Krasting, and H. Guo. Analysis of Precipitation Diurnal Cycle and Variance in Multiple Observations, CMIP6 Models, and a Series of GFDL-AM4.0 Simulations. Journal of Climate, 8637–8655, https://doi.org/10.1175/JCLI-D-23-0268.1.

Dunne, J. P., Horowitz, L. W., Adcroft, A. J., Ginoux, P., Held, I. M., et al. (2020). The GFDL earth system model version 4.1 (GFDL-ESM4.1): Overall coupled model description and simulation characteristics. Journal of Advances in Modeling Earth Systems, 12. https://doi.org/10.1029/2019MS002015

Dye, T.S., Roberts, P.T., Korc, M.E., 1995. Observations of transport processes for ozone and ozone precursors during the 1991 Lake Michigan Ozone Study. J. Appl. Meteorol. 34 (8), 1877–1889.

Emmons, L. K., Walters, S., Hess, P. G., Lamarque, J.-F., Pfister, G. G., Fillmore, D., Granier, C., Guenther, A., Kinnison, D., Laepple, T., Orlando, J., Tie, X., Tyndall, G., Wiedinmyer, C., Baughcum, S. L., & Kloster, S. (2010). Description and evaluation of the Model for Ozone and Related chemical Tracers, version 4 (MOZART-4). Geoscientific Model Development, 3(1), 43– 67. https://doi.org/10.5194/gmd-3-43-2010

Evans, Stuart, Paul Ginoux, Sergey Malyshev, and Elena Shevliakova (2016): Climate-vegetation interaction and amplification of Australian dust variability. Geophysical Research Letters, 43(22), DOI:10.1002/2016GL071016.

Fécan, F., Marticorena, B. and Bergametti, G., 1998. Parametrization of the increase of the aeolian erosion threshold wind friction velocity due to soil moisture for arid and semi-arid areas. In *Annales Geophysicae* (Vol. 17, No. 1, pp. 149-157). Berlin/Heidelberg: Springer-Verlag.

Fiore, A. M., Naik, V., and Leibensperger, E. M.: Air Quality and Climate Connections, J. Air Waste Manage., 65, 645–685, doi:10.1080/10962247.2015.1040526, 2015

Fountoukis, C. and Nenes, A.: ISORROPIA II: a computationally efficient thermodynamic equilibrium model for K^+–Ca^{2+}–Mg^{2+}–NH^{4+}–Na^+–SO_4^{2-}–NO^{3-}–Cl^-–H_2O aerosols, Atmos. Chem. Phys., 7, 4639–4659, https://doi.org/10.5194/acp-7-4639-2007, 2007.

Francis, D., Fonseca, R., Nelli, N., Cuesta, J., Weston, M., Evan, A., and Temimi, M.: The atmospheric drivers of the major Saharan dust storm in June 2020, Geophys. Res. Lett., 47, e2020GL090102, https://doi.org/10.1029/2020GL090102, 2020.

Franchin, A., D.L. Fibiger, L. Goldberger, E.E. McDuffie, A. Moravek, C.C. Womack, E.T. Crosman, K.S. Docherty, W.P. Dube, S.W. Hoch, B.H. Lee, R. Long, J.G. Murphy, J.A. Thornton, S.S. Brown, M. Baasandorj, and A.M. Middlebrook, Airborne and ground-based observations of ammonium-nitrate-dominated aerosols in a shallow boundary layer during intense winter pollution episodes in northern Utah. Atmos. Chem. Phys., 2018. 18(23): p. 17259-17276. https://www.atmos-chem-phys.net/18/17259/2018/

Freitas, S. R., Putman, W. M., Arnold, N. P., Adams, D. K., & Grell, G. A. (2020). Cascading toward a kilometer-scale GCM: Impacts of a scale-aware convection parameterization in the Goddard Earth observing system GCM. Geophysical Research Letters, 47(17). e2020GL087682. https://doi.org/10.1029/2020GL087682

Froyd, K.D., D.M. Murphy, C.A. Brock, P. Campuzano-Jost, J.E. Dibb, J.-L. Jimenez, A. Kupc, A.M. Middlebrook, G.P. Schill, K.L Thornhill, C.J. Williamson, J.C. Wilson, and L.D. Ziemba. 2019. A new method to quantify mineral dust and other aerosol species from aircraft platforms using single-particle mass spectrometry. Atmospheric Measurement Techniques 12:6209-6239. https://doi.org/10.5194/amt-12-6209-2019

Froyd, K.D., D.M. Murphy, G.P. Schill, and C.A. Brock. 2021. Atmospheric Tomography (ATom): Measurements from Particle Analysis By Laser Mass Spectrometry (PALMS). ORNL DAAC, Oak Ridge, Tennessee, USA. https://doi.org/10.3334/ORNLDAAC/1733

Gao, Y., Fu, J. S., Drake, J. B., Lamarque, J.-F., & Liu, Y. (2013). The impact of emission and climate change on ozone in the United States under representative concentration pathways (RCPs). Atmospheric Chemistry and Physics, 13(18), 9607–9621. https://doi.org/10.5194/
Acp-13-9607-2013

Galmarini, S., Makar, P., Clifton, O. E., Hogrefe, C., Bash, J. O., Bellasio, R., Bianconi, R., Bieser, J., Butler, T., Ducker, J., Flemming, J., Hodzic, A., Holmes, C. D., Kioutsioukis, I., Kranenburg, R., Lupascu, A., Perez-Camanyo, J. L., Pleim, J., Ryu, Y.-H., San Jose, R., Schwede, D., Silva, S., and Wolke, R.: Technical note: AQMEII4 Activity 1: evaluation of wet and dry deposition schemes as an integral part of regional-scale air quality models, Atmos. Chem. Phys., 21, 15663–15697, https://doi.org/10.5194/acp-21-15663-2021, 2021.

Ginoux, P., Chin, M., Tegen, I., Prospero, J.M., Holben, B., Dubovik, O. and Lin, S.J., 2001. Sources and distributions of dust aerosols simulated with the GOCART model. *Journal of Geophysical Research: Atmospheres*, *106* (D17), pp.20255-20273.

Ginoux, P., Prospero, J.M., Gill, T.E., Hsu, N.C. and Zhao, M. (2012). Global-scale attribution of anthropogenic and natural dust sources and their emission rates based on MODIS Deep Blue aerosol products. Reviews of Geophysics 50, 1–35

Golaz, J.-C., Horowitz, L. W., & Levy, H., II (2013). Cloud tuning in a coupled climate model: Impact on 20th century warming. Geophysical Research Letters, 40, 2246–2251. https://doi.org/10.1002/grl.50232

Goss, M., Swain, D. L., Abatzoglou, J. T., Sarhadi, A., Kolden, C. A., Williams, A. P., & Diffenbaugh, N. S. (2020). Climate change is increasing the likelihood of extreme autumn wildfire conditions across California. Environmental Research Letters, 15(9), 094016. https://doi.org/10.1088/1748-9326/ab83a7

Gray, E., Gilardoni, S., Baldocchi, D.,McDonald, B. C., Facchini, M. C., & Goldstein, A. H. (2019). Impact of air pollution controls on radiation fog frequency in the Central Valley of California.Journal of GeophysicalResearch: Atmospheres,124, 5889–5905.https://doi.org/10.1029/2018JD029419

Guenther, A. B, Karl, T., Harley, P., Wiedinmyer, C., Palmer, P. I., & Geron, C. (2006). Estimates of global terrestrial isoprene emissions using MEGAN (model of emissions of gases and aerosols from nature). Atmospheric Chemistry and Physics, 6(11), 3181– 3210. https://doi.org/10.5194/acp-6-3181-2006

Guenther, A. B., Jiang, X., Heald, C. L., Sakulyanontvittaya, T., Duhl, T., Emmons, L. K., & Wang, X. (2012). The model of emissions of gases and aerosols from nature version 2.1 (MEGAN 2.1): An extended and updated framework for modeling biogenic emissions. Geoscientific Model Development, 5(6), 1471– 1492. https://doi.org/10.5194/gmd-5-1471-2012

Haarsma, R, M Acosta, R Bakhshi, P-A Bretonnière, L-P Caron, M Castrillo, S Corti, P Davini, E Exarchou, F Fabiano, U Fladrich, R Fuentes, J García-Serrano, J von Hardenberg, T Koenigk, X Levine, V Meccia, T van Noije, G van den Oord, F Palmeiro, M Rodrigo, Y Ruprich-Robert, P Le Sager, E Tourigny, S Wang, M van Weele and K Wyser, 2020: HighResMIP versions of EC-Earth: EC-Earth3P and EC-Earth3P-HR. Description, model performance, data handling and validation. Geosci. Model Dev. https://doi.org/10.5194/gmd-2019-350

Harris L. M., Lin S-J, Tu CY (2016) High-resolution climate simulations using GFDL HiRAM with a stretched global grid. J Clim 29:4293–4314. https://doi.org/10.1175/JCLI-D-15-0389.1

Harris, L. M., Rees, S. L., Morin, M., Zhou, L., & Stern, W. F. (2019). Explicit prediction of continental convection in a skillful variable-resolution global model. Journal of Advances in Modeling Earth Systems, 11, 1847–1869. https://doi. org/10.1029/2018MS001542

Harris, L. M.; Chen, Xi; Putman, William; Zhou, Linjiong; Chen, Jan-Huey; A Scientific Description of the GFDL Finite-Volume Cubed-Sphere Dynamical Core. NOAA technical memorandum OAR GFDL ; 2021-001. DOI : https://doi.org/10.25923/6nhs-5897

Hoesly, R. M., Smith, S. J., Feng, L., Klimont, Z., Janssens-Maenhout, G., Pitkanen, T., Seibert, J. J., Vu, L., Andres, R. J., Bolt, R. M., Bond, T. C., Dawidowski, L., Kholod, N., Kurokawa, J.-i., Li, M., Liu, L., Lu, Z., Moura, M. C. P., O'Rourke, P. R., & Zhang, Q. (2018). Historical (1750–2014) anthropogenic emissions of reactive gases and aerosols from the Community Emissions Data System (CEDS). Geoscientific Model Development (Online), 11. https://doi.org/10.5194/gmd-11-369-2018

Hogrefe, C, P Liu, G Pouliot, R. Mathur, S Roselle, Johannes Flemming, and Meiyun Lin, et al., March 2018: Impacts of different characterizations of large-scale background on simulated regional-scale ozone over the continental United States. Atmospheric Chemistry and Physics, 18(5), DOI:10.5194/acp-18-3839-2018.

Holmes, C. D., Bertram, T. H., Confer, K. L., Graham, K. A., Ronan, A. C., Wirks, C. K., & Shah, V. (2019). The role of clouds in the tropospheric NOx cycle: A new modeling approach for cloud chemistry and its global implications. *Geophysical Research Letters*, 46(9), 4980–4990. https://doi.org/10.1029/2019GL081990

Horowitz, L.W. et al. (2020): The GFDL Global Atmospheric Chemistry-Climate Model AM4.1: Model Description and Simulation Characteristics. Journal of Advances in Modeling Earth Systems, 12(10), DOI:10.1029/2019MS002032.

Huffman, G.J., E.F. Stocker, D.T. Bolvin, E.J. Nelkin, Jackson Tan (2019), GPM IMERG Final Precipitation L3 Half Hourly 0.1 degree x 0.1 degree V06, Greenbelt, MD, Goddard Earth Sciences Data and Information Services Center (GES DISC), Accessed: [08/04/2021], 10.5067/GPM/IMERG/3B-HH/06

Huang, X., Rhoades, A. M., Ullrich, P. A., & Zarzycki, C. M. (2016). An evaluation of the variable-resolution CESM for modeling California's climate. Journal of Advances in Modeling Earth Systems, 8, 345– 369. https://doi.org/10.1002/2015MS000559

Hurtt, G. C., Chini, L., Sahajpal, R., Frolking, S., Bodirsky, B. L., Calvin, K., Doelman, J. C., Fisk, J., Fujimori, S., Klein Goldewijk, K., Hasegawa, T., Havlik, P., Heinimann, A., Humpenöder, F., Jungclaus, J., Kaplan, J. O., Kennedy, J., Krisztin, T., Lawrence, D., Lawrence, P., Ma, L., Mertz, O., Pongratz, J., Popp, A., Poulter, B., Riahi, K., Shevliakova, E., Stehfest, E., Thornton, P., Tubiello, F. N., van Vuuren, D. P., and Zhang, X.: Harmonization of global land use change and management for the period 850–2100 (LUH2) for CMIP6, Geosci. Model Dev., 13, 5425–5464, https://doi.org/10.5194/gmd-13-5425-2020, 2020.

Jaffe, D. A., Cooper, O. R., Fiore, A. M., Henderson, B. H., Tonneson, G. S., Russell, A. G., Henze, D. K., Langford, A. O., Lin, M., and Moore, T.: Scientific assessment of background ozone over the U.S.: Implications for air quality management, Elem. Sci. Anth., 6, 56, https://doi.org/10.1525/elementa.309, 2018.

Jaffe, D. A., Susan M. O'Neill, Narasimhan K. Larkin, Amara L. Holder, David L. Peterson, Jessica E. Halofsky & Ana G. Rappold (2020) Wildfire and prescribed burning impacts on air quality in the United States, Journal of the Air & Waste Management Association, 70:6, 583-615, DOI: 10.1080/10962247.2020.1749731

Jong, Bor-Ting, Thomas L Delworth, William F Cooke, Kai-Chih Tseng, and Hiroyuki Murakami, March 2023: Increases in extreme precipitation over the Northeast United States using high-resolution climate model simulations. npj Climate and Atmospheric Science, 18, DOI:10.1038/s41612-023-00347-w.

Kahn, R. A., Gaitley, B. J., Garay, M. J., Diner, D. J., Eck, T. F., Smirnov, A., and Holben, B. N. (2010), Multiangle Imaging SpectroRadiometer global aerosol product assessment by comparison with the Aerosol Robotic Network, J. Geophys. Res., 115, D23209, doi:10.1029/2010JD014601

Kaiser, J., Jacob, D. J., Zhu, L., Travis, K. R., Fisher, J. A., González Abad, G., Zhang, L., Zhang, X., Fried, A., Crounse, J. D., St. Clair, J. M., and Wisthaler, A.: High-resolution inversion of OMI formaldehyde columns to quantify isoprene emission on ecosystem-relevant scales: application to the southeast US, Atmos. Chem. Phys., 18, 5483–5497, https://doi.org/10.5194/acp-18-5483-2018, 2018.

Kanaya, Y., Yamaji, K., Miyakawa, T., Taketani, F., Zhu, C., Choi, Y., Komazaki, Y., Ikeda, K., Kondo, Y., and Klimont, Z.: Rapid reduction in black carbon emissions from China: evidence from 2009–2019 observations on Fukue Island, Japan, Atmos. Chem. Phys., 20, 6339–6356, https://doi.org/10.5194/acp-20-6339-2020, 2020

Kapnick, Sarah B., Xiaosong Yang, Gabriel A Vecchi, Thomas L Delworth, Richard G Gudgel, Sergey Malyshev, P C D Milly, Elena Shevliakova, Seth D Underwood, and S A Margulis, February 2018: Potential for western US seasonal snowpack prediction. Proceedings of the National Academy of Sciences, 115(6), DOI:10.1073/pnas.1716760115.

Kavassalis, S. C. & Murphy, J. G. Understanding ozone–meteorology correlations: a role for dry deposition. Geophys. Res. Lett. 44, 2922–2931 (2017).

Kim, D, Mian Chin, E M Kemp, Z Tao, C D Peters-Lidard, and Paul Ginoux, June 2017: Development of high-resolution dynamic dust source function - A case study with a strong dust storm in a regional model. Atmospheric Environment, 159, DOI:10.1016/j.atmosenv.2017.03.045.

Kok, J.F., Mahowald, N.M., Fratini, G., Gillies, J.A., Ishizuka, M., Leys, J.F., Mikami, M., Park, M.S., Park, S.U., Van Pelt, R.S. and Zobeck, T.M., 2014. An improved dust emission model–Part 1: Model description and comparison against measurements. *Atmospheric Chemistry and Physics*, *14*(23), pp.13023-13041.

Lakra K, Avishek K. A review on factors influencing fog formation, classification, forecasting, detection and impacts. Rend Lincei Sci Fis Nat. 2022;33(2):319-353. doi: 10.1007/s12210-022-01060-1. Epub 2022 Mar 14. PMID: 35309246; PMCID: PMC8918085.

Langford, A. O., Alvarez, R. J., Brioude, J., Fine, R., Gustin, M. S., Lin, M. Y., Marchbanks, R. D., Pierce, R. B., Sandberg, S. P., Senff, C. J., Weickmann, A. M., and Williams, E. J.: Entrainment of stratospheric air and Asian pollution by the convective boundary layer in the southwestern U.S, J. Geophys. Res., 122, 1312–1337, https://doi.org/10.1002/2016JD025987, 2017.

Lanzante, J. R., Dixon, K. W., Nath, M. J., Whitlock, C. E., & Adams-Smith, D. (2018). Some pitfalls in statistical downscaling of future climate. Bulletin of the American Meteorological Society, 99(4), 791– 803. https://doi.org/10.1175/BAMS-D-17-0046.1

Lau, Ngar-Cheung, and Mary Jo Nath, July 2012: A Model Study of Heat Waves over North America: Meteorological Aspects and Projections for the 21st Century. Journal of Climate, 25(14), DOI:10.1175/JCLI-D-11-00575.1.

Lee, M.-I., Schubert, S. D., Suarez, M. J., Held, I. M., Lau, N.-C., Ploshay, J. J., Kumar, A., Kim, H. K., & Schemm, J. K. E. (2007). An analysis of the warm-season diurnal cycle over the continental United States and Northern Mexico in general circulation models. Journal of Hydrometeorology, 8(3), 344– 366. https://doi.org/10.1175/JHM581.1

Levy, R. C., Mattoo, S., Sawyer, V., Shi, Y., Colarco, P. R., Lyapustin, A. I., Wang, Y., and Remer, L. A.: Exploring systematic offsets between aerosol products from the two MODIS sensors, Atmos. Meas. Tech., 11, 4073–4092, https://doi.org/10.5194/amt-11-4073-2018, 2018.

Li, Y., Tong, D., Ma, S., Freitas, S. R., Ahmadov, R., Sofiev, M., Zhang, X., Kondragunta, S., Kahn, R., Tang, Y., Baker, B., Campbell, P., Saylor, R., Grell, G., and Li, F.: Impacts of estimated plume rise on PM2.5 exceedance prediction during extreme wildfire events: a comparison of three schemes (Briggs, Freitas, and Sofiev), Atmos. Chem. Phys., 23, 3083–3101, https://doi.org/10.5194/acp-23-3083-2023, 2023.

Li, Dan, Sergey Malyshev, and Elena Shevliakova, June 2016: Exploring historical and future urban climate in the Earth System Modeling framework: 1. Model development and evaluation. Journal of Advances in Modeling Earth Systems, 8(2), DOI:10.1002/2015MS000578.

Li, Dan, Sergey Malyshev, and Elena Shevliakova, June 2016: Exploring historical and future urban climate in the Earth System Modeling framework: 2. Impact of urban land use over the Continental United States. Journal of Advances in Modeling Earth Systems, 8(2), DOI:10.1002/2015MS000579.

Liao, Weilin, Dan Li, Sergey Malyshev, Elena Shevliakova, Honghui Zhang, and Xiaoping Liu, March 2021: Amplified increases of compound hot extremes over urban land in China. Geophysical Research Letters, 48(6), DOI:10.1029/2020GL091252.

Lin, M., Holloway, T., Oki, T., Streets, D. G., and Richter, A.: Multi-scale model analysis of boundary layer ozone over East Asia, Atmos. Chem. Phys., 9, 3277–3301, https://doi.org/10.5194/acp-9-3277-2009, 2009.

Lin, M., T. Holloway, G. R. Carmichael and A. M. Fiore: Quantifying pollution inflow and outflow over East Asia in spring with regional and global models. Atmos. Chem. Phys., 10, 4221-4239, 2010.

Lin, M., Fiore, A. M., Cooper, O. R., Horowitz, L. W., Langford, A. O., Levy, H., Johnson, B. J., Naik, V., Oltmans, S. J., and Senff, C. J.: Springtime high surface ozone events over the western United States: Quantifying the role of stratospheric intrusions, J. Geophys. Res., 117, D00V22, doi:10.1029/2012jd018151, 2012a.

Lin, M., Fiore, A. M., Horowitz, L. W., Cooper, O. R., Naik, V., Holloway, J., Johnson, B. J., Middlebrook, A. M., Oltmans, S. J., Pollack, I. B., Ryerson, T. B., Warner, J. X., Wiedinmyer, C., Wilson, J., and Wyman, B.: Transport of Asian ozone pollution into surface air over the western United States in spring, J. Geophys. Res., 117, D00V07, doi:10.1029/2011jd016961, 2012b

Lin, M., Fiore, A. M., Horowitz, L. W., Langford, A. O., Oltmans, S. J., Tarasick, D., and Rieder, H. E.: Climate variability modulates western U.S. ozone air quality in spring via deep stratospheric intrusions, Nat. Commun., 6, 7105, doi:10.1038/ncomms8105, 2015a

Lin, M. et al. (2017), US surface ozone trends and extremes over 1980-2014: Quantifying the roles of rising Asian emissions, domestic controls, wildfires, and climate. Atmos. Chem. Phys., 17 (4), doi:10.5194/acp-17-2943-2017.

Lin, M., Malyshev, S., Shevliakova, E., Paulot, F., Horowitz, L. W., Fares, S., Mikkelsen, T. N., & Zhang, L. (2019). Sensitivity of ozone dry deposition to ecosystem-atmosphere interactions: A critical appraisal of observations and simulations. Global Biogeochemical Cycles, 33, 1264– 1288.

Lin, M., et al. (2020): Vegetation feedbacks during drought exacerbate ozone air pollution extremes in Europe. Nature Climate Change, 10(5), DOI:10.1038/s41558-020-0743-y.

Lin, Y., Dong, W., Zhang, M. et al. Causes of model dry and warm bias over central U.S. and impact on climate projections. Nat Commun 8, 881 (2017). https://doi.org/10.1038/s41467-017-01040-2

Liu, P., Hogrefe, C., Im, U., Christensen, J. H., Bieser, J., Nopmongcol, U., Yarwood, G., Mathur, R., Roselle, S., and Spero, T.: Attributing differences in the fate of lateral boundary ozone in AQMEII3 models to physical process representations, Atmos. Chem. Phys., 18, 17157–17175, https://doi.org/10.5194/acp-18-17157-2018, 2018.

Loeb, N. G., Doelling, D. R., Wang, H., Su, W., Nguyen, C., Corbett, J. G., Liang, L., Mitrescu, C., Rose, F. G., & Kato, S. (2018). Clouds and the Earth's radiant energy system (CERES) energy balanced and filled (EBAF) top-

of-atmosphere (TOA) edition-4.0 data product. Journal of Climate, 31(2), 895– 918. https://doi.org/10.1175/JCLI-D-17-0208.1

Makar, P. A. et al. The effects of forest canopy shading and turbulence on boundary layer ozone. Nat. Commun. 8, 15243, doi: 10.1038/ncomms15243 (2017).

Malyshev, S., Shevliakova, E., Stouffer, R. J., & Pacala, S. W. (2015). Contrasting local versus regional effects of land-use-change-induced heterogeneity on historical climate: Analysis with the GFDL Earth System Model. Journal of Climate, 28(13), 5448– 5469. https://doi.org/10.1175/Jcli-D-14-00586.1

Mass, C. F., and D. Ovens. 2019. The northern California wildfires of 8-9 October 2017: the role of a major downslope wind event. Bull. Am. Meteor. Soc. 100 (2):235-256. doi: 10.1175/bams-d-18-0037.1.

Mazoyer M, Burnet F, Denjean C, Roberts GC, Haeffelin M, Dupont JC, Elias T. Experimental study of the aerosol impact on fog microphysics. Atmos Chem Phys. 2019;19(7):4323–4344. doi: 10.5194/acp-19-4323-2019.

McDuffie, E. E., Smith, S. J., O'Rourke, P., Tibrewal, K., Venkataraman, C., Marais, E. A., Zheng, B., Crippa, M., Brauer, M., and Martin, R. V.: A global anthropogenic emission inventory of atmospheric pollutants from sector- and fuel-specific sources (1970–2017): an application of the Community Emissions Data System (CEDS), Earth Syst. Sci. Data, 12, 3413–3442, https://doi.org/10.5194/essd-12-3413-2020, 2020.

Morcrette, C. J., Van Weverberg, K., Ma, H.-Y., Ahlgrimm, M., Bazile, E., Berg, L. K., et al. (2018). Introduction to CAUSES: Description of weather and climate models and their near-surface temperature errors in 5 day hindcasts near the Southern Great Plains. Journal of Geophysical Research: Atmospheres, 123. https://doi.org/10.1002/2017JD027199

Murakami, Hiroyuki, May 2022: Substantial global influence of anthropogenic aerosols on tropical cyclones over the past 40 years. Science Advances, 8(19), DOI:10.1126/sciadv.abn9493.

Nie, W., Yan, C., Huang, D.D. et al. Secondary organic aerosol formed by condensing anthropogenic vapors over China's megacities. Nat. Geosci. 15, 255–261 (2022). https://doi.org/10.1038/s41561-022-00922-5

Nowell, H. K., C. D. Holmes, K. Robertson, C. Teske, and J. K. Hiers. 2018. A new picture of fire extent, variability, and drought interaction in prescribed fire landscapes: insights from Florida government records. Geophys. Res. Lett. 45 (15):7874-7884. doi: 10.1029/2018gl078679.

Office of Environmental Health Hazard Assessment (OEHHA, 2022). Indicators of Climate Change in California, Fourth Edition, California Environmental Protection Agency, OEHHA.

Okin, G.S., 2022. Where and how often does rain prevent dust emission? *Geophysical Research Letters*, *49* (4), e2021GL095501.

Paulot, F., Jacob, D. J., Pinder, R. W., Bash, J. O., Travis, K., & Henze, D. K. (2014). Ammonia emissions in the United States, European Union, and China derived by high-resolution inversion of ammonium wet deposition data: Interpretation with a new agricultural emissions inventory (MASAGE_NH3). Journal of Geophysical Research: Atmospheres, 119, 4343– 4364. https://doi.org/10.1002/2013JD021130

Paulot, F., Malyshev, S., Nguyen, T., Crounse, J. D., Shevliakova, E., & Horowitz, L. W. (2018). Representing sub-grid scale variations in nitrogen deposition associated with land use in a global Earth System Model:

Implications for present and future nitrogen deposition fluxes over North America. Atmospheric Chemistry and Physics, 18, 17,963– 17,978. https://doi.org/10.5194/acp-18-17963-2018

Paugam, R., M. Wooster, S. Freitas, and M. V. Martin (2016), A review of approaches to estimate wildfire plume injection height within large-scale atmospheric chemical transport models, Atmos. Chem. Phys., 16(2), 907-925, doi:10.5194/acp-16-907-2016

Pan, X., Ichoku, C., Chin, M., Bian, H., Darmenov, A., Colarco, P., et al. (2020). Six global biomass burning emission datasets: intercomparison and application in one global aerosol model. Atmospheric Chemistry and Physics, 20(2), 969-994. , https://doi.org/10.5194/acp-20-969-2020

Price, C., and D. Rind, 1994: Modeling global lightning distributions in a general circulation model. Mon. Wea. Rev., 122, 1930–1939, doi:10.1175/1520-0493 (1994)

Pfister, G. G., Walters, S., Lamarque, J.-F., Fast, J., Barth, M. C., Wong, J., et al. (2014). Projections of future summertime ozone over the U.S. Journal of Geophysical Research: Atmospheres, 119(9), 5559–5582. https://doi.org/10.1002/2013JD020932

Pfister, G. G., Eastham, S. D., Arellano, A. F., Aumont, B., Barsanti, K. C., Barth, M. C., et al. (2020). The Multi-Scale Infrastructure for Chemistry and Aerosols (MUSICA). Bulletin of the American Meteorological Society, 101(10), E1743– E1760. https://doi.org/10.1175/BAMS-D-19-0331.1

Possell, M., and Hewitt, C. N.: Isoprene emissions from plants are mediated by atmospheric CO_2 concentrations, Global Change Biology, 17, 1595-1610, 2011. doi: 10.1111/j.1365-2486.2010.02306.x

Prospero, J.M., 1996. Saharan dust transport over the North Atlantic Ocean and Mediterranean: An overview. *The impact of desert dust across the Mediterranean*, pp.133-151.

Pu, B. and Jin, Q.: A record-breaking trans-Atlantic African dust plume associated with atmospheric circulation extremes in June 2020, B. Am. Meteorol. Soc., 102, E1340–E1356, https://doi.org/10.1175/BAMS-D-21-0014.1, 2021

Pu et al. (2022), Compound heatwaves, drought, and dust events in California. Journal of Climate, 35 (24), 8133–8152, https://doi.org/10.1175/JCLI-D-21-0889.1

Putman, William M., and Shian-Jiann Lin, 2007: Finite-volume transport on various cubed-sphere grids. Journal of Computational Physics, 227(1), 55-78.

Rabin, S, B I Magi, Elena Shevliakova, and Stephen W Pacala, November 2015: Quantifying regional, time-varying effects of cropland and pasture on vegetation fire. Biogeosciences, 12(22), DOI:10.5194/bg-12-6591-2015.

Randerson, J.T., G.R. van der Werf, L. Giglio, G.J. Collatz, and P.S. Kasibhatla. 2018. Global Fire Emissions Database, Version 4.1 (GFEDv4). ORNL DAAC, Oak Ridge, Tennessee, USA. https://doi.org/10.3334/ORNLDAAC/1293

Rasmussen, D J, A. M Fiore, V. Naik, L. W Horowitz, S J McGinnis, and M G Schultz, February 2012: Surface ozone-temperature relationships in the eastern US: A monthly climatology for evaluating chemistry-climate models. Atmospheric Environment, 47, DOI:10.1016/j.atmosenv.2011.11.021.

Roberts, M. J., Camp, J., Seddon, J., Vidale, P. L., Hodges, K., Vannière, B., ... & Wu, L. (2020). Projected future changes in tropical cyclones using the CMIP6 HighResMIP multimodel ensemble. Geophysical research letters, 47(14), e2020GL088662.

Rydsaa, J. H., Stordal, F., Gerosa, G., Finco, A. & Hodnebrog, O. Evaluating stomatal ozone fluxes in WRF-Chem: comparing ozone uptake in Mediterranean ecosystems. Atmos. Environ. 143, 237–248 (2016).

Sayer, A. M., Munchak, L. A., Hsu, N. C., Levy, R. C., Bettenhausen, C., & Jeong, M. J. (2014). MODIS Collection 6 aerosol products: Comparison between Aqua's e-deep blue, dark target, and "merged"data sets, and usage recommendations. Journal of Geophysical Research: Atmospheres,119, 13,965–13,989. https://doi.org/10.1002/2014JD022453

Schultz, M. G., Schröder, S., Lyapina, O., Cooper, O., Galbally, I., et al. (2017). Tropospheric ozone assessment report: Database and metrics data of global surface ozone observations. Elementa: Science of the Anthropocene, 5(0). https://doi.org/10.1525/elementa.244

Schumacher, R.S., Rasmussen, K.L. The formation, character and changing nature of mesoscale convective systems. Nat Rev Earth Environ 1, 300–314 (2020). https://doi.org/10.1038/s43017-020-0057-7

Schwantes, R. H., Lacey, F. G., Tilmes, S., Emmons, L. K., Lauritzen, P. H., Walters, S., et al. (2022). Evaluating the impact of chemical complexity and horizontal resolution on tropospheric ozone over the conterminous US with a global variable resolution chemistry model. Journal of Advances in Modeling Earth Systems, 14, e2021MS002889. https://doi.org/10.1029/2021MS002889

Silva, S. J., & Heald, C. L. (2018). Investigating dry deposition of ozone to vegetation. Journal of Geophysical Research: Atmospheres, 123, 559– 573. https://doi.org/10.1002/2017jd027278

Sindelarova, K., Markova, J., Simpson, D., Huszar, P., Karlicky, J., Darras, S., and Granier, C.: High-resolution biogenic global emission inventory for the time period 2000–2019 for air quality modeling, Earth Syst. Sci. Data, 14, 251–270, https://doi.org/10.5194/essd-14-251-2022, 2022.

Sharkey, T. D. and Monson, R. K.: The future of isoprene emission from leaves, canopies and landscapes, Plant Cell Environ., 37, 1727–1740, https://doi.org/10.1111/pce.12289, 2014.

Shevliakova, E., Pacala, S. W., Malyshev, S., Hurtt, G. C., Milly, P. C. D., Caspersen, J. P., Sentman, L. T., Fisk, J. P., Wirth, C., & Crevoisier, C. (2009). Carbon cycling under 300 years of land use change: Importance of the secondary vegetation sink. Global Biogeochemical Cycles, 23, GB2022. https://doi.org/10.1029/2007gb003176

Stanier, C.O., Pierce, R.B., Abdi-Oskouei, M., Adelman, Z.E., Al-Saadi, J., Alwe, H.D., Bertram, T.H., Carmichael, G.R., Christiansen, M.B., Cleary, P.A., Czarnetzki, A.C., Dickens, A.F., Fuoco, M.A., Hughes, D.D., Hupy, J.P., Janz, S.J., Judd, L.M., Kenski, D., Kowalewski, M.G., Long, R.W., Millet, D.B., Novak, G., Roozitalab, B., Shaw, S.L., Stone, E.A., Szykman, J., Valin, L., Vermeuel, M., Wagner, T.J., Whitehill, A.R., 2021. Overview of The lake Michigan ozone study 2017. Bull. Am. Meteorol. Soc. https://doi.org/10.1175/BAMS-D-20-0061.1.

Sun C. and Liang X.-Z. (2023) Understanding and Reducing Warm and Dry Summer Biases in the Central United States: Improving Cumulus Parameterization, 2015–2034, https://doi.org/10.1175/JCLI-D-22-0254.1

Suzuki, K., JC Golaz, GL Stephens: Evaluating cloud tuning in a climate model with satellite observations Geophysical Research Letters, 2013.

Tai, Amos P. K., Loretta J. Mickley, Colette L. Heald, and Shiliang Wu. Effect of CO2 inhibition on Biogenic Isoprene Emission: Implications for Air Quality Under 2000 to 2050 Changes in Climate, Vegetation, and Land Use. Geophys. Res. Lett. 40 (13), 3479–3483, 2013.
https://agupubs.onlinelibrary.wiley.com/doi/full/10.1002/grl.50650

Tang, Q., Klein, S. A., Xie, S., Lin, W., Golaz, J.-C., Roesler, E. L., Taylor, M. A., Rasch, P. J., Bader, D. C., Berg, L. K., Caldwell, P., Giangrande, S. E., Neale, R. B., Qian, Y., Riihimaki, L. D., Zender, C. S., Zhang, Y., and Zheng, X.: Regionally refined test bed in E3SM atmosphere model version 1 (EAMv1) and applications for high-resolution modeling, Geosci. Model Dev., 12, 2679–2706, https://doi.org/10.5194/gmd-12-2679-2019, 2019.

Tang, Q., Golaz, J.-C., Van Roekel, L. P., Taylor, M. A., Lin, W., Hillman, B. R., Ullrich, P. A., Bradley, A. M., Guba, O., Wolfe, J. D., Zhou, T., Zhang, K., Zheng, X., Zhang, Y., Zhang, M., Wu, M., Wang, H., Tao, C., Singh, B., Rhoades, A. M., Qin, Y., Li, H.-Y., Feng, Y., Zhang, Y., Zhang, C., Zender, C. S., Xie, S., Roesler, E. L., Roberts, A. F., Mametjanov, A., Maltrud, M. E., Keen, N. D., Jacob, R. L., Jablonowski, C., Hughes, O. K., Forsyth, R. M., Di Vittorio, A. V., Caldwell, P. M., Bisht, G., McCoy, R. B., Leung, L. R., and Bader, D. C.: The fully coupled regionally refined model of E3SM version 2: overview of the atmosphere, land, and river results, Geosci. Model Dev., 16, 3953–3995, https://doi.org/10.5194/gmd-16-3953-2023, 2023.

Tang, W., Gabriele G. Pfister, Rajesh Kumar, Mary Barth, David P. Edwards, Louisa K. Emmons, Simone Tilmes, Capturing High-Resolution Air Pollution Features Using the Multi-Scale Infrastructure for Chemistry and Aerosols Version 0 (MUSICAv0) Global Modeling System, Journal of Geophysical Research: Atmospheres, 10.1029/2022JD038345, 128, 7, (2023).

Thiery, W., Davin, E. L., Lawrence, D. M., Hirsch, A. L., Hauser, M., & Seneviratne, S. I. (2017). Present-day irrigation mitigates heat extremes. Journal of Geophysical Research: Atmospheres, 122(3), 1403– 1422. https://doi.org/10.1002/2016jd025740

Thornhill, G. D., Collins, W. J., Kramer, R. J., Olivié, D., Skeie, R. B., O'Connor, F. M., ... & Zhang, J. (2021). Effective radiative forcing from emissions of reactive gases and aerosols–a multi-model comparison. *Atmospheric Chemistry and Physics*, *21*(2), 853-874.

Torregrosa, A., O'Brien, T. A., & Faloona, I. C. (2014). Coastal fog, climate change, and the environment. Eos, Transactions American Geophysical Union, 95(50), 473– 474. https://doi.org/10.1002/2014EO500001

Turnock, S. T., Allen, R. J., Andrews, M., Bauer, S. E., Deushi, M., Emmons, L., Good, P., Horowitz, L., John, J. G., Michou, M., Nabat, P., Naik, V., Neubauer, D., O'Connor, F. M., Olivié, D., Oshima, N., Schulz, M., Sellar, A., Shim, S., Takemura, T., Tilmes, S., Tsigaridis, K., Wu, T., and Zhang, J.: Historical and future changes in air pollutants from CMIP6 models, Atmos. Chem. Phys., 20, 14547–14579, https://doi.org/10.5194/acp-20-14547-2020, 2020.

United Nations Environmental Program (UNEP), World Meteorological Organization (WMO), UNCCD (2016). Global Assessment of Sand and Dust Storms. Edited by Gemma Shepherd. ISBN: 978-92-807-3551-2.

United States Environmental Protection Agency (2016). The Final 2016 Exceptional Events Rule, Supporting Guidance Documents, Updated FAQs, and Other Rule Implementation Resources. https://www.epa.gov/air-quality-analysis/final-2016-exceptional-events-rule-supporting-guidance-documents-updated-faqs

United States Environmental Protection Agency (2022). CMAQ (Version 5.4) [Software]. Available from https://doi.org/10.5281/zenodo.7218076

Val Martin, M., Kahn, R., & Tosca, M. (2018). A global analysis of wildfire smoke injection heights derived from space-based multi-angle imaging. Remote Sensing, 10(10), 1609. https://doi.org/10.3390/rs10101609

van Marle, M. J. E., Kloster, S., Magi, B. I., Marlon, J. R., Daniau, A.-L., Field, R. D., Arneth, A., Forrest, M., Hantson, S., Kehrwald, N. M., Knorr, W., Lasslop, G., Li, F., Mangeon, S., Yue, C., Kaiser, J. W., & van der Werf, G. R. (2017). Historic global biomass burning emissions based on merging satellite observations with proxies and fire models (1750-2015). Geoscientific Model Development, 10(9), 3329–3357. https://doi.org/10.5194/gmd-2017-32

Wang, R., Guo, X., Pan, D., Kelly, J.T., Bash, J. O., Sun, K., Paulot, F., Clarisse, L., Van Damme, M., Whitburn, S., Coheur, P.-F., Clerbaux, C. and Zondlo, M.A., 2020, Monthly patterns of ammonia over the contiguous United States at 2 km resolution, Geophys. Res. Lett., doi:10.1029/2020GL090579.

Ward, Daniel S., Elena Shevliakova, Sergey Malyshev, and S Rabin, January 2018: Trends and variability of global fire emissions due to historical anthropogenic activities. Global Biogeochemical Cycles, 32(1), DOI:10.1002/2017GB005787.

Ward, Daniel S., Elena Shevliakova, Sergey Malyshev, M Kuwata, and Andrew T Wittenberg, December 2016: Variability of fire emissions on interannual to multi-decadal timescales in two Earth System models. Environmental Research Letters, 11(12), DOI:10.1088/1748-9326/11/12/125008.

Warner, J. X., R. R. Dickerson, Z. Wei,L. L. Strow, Y. Wang, and Q. Liang (2017), Increased atmospheric ammonia over the world's major agricultural areas detected from space,Geophys. Res. Lett.,44, 2875–2884, doi:10.1002/2016GL072305.

Westerling, A. L., H. G. Hidalgo, D. R. Cayan, T. W. Swetnam, Warming and earlier spring increase western U.S. forest wildfire activity. Science 313, 940–943 (2006).

Womack, C. C., McDuffie, E. E., Edwards, P. M., Bares, R., de Gouw, J. A.,Docherty, K. S., et al. (2019). An odd oxygen framework for wintertime ammonium nitrate aerosol pollution in urban areas: NOxand VOC control as mitigation strategies. Geophysical Research Letters,46, 4971–4979. https://doi.org/10.1029/2019GL082028

Xie, Y., Lin, M., & Horowitz, L. W. (2020). Summer $PM_{2.5}$ pollution extremes caused by wildfires over the western United States during 2017–2018.Geophysical ResearchLetters,47, e2020GL089429. https://doi.org/10.1029/2020GL089429

Xie, Y., Lin, M., and Bertrand Decharme et al. Tripling of western US particulate pollution from wildfires in a warming climate. Proc. Natl Acad. Sci. USA 119, e2111372119 (2022).

Xu, L., J.D. Crounse, and K.T. Vasquez et al., Ozone Chemistry in Western U.S. Wildfire Plumes. Science Advances, 7 (50), 2021, DOI: 10.1126/sciadv.abl3648

Xu, Z., Di Vittorio, A., Zhang, J., Rhoades, A., Xin, X., Xu, H., & Xiao, C. (2021). Evaluating variable-resolution CESM over China and western United States for use in water-energy nexus and impacts modeling. Journal of Geophysical Research: Atmospheres, 126, e2020JD034361. https://doi.org/10.1029/2020JD034361

Yao, Y., Vanderkelen, I., Lombardozzi, D., Swenson, S., Lawrence, D., Jägermeyr, J., et al. (2022). Implementation and evaluation of irrigation techniques in the community land model. Journal of Advances in Modeling Earth Systems, 14(12), e2022MS003074. https://doi.org/10.1029/2022MS003074

Yu, H., Tan, Q., Zhou, L., Zhou, Y., Bian, H., Chin, M., Ryder, C. L., Levy, R. C., Pradhan, Y., Shi, Y., Song, Q., Zhang, Z., Colarco, P. R., Kim, D., Remer, L. A., Yuan, T., Mayol-Bracero, O., and Holben, B. N.: Observation and modeling of the historic "Godzilla" African dust intrusion into the Caribbean Basin and the southern US in June 2020, Atmos. Chem. Phys., 21, 12359–12383, https://doi.org/10.5194/acp-21-12359-2021, 2021

Yu, Y. and P. Ginoux 2022: Enhanced dust emission following large wildfires due to vegetation disturbance. Nat. Geosci., 15, 878– 884, https://doi.org/10.1038/s41561-022-01046-6.

Yuan, H., Dai, Y., Li, S., 2020. Reprocessed MODIS Version 6 Leaf Area Index data sets for land surface and climate modeling. Sun Yat-sen University. http://globalchange.bnu.edu.cn/research/laiv6

Yuan, H., Dai, Y., Xiao, Z., Ji, D., Shangguan, W., 2011. Reprocessing the MODIS Leaf Area Index Products for Land Surface and Climate Modelling. Remote Sensing of Environment, 115(5), 1171-1187. doi:10.1016/j.rse.2011.01.001

Zeng, Yujin, P C D Milly, Elena Shevliakova, Sergey Malyshev, M H J Van Huijgevoort, and Krista A Dunne, March 2022: Possible anthropogenic enhancement of precipitation in the Sahel-Sudan savanna by remote agricultural irrigation. Geophysical Research Letters, 49(6), DOI:10.1029/2021GL096972.

Zhang, C., Xie, S., Klein, S. A., Ma, H.-Y., Tang, S., Van Weverberg, K., et al. (2018). CAUSES: Diagnosis of the summertime warm bias in CMIP5 climate models at the ARM Southern Great Plains site. Journal of Geophysical Research: Atmospheres, 123, https://doi.org/10.1002/2017JD027200

Zhang, L., Lin, M., Langford, A. O., Horowitz, L. W., Senff, C. J., Klovenski, E., Wang, Y., Alvarez II, R. J., Petropavlovskikh, I., Cullis, P., Sterling, C. W., Peischl, J., Ryerson, T. B., Brown, S. S., Decker, Z. C. J., Kirgis, G., and Conley, S.: Characterizing sources of high surface ozone events in the southwestern US with intensive field measurements and two global models, Atmos. Chem. Phys.,20, 10379–10400, https://doi.org/10.5194/acp-20-10379-2020, 2020.

Zhang Q, et al. Drivers of improved PM2.5 air quality in China from 2013 to 2017. P Natl Acad Sci Usa. 2019;116:24463–24469. doi: 10.1073/pnas.1907956116.

Zhao, M., Golaz, J.-C., Held, I.M., et al. (2018a). The GFDL global atmosphere and land model AM4.0/LM4.0: 1. Simulation characteristics with prescribed SSTs. Journal of Advances in Modeling Earth Systems, 10(3), 691–734. https://doi.org/10.1002/2017MS001208

Zhao, M., Golaz, J.-C., Held, I. M., et al. (2018b). The GFDL global atmosphere and land model AM4.0/LM4.0: 2. Model description, sensitivity studies, and tuning strategies. Journal of Advances in Modeling Earth Systems, 10. https://doi.org/10.1002/2017MS001209

Zhao, M., Held, I. M., & Lin, S.-J. (2012). Some counterintuitive dependencies of tropical cyclone frequency on parameters in a GCM. Journal of the Atmospheric Sciences, 69, 2272–2283.

Zhao, Ming, January 2022: A study of AR-, TS-, and MCS-associated precipitation and extreme precipitation in present and warmer climates. Journal of Climate, 35(2), DOI:10.1175/JCLI-D-21-0145.1479-497.

Zheng, B., Tong, D., Li, M., Liu, F., Hong, C., Geng, G., Li, H., Li, X., Peng, L., Qi, J., Yan, L., Zhang, Y., Zhao, H., Zheng, Y., He, K., and Zhang, Q.: Trends in China's anthropogenic emissions since 2010 as the consequence of clean air actions, Atmos. Chem. Phys., 18, 14095–14111, https://doi.org/10.5194/acp-18-14095, 2018.

Zheng, Y., Horowitz, L. W., Menzel, R., Paynter, D. J., Naik, V., Li, J., and Mao, J.: Anthropogenic amplification of biogenic secondary organic aerosol production, EGUsphere [preprint], https://doi.org/10.5194/egusphere-2023-372, 2023.

Zhou, L, S-J Lin, J-H Chen, L. Harris, X Chen, and S. L Rees (2019): Toward Convective-Scale Prediction within the Next Generation Global Prediction System. Bulletin of the American Meteorological Society, 100(7), DOI:10.1175/BAMS-D-17-0246.1.

Figures Captions

Figure 1. Grid structure and local grid cell widths (shading, units: km) for c96 uniform grid in AM4.1 configuration and c256 stretched grid centered at 32.0N and 97.6W for AM4VR configuration. The notation *cN* refers to a cubed-sphere grid with *N x N* grid cells on each of its six faces (bounded by thick black lines). The AM4VR resolution is highest along the coastal US on the corner of the cubed-sphere face. Thin lines are the boundaries of every 32 x 32 grid cells.

Figure 2. Comparisons of BVOC emissions computed in AMIP simulations with AM4.1 (100 km) and AM4VR (13 km, with updated land cover and EP maps): (a-b) long-term JJA mean isoprene emission fluxes; (c-d) annual mean monoterpenes emission fluxes; and (e-f) annual mean emission fluxes for other BVOCs. The annual totals for the domain, as well as interannual standard deviations for the 2000-2014 period, are reported on each graph.

Figure 3. Comparisons of biogenic isoprene emissions over the southeast US in August-September 2013 from the OMI inversion (25 km; Kaiser et al., 2018) with those computed in AM4.1 (100 km) and AM4VR (13 km, with updated land cover and EP maps). Total isoprene emissions (in TgC) for the southeast US domain are reported.

Figure 4. (a-e) Comparison of regional anthropogenic emissions of BC, OM, SO_2, NO and total NMVOCs used in AM4.1 (CEDS v2017-05-18) and AM4VR (CEDS v2021-04-21) for China (20N-45N, 100E-125E), Europe (40N-60N,10W-25E), and US (30N-50N, 123W-65W). The purple stars in (a-b) denote estimates from the US NEI2017. (f) Comparison of global total biomass burning emissions of oxygenated VOCs in AM4.1 and AM4VR (Text S4).

Figure 5. (a-d) Long-term annual mean precipitation (mm day^{-1}) from observation-based estimates from IMERG (0.1°, 2000-2020) and GPCP (1°, 1985-2015) and from the AM4VR (regridded to 50km globally, ε_1 = 0.5 km^{-1}) and C96 (100 km, ε_1 = 0.9 km^{-1}) AMIP simulations (1990-2020). (e-f) Differences between simulated results and GPCP estimates. (g-h) Fraction of parameterized deep convective precipitation.

Figure 6. (a-f) Model bias in long-term annual mean TOA outgoing longwave radiation, shortwave absorption, and net radiative flux (W/m^2) in comparison with satellite estimates from CERES-EBAF-Ed4.2. Results are shown from AM4VR with ε_1 = 0.6 km^{-1} and C96 with ε_1 = 0.9 km^{-1}.

Figure 7. US annual mean precipitation (mm day^{-1}) for 1990-2020 from AM4VR (13 km, ε_1 = 0.6 km^{-1}) and C96 (100 km, ε_1 = 0.9 km^{-1}) AMIP simulations and PRISM observations (4 km), and differences between simulated and observed precipitation. The boxes on the PRISM map denotes select regions for analyses in Figs. 9-10.

Figure 8. Long-term mean March snowpack climatology over the western US from 25 km gridded observations (Kapnick et al., 2018), AM4VR (13 km), and C96 (100 km) AMIP simulation.

Figure 9. Monthly climatology (1990-2020) of precipitation (mm day^{-1}) from PRISM observations (black), C96 (ε_1 = 0.9 km−1, green), and AM4VR AMIP simulations with ε_1 = 0.5 (orange) and 0.6 km^{-1} (red) for the Pacific Northwest, the Southwest. the Great Plains, and the Southeast US. The vertical bars represent interannual standard deviations. Correlations between observed and simulated total precipitation as well as the percentage of large-scale precipitation (dashed lines) for JJAS are reported.

Figure 10. (a-d) Probability distribution of regionally averaged daily precipitation for the Pacific Northwest in DJF, the Southwest in JAS, and the Central and Southeast US in JJAS from PRISM observations and AM4 AMIP simulations. The median (q50), the 90th percentile (q90), and standard deviations (σ) are shown (mm day^{-1}). (e-f) Diurnal cycle of JJAS mean precipitation (mm hr^{-1}) for the Central and Southeast US from IMERG observations (black) and AM4 AMIP simulations at 100 km (green), 25 km (blue), and 13 km resolution (red and orange). The dotted lines show parameterized precipitation.

Figure 11. (Left) JJAS precipitation from PRISM observations (4 km) and model biases for C96 (100 km) and two AM4VR (13 km) AMIP simulations with ε_1 = 0.5 and 0.6 km^{-1}, respectively; (Right) Long-term mean annual consecutive dry days calculated from PRISM observations and model simulations.

Figure 12. (Top) US JJAS mean daily maximum 2m temperature (°C) for 1990-2020 from AM4VR (13 km, ε_1 = 0.6 km^{-1}) and C96 (100 km) AMIP simulations; (Middle) PRISM observations (4 km); (Bottom) Differences between simulated and observed results.

Figure 13. Monthly climatology (2000-2014) of aerosol optical depth simulated by AM4.1 (blue line), C96 (green line) and AM4VR (red line) and measured by MODIS (TERRA: star, AQUA: cross) and MISR (filled circles) satellite instruments. Each panel represents a spatial average over the corresponding region on the background map. The vertical bars represent the contribution from different aerosol components in AM4VR simulation. The numbers in each box show the correlation coefficients (left) and normalized root mean square error (right) compared to MODIS-AQUA.

Figure 14. Comparison of fine dust vertical profiles (μg m^{-3}) from ATom aircraft measurements (blue; 2016-2018), C96 (green) and AM4VR (red) AMIP simulations (2000-2014 monthly climatology) sampled along the ATom campaigns flight track in northern mid-latitudes (30°N to 60°N), tropics (30°S to 30°N), and southern mid-latitudes (30°S to 60°S). The box represents the 25th percentile, median, and 75th percentile of data points for each 2 km altitude bins, and the whiskers extend to the minimum and maximum values, excluding the outliers. Median absolute error is reported.

Figure 15. Comparison of simulated AOD (550 nm) with AERONET observations over the 2000-2014 period for AM4.1 and AM4VR AMIP simulation. Sites with at least 5 years of observations are shown.

Figure 16. As in Fig. 13 but for CONUS.

Figure 17. Tropospheric HCHO columns during JJA 2018-2020 retrieved from TROPOMI (bias-corrected, regridded to 13 km) and computed from AM4VR (nudged, 13km) sampled on TROPOMI overpass time (1:30PM). The mean value over the SEUS (box on map), as well as standard deviation across the nine months in JJA 2018-2020, is reported on each graph.

Figure 18. JJA mean surface organic matter (OM) concentrations (μg m^{-3}) for 1995-2014 from IMPROVE observations, AM4VR and AM4.1 simulations (a,b,f), along with the simulated contributions from biogenic SOA (c,g) and from anthropogenic and biomass burning emissions (d,h). Also shown is observed and simulated monthly climatology (1995-2014) of OM for the southeast US (box on map), with the vertical bars representing interannual standard deviations (e). JJA mean values for the Southeast are reported on the top right corner of (a), (b), and (f).

Figure 19. (a-b) Monthly climatology (1995-2014) of surface OM and NH_4NO_3 aerosol concentrations in the Midwest US from IMPROVE observations and model simulations. The vertical bars represent

interannual standard deviation. (c) Springtime climatology of NH_4NO_3 aerosol concentrations from AQS observations and AM4VR simulation.

Figure 20. (a) Monthly climatology of surface sulfate concentrations in the Eastern US for 1995-2009 versus 2010-2020 from IMPROVE observations and AM4VR simulations. Results from C96 and AM4.1 for the 1995-2009 period are also shown for comparison. (b) Time series of monthly mean sulfate concentrations from 1995 to 2020 from observations and model simulations.

Figure 21. Summer $PM_{2.5}$ concentrations in US surface air averaged over 2000-2014 from IMPROVE and AQS observations and from model simulations. The observed-model correlations (r) and means (mn) sampled at IMPROVE sites are reported. For illustrative purposes, AQS sites with $PM_{2.5}$ greater than 17 $\mu g/m^3$ are plotted as larger circles.

Figure 22. (a) Monthly climatology (1995-2014) of surface fine dust concentrations at IMPROVE sites in Arizona (box on map) from observations and model simulations. The vertical bars represent interannual standard deviation. (b) Difference in top 15-cm soil moisture between AM4VR and C96 (regridded to 50 km for comparison) for March-April and July-August, respectively.

Figure 23. (a) Monthly climatology (1995-2014) of surface fine dust concentrations in the Southeast US from IMPROVE observations and AMIP simulations with AM4.1, C96, and AM4VR. The vertical bars represent interannual standard deviation. (b) Climatology (1990-2020) of JJA mean dust optical depth in AM4VR AMIP simulation. (c) Surface concentrations of 24-h average $PM_{2.5}$ on June 26-27, 2020 from AQS observations (filled circles) and an AM4VR nudged simulation.

Figure 24. Summer mean surface daily maximum 8-hour average (MDA8) ozone (ppb) for the northern hemisphere from observations, AM4.1 (100 km) and AM4VR (remapped to 50 km globally) AMIP simulations (2000-2014) sampled in the lowest model layer. Differences between AM4VR and AM4.1, the rmse and model means (mn) sampled at observational sites are shown.

Figure 25. (a-b) Differences from AM4.1 for long-term JJA mean MDA8 ozone in C96 and AM4VR AMIP simulations sampled in the lowest model layer. (c) Differences in summer daytime (9-15 Local Time) mean ozone dry deposition velocities ($V_{d,O3}$) to secondary vegetation between AM4VR and C96 AMIP simulations. (d) Summer daytime mean $V_{d,O3}$ averaged across all land-cover types simulated in AM4VR. The color-coded symbols denote values derived from ozone flux measurements for forests (circles), croplands (triangles), and grasslands (squares). (e-f) JJA mean MDA8 ozone from AQS observations and AM4VR computed at the 2m level (Text S7).

Figure 26. (a) JJA mean surface MDA8 ozone for 2000-2014 from observations, AM4.1 (100 km) sampled in the lowest model layer, and AM4VR (13 km) computed at the 2m level. Spatial correlations between observed and simulated results are reported. (b) Probability distributions for observed and simulated JJA daily MDA8 ozone sampled in the lowest model layer at sites in Southern California (32.5-37.5N; 120-114W). The median (q50), the 90th percentile (q90), standard deviation (σ), and the percentage of site-days with MDA8 ozone $\geq$70 ppb (D70) are shown.

Figure 27. Surface concentrations of DJF 24-h average NO_2, DJF 24-h average ozone, and JJA 24-h average ozone in California during 2000-2014 from observations and model simulations sampled in the lowest model layer.

Figure 28. Wintertime (DJF) surface concentrations of total $PM_{2.5}$ and NH_4NO_3 aerosols in California during 2000-2020 from observations (25 km), C96 (100 km) and AM4VR (13 km) AMIP simulations. The circles denote locations of Fresno and Visalia analysed in Fig. 29.

Figure 29. Monthly mean $PM_{2.5}$ and NH_4NO_3 aerosols sampled at Fresno and Visalia in the San Joaquin Valley for 2000-2010 and 2011-2020 from observations and model simulations. The vertical bars represent interannual standard deviations.

Figure 30. Wintertime (DJF) precipitation and 2 m relative humidity in California averaged over 1990-2020 from PRISM observation-based estimates (4 km), C96 (100 km) and AM4VR (13 km) AMIP simulations.

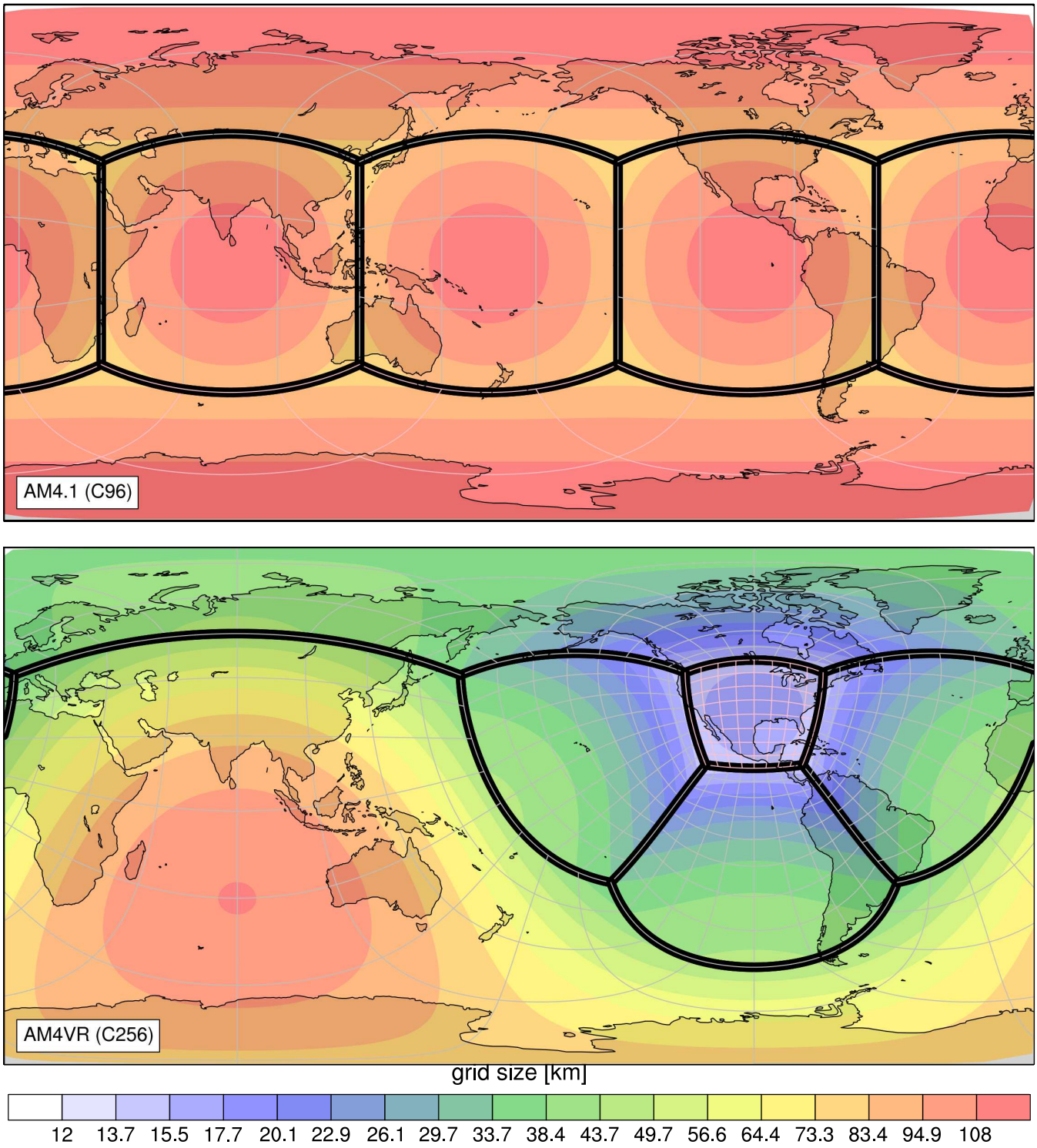

Figure 1. Grid structure and local gridcell widths (shading, units: km) for c96 uniform grid in AM4.1 configurations and c256 stretched grid centered at 32.0N and 97.6W for AM4VR configurations. The notation cN refers to a cubed-sphere grid with N x N grid cells on each of its six faces (bounded by thick black lines). The AM4VR resolution is highest along the coastal US on the corner of the cubed-sphere face. Thin lines are the boundaries of every 32 x 32 grid cells.

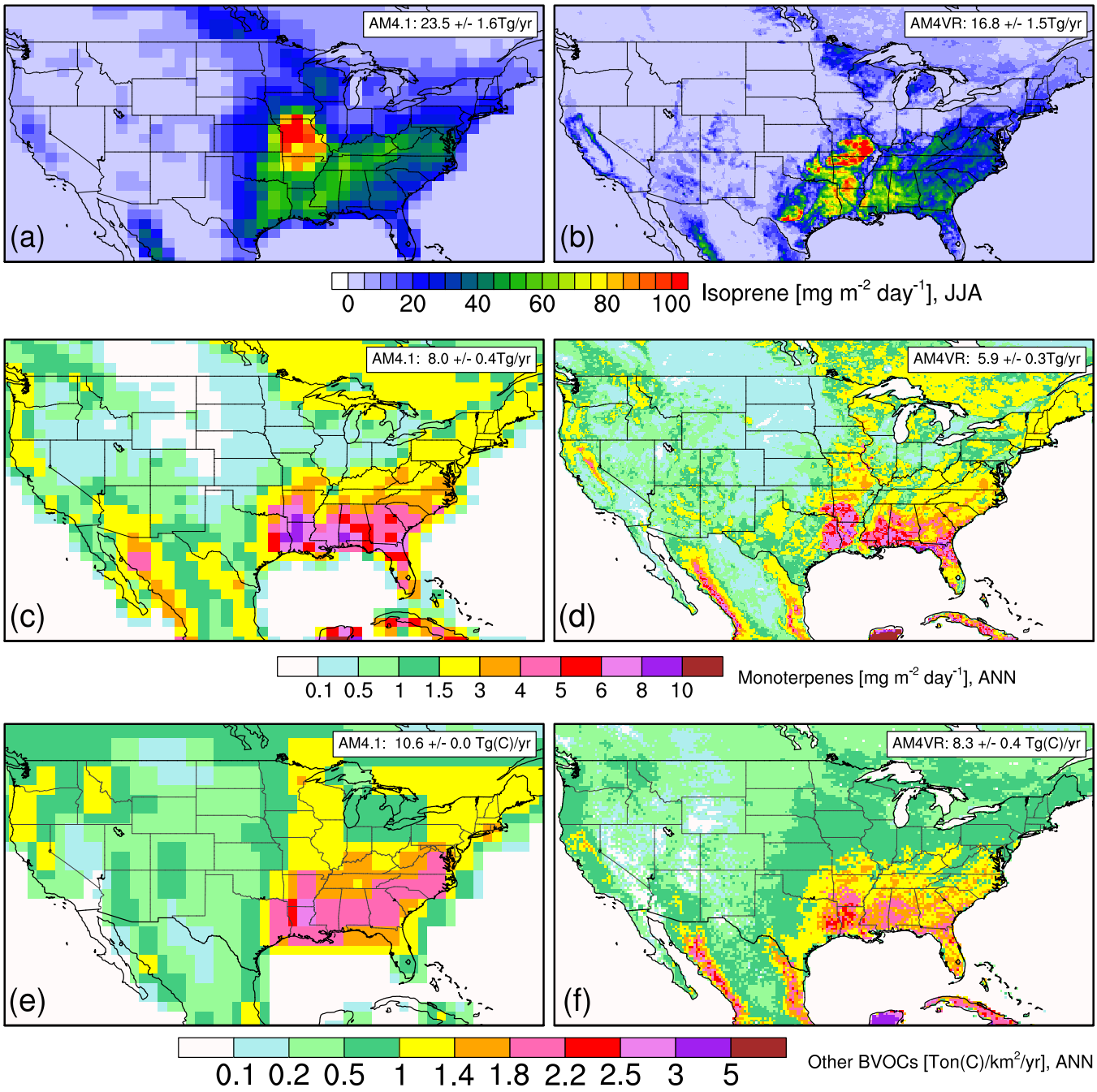

Figure 2. Comparisons of BVOC emissions computed in AMIP simulations with AM4.1 (100 km) and AM4VR (13 km, with updated land cover and EP maps): (a-b) long-term JJA mean isoprene emission fluxes; (c-d) annual mean monoterpenes emission fluxes; and (e-f) annual mean emission fluxes for other BVOCs. The annual totals for the domain, as well as interannual standard deviations for the 2000-2014 period, are reported on each graph.

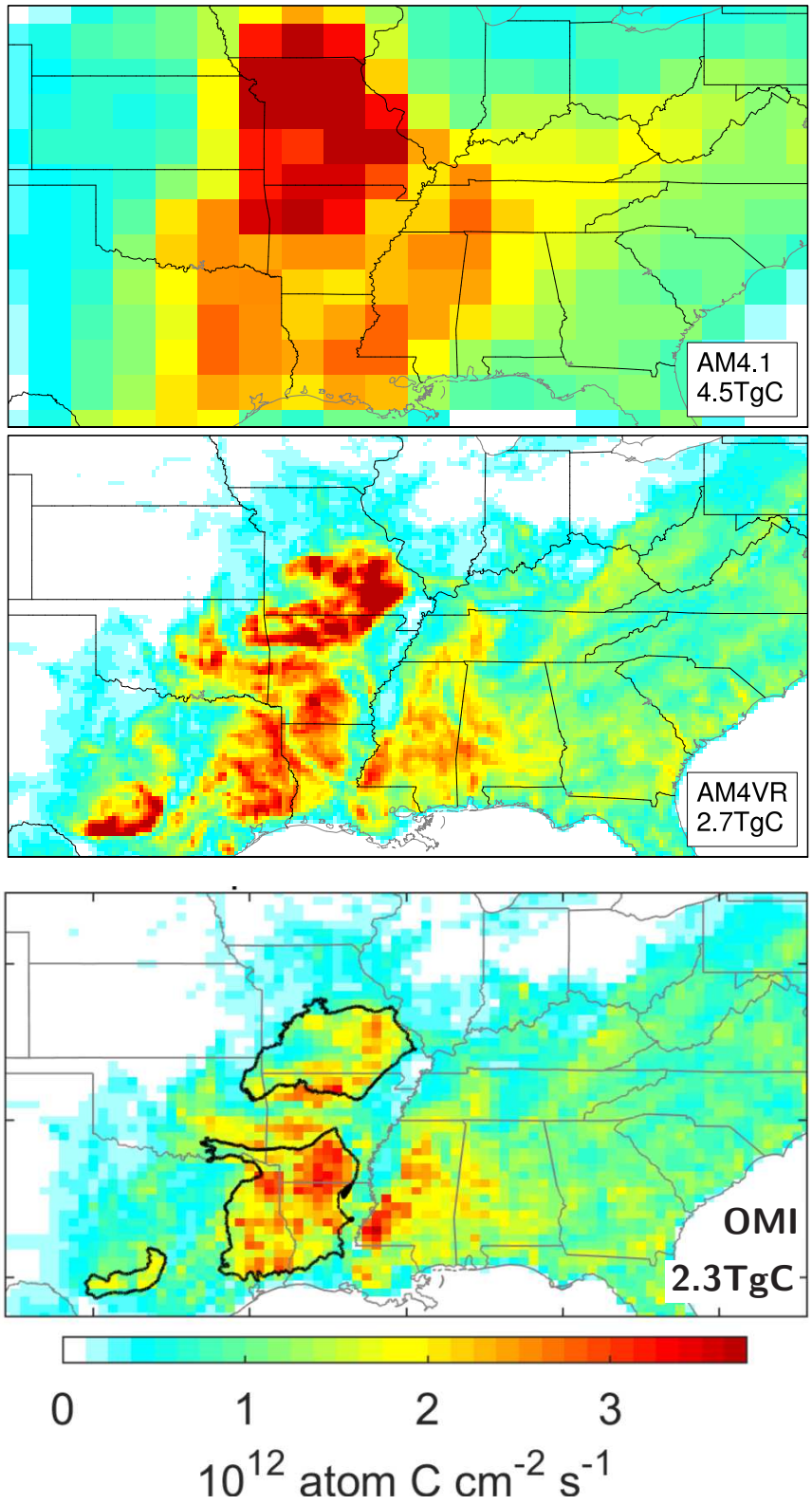

Figure 3. Comparisons of biogenic isoprene emissions over the southeast US in August-September 2013 from the OMI inversion (25 km; Kaiser et al., 2018) with those computed in AM4.1 (100 km) and AM4VR (13 km, with updated land cover and EP maps). Total isoprene emissions (in TgC) for the southeast US domain are reported.

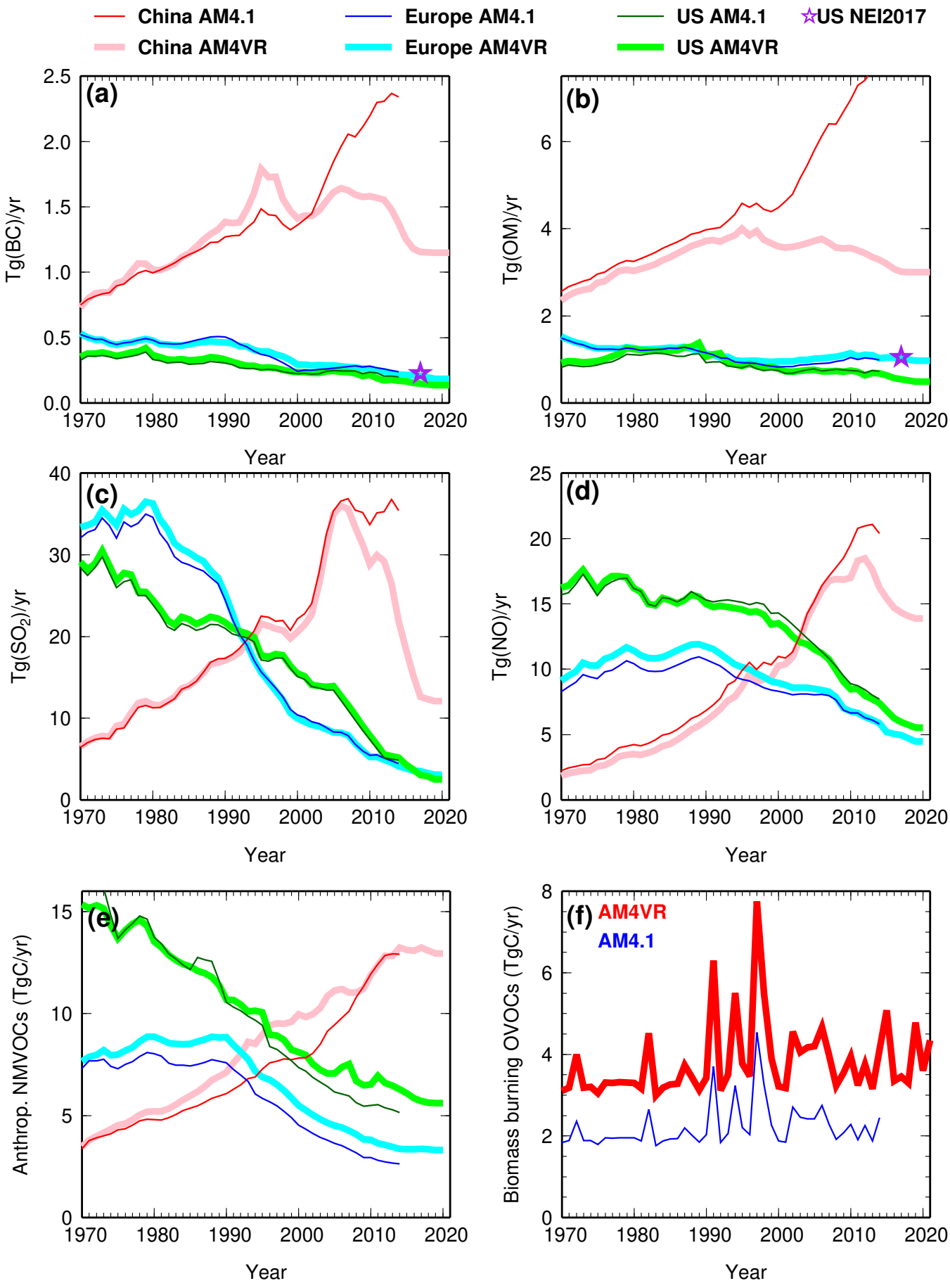

Figure 4. (a-e) Regional anthropogenic emissions of BC, OM, SO_2, NO and total NMVOCs used in AM4.1 (CEDS v2017-05-18) and AM4VR (CEDS v2021-04-21) for China (20N-45N, 100E-125E), Europe (40N-60N, 10W-25E), and US (30N-50N, 123W-65W). The purple stars in (a-b) denote estimates from the US NEI2017. (f) Comparison of global total biomass burning emissions of oxygenated VOCs in AM4.1 and AM4VR (Text S4).

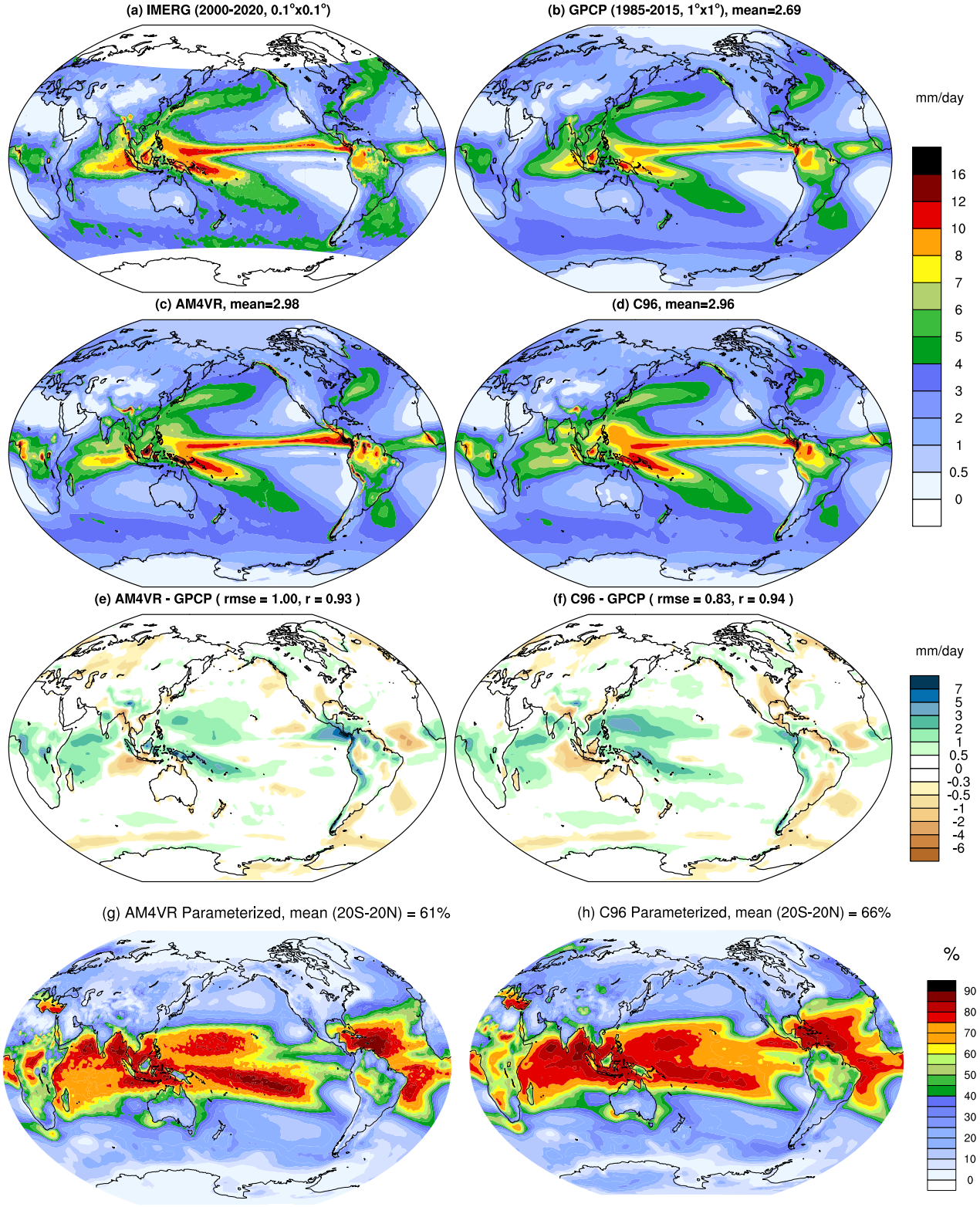

Figure 5. (a-d) Long-term annual mean precipitation (mm day^{-1}) from observation-based estimates from IMERG (0.1^o, 2000-2020) and GPCP (1^o, 1985-2015) and from the AM4VR (regridded to 50km globally, ϵ_1 = 0.5 km^{-1}) and C96 (100 km, ϵ_1 = 0.9 km^{-1}) AMIP simulations for 1990-2020. (e-f) Differences between simulated results and GPCP estimates. (g-h) Fraction of parameterized deep convective precipitation.

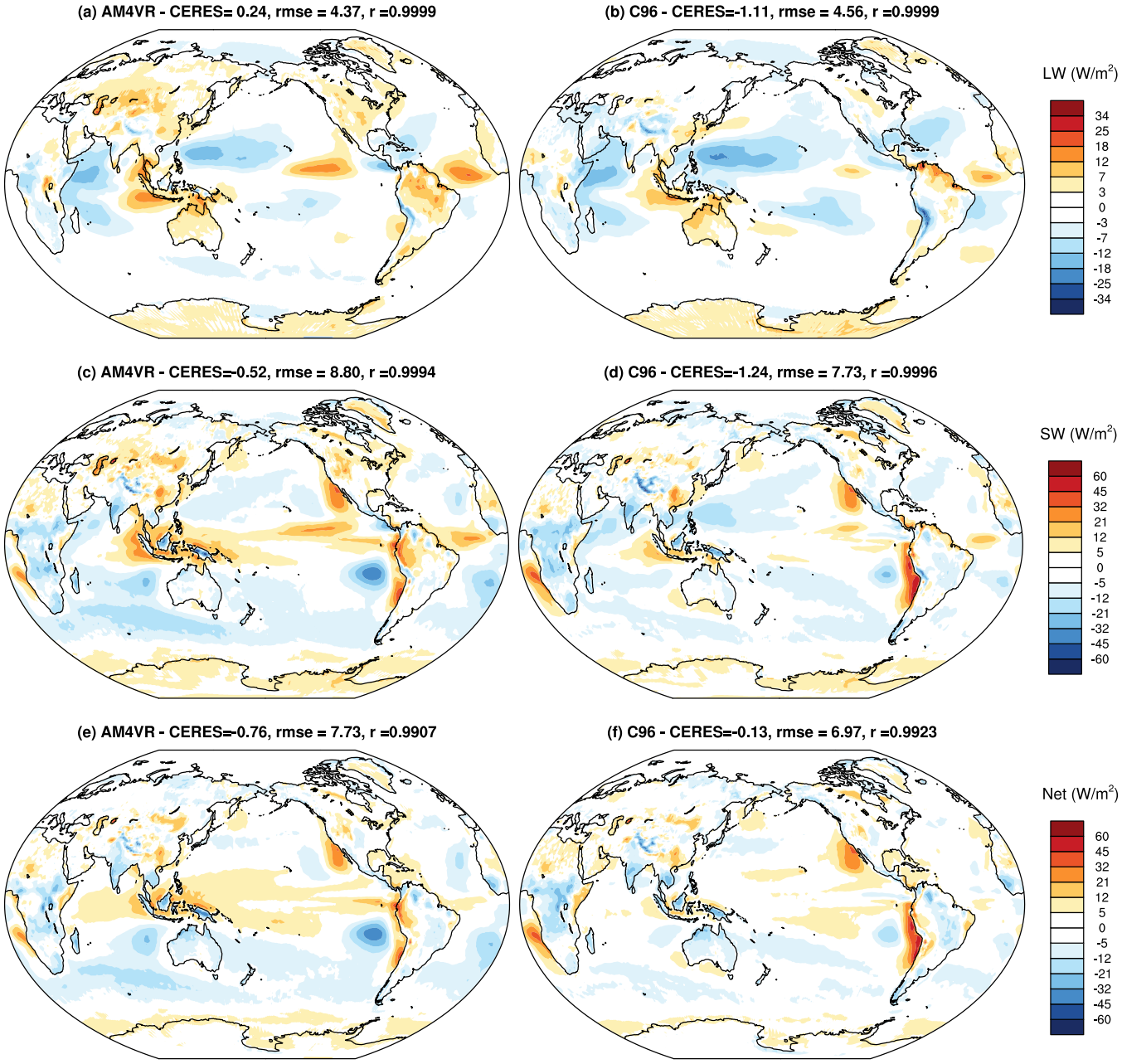

Figure 6. (a-f) Model bias in long-term annual mean TOA outgoing longwave radiation, shortwave absorption, and net radiative flux (W/m^2) in comparison with satellite estimates from CERES-EBAF-Ed4.2. Results are shown from AM4VR with $\epsilon_1 = 0.6$ km^{-1} and C96 with $\epsilon_1 = 0.9$ km^{-1}.
.

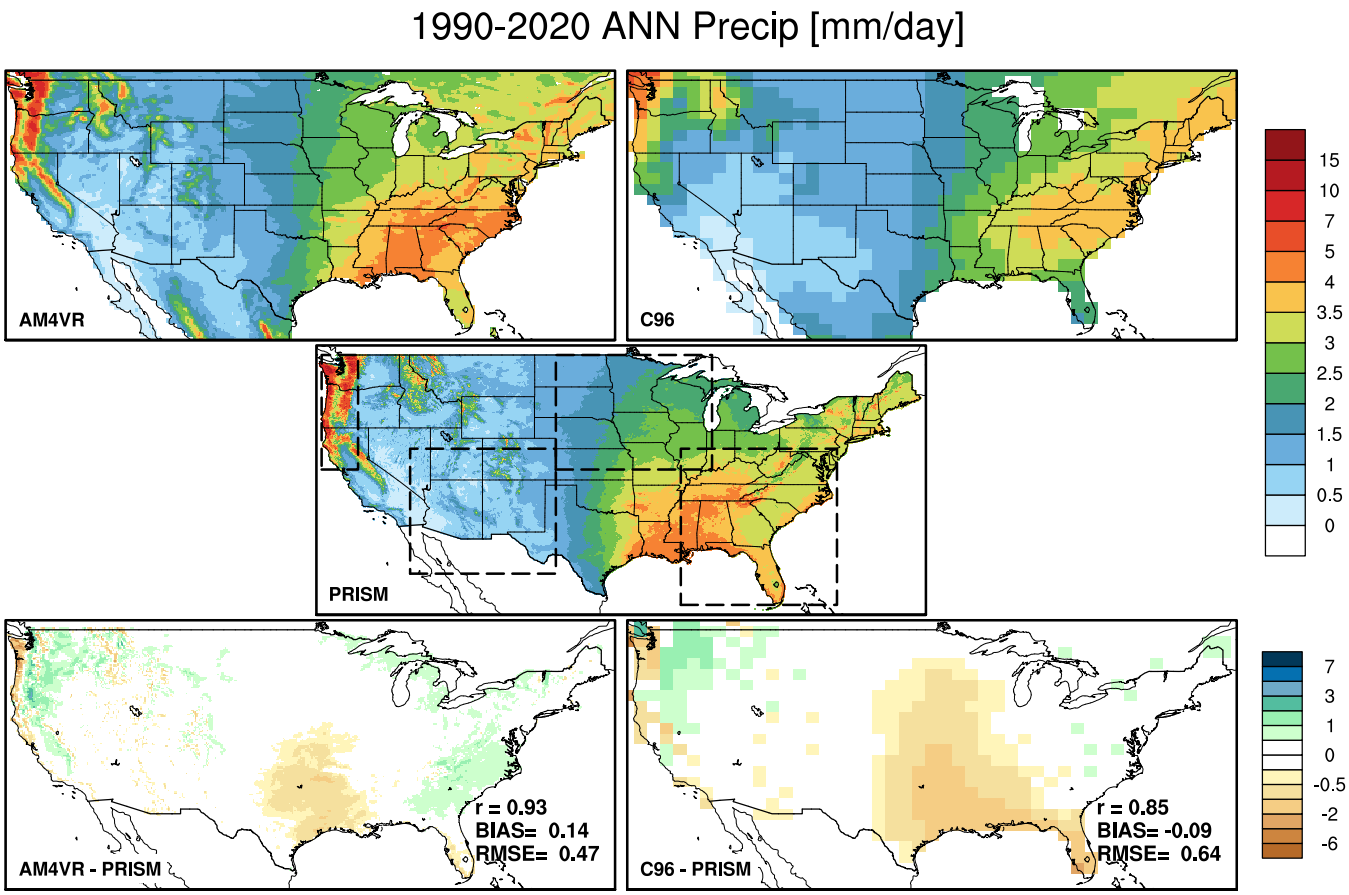

Figure 7. US annual mean precipitation (mm day^{-1}) for 1990-2020 from AM4VR (13 km, $\epsilon_1 = 0.6$ km^{-1}) and C96 (100 km, $\epsilon_1 = 0.9$ km^{-1}) AMIP simulations and PRISM observations (4 km), and differences between simulated and observed precipitation. The boxes on the PRISM map denotes select regions for analyses in Figs. 9-10.

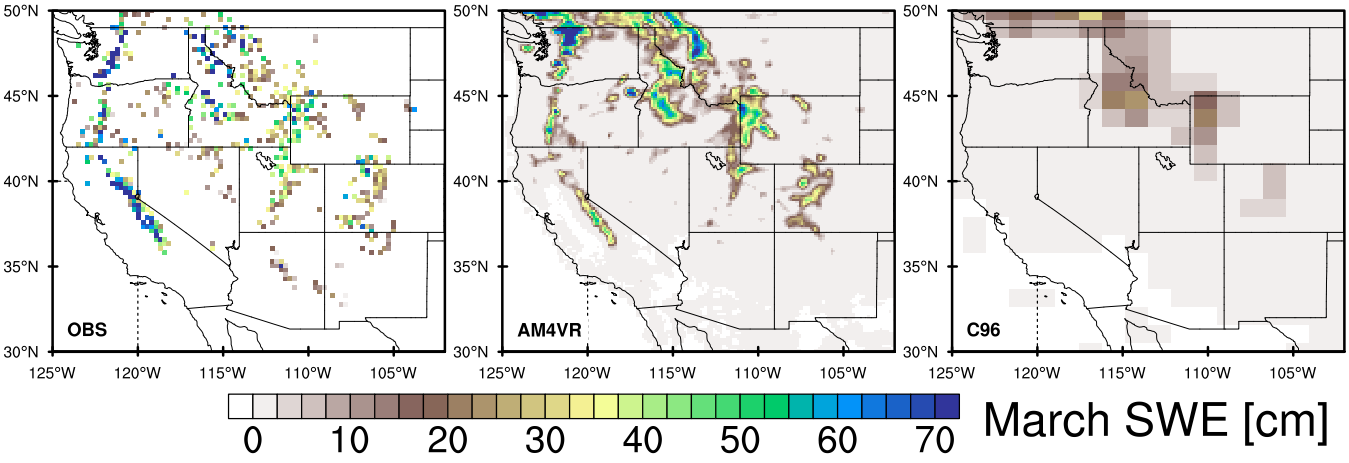

Figure 8. Long-term mean March snowpack climatology over the western US from 25 km gridded observations (Kapnick et al., 2018), AM4VR (13 km), and C96 (100 km) AMIP simulation.

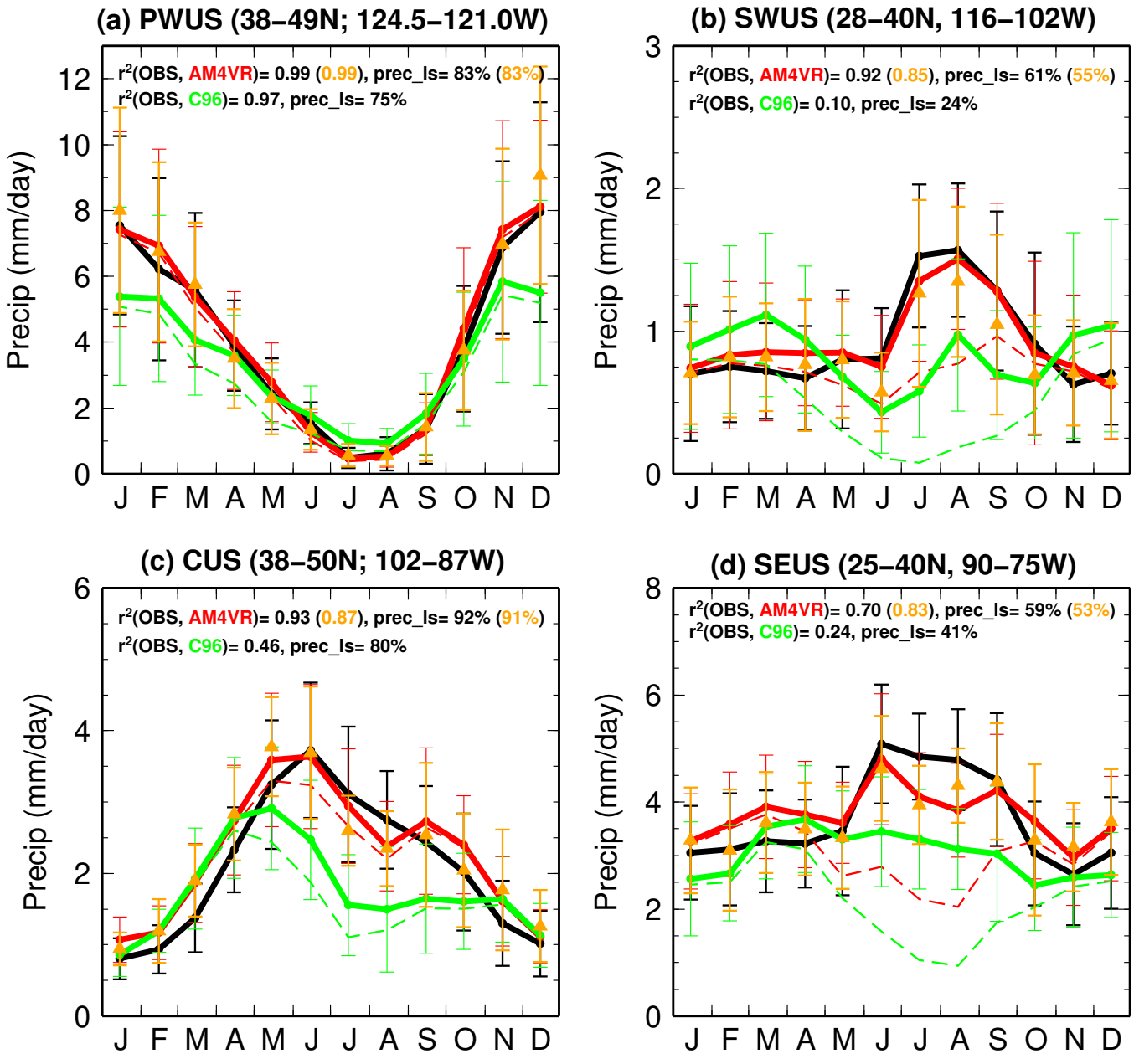

Figure 9. Monthly climatology (1990-2020) of precipitation (mm day^{-1}) from PRISM observations (black), C96 ($\epsilon_1 = 0.9$ km^{-1}, green), and AM4VR AMIP simulations with $\epsilon_1 = 0.5$ (orange) and 0.6 (red) km^{-1} for the Pacific Northwest, the Southwest. the Great Plains, and the Southeast US. The vertical bars represent interannual standard deviations. Correlatons between observed and simulated total precipitation as well as the percentage of large-scale precipitation (dashed lines) for JJAS are reported.

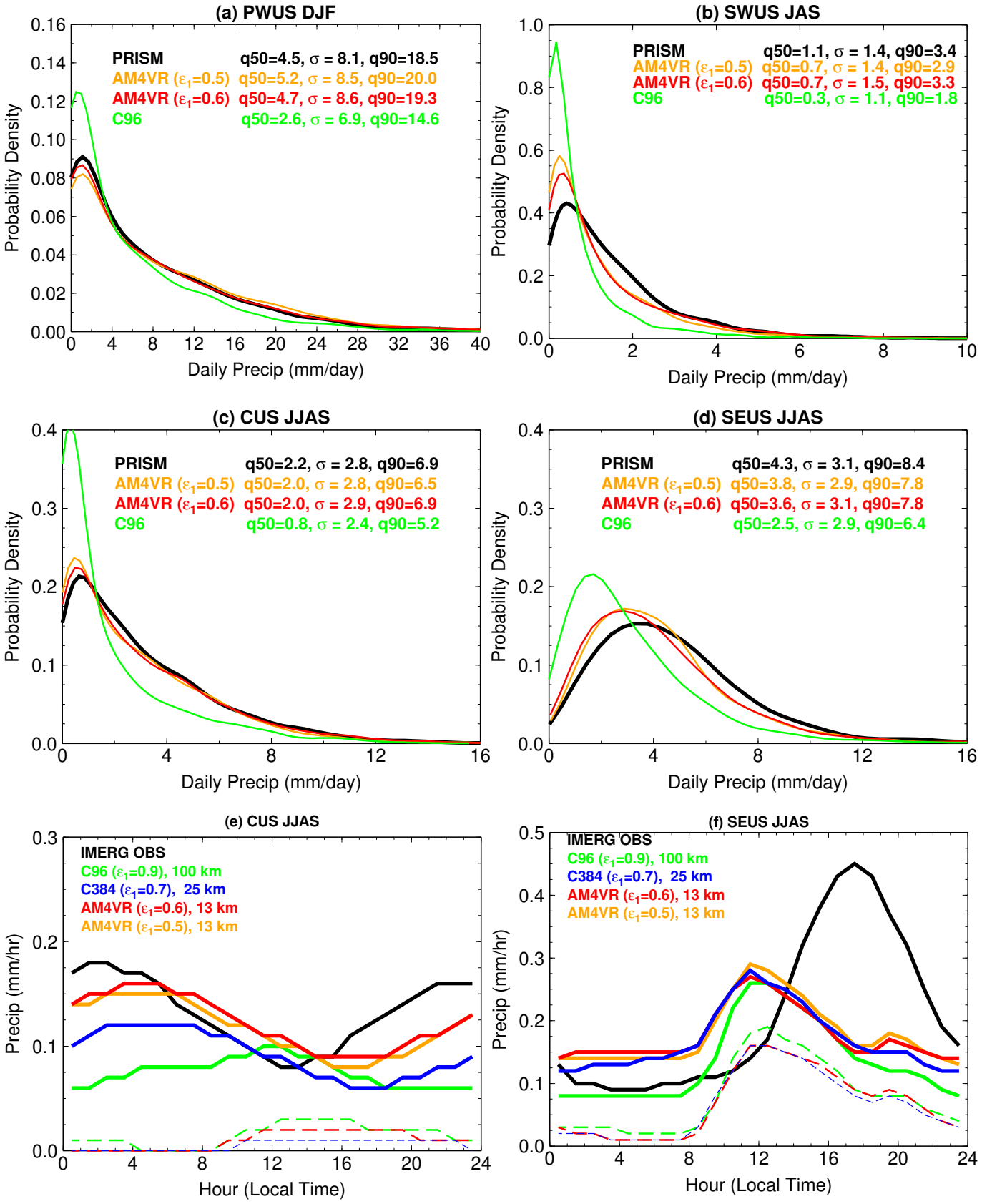

Figure 10. (a-d) Probability distribution of regionally averaged daily precipitation for the Pacific Northwest in DJF, the Southwest in JAS, and the Central and Southeast US in JJAS from PRISM observations and AMIP simulations. The median (q50), the 90th percentile (q90), and standard deviations (σ) are shown (mm day^{-1}). (e-f) Diurnal cycle of JJAS mean precipitation (mm hr^{-1}) for the Central and Southeast US from IMERG observations (black) and AM4 AMIP simulations at 100 km (green), 25 km (blue), and 13 km resolution (red and orange). The dotted lines show parameterized precipitation.

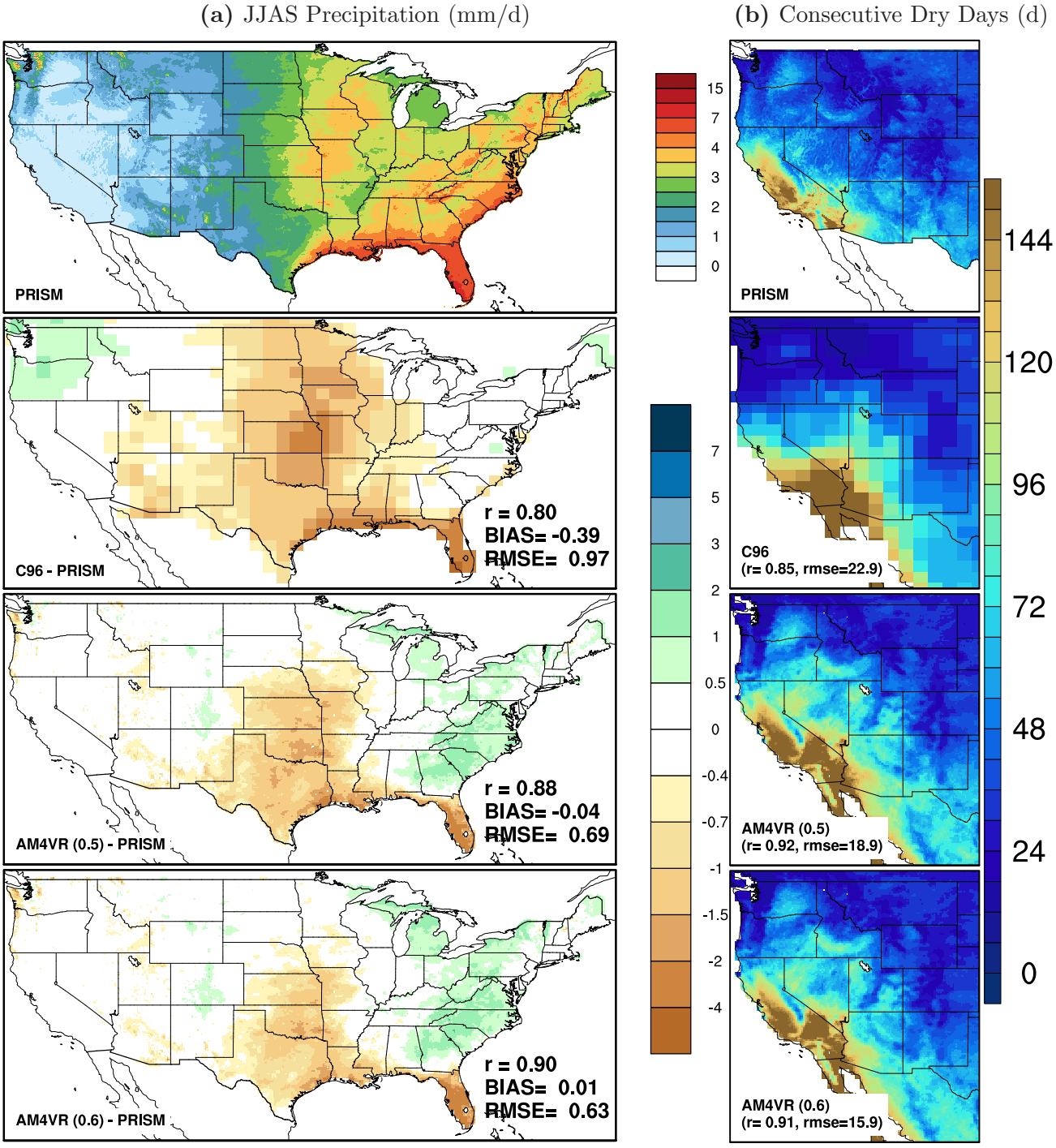

Figure 11. (Left) JJAS precipitation from PRISM observations (4 km) and model biases for C96 (100 km) and two AM4VR (13 km) AMIP simulations with $\epsilon_1 = 0.5$ and 0.6 km^{-1}, respectively; (Right) Long-term mean annual consecutive dry days calculated from PRISM and model simulations.

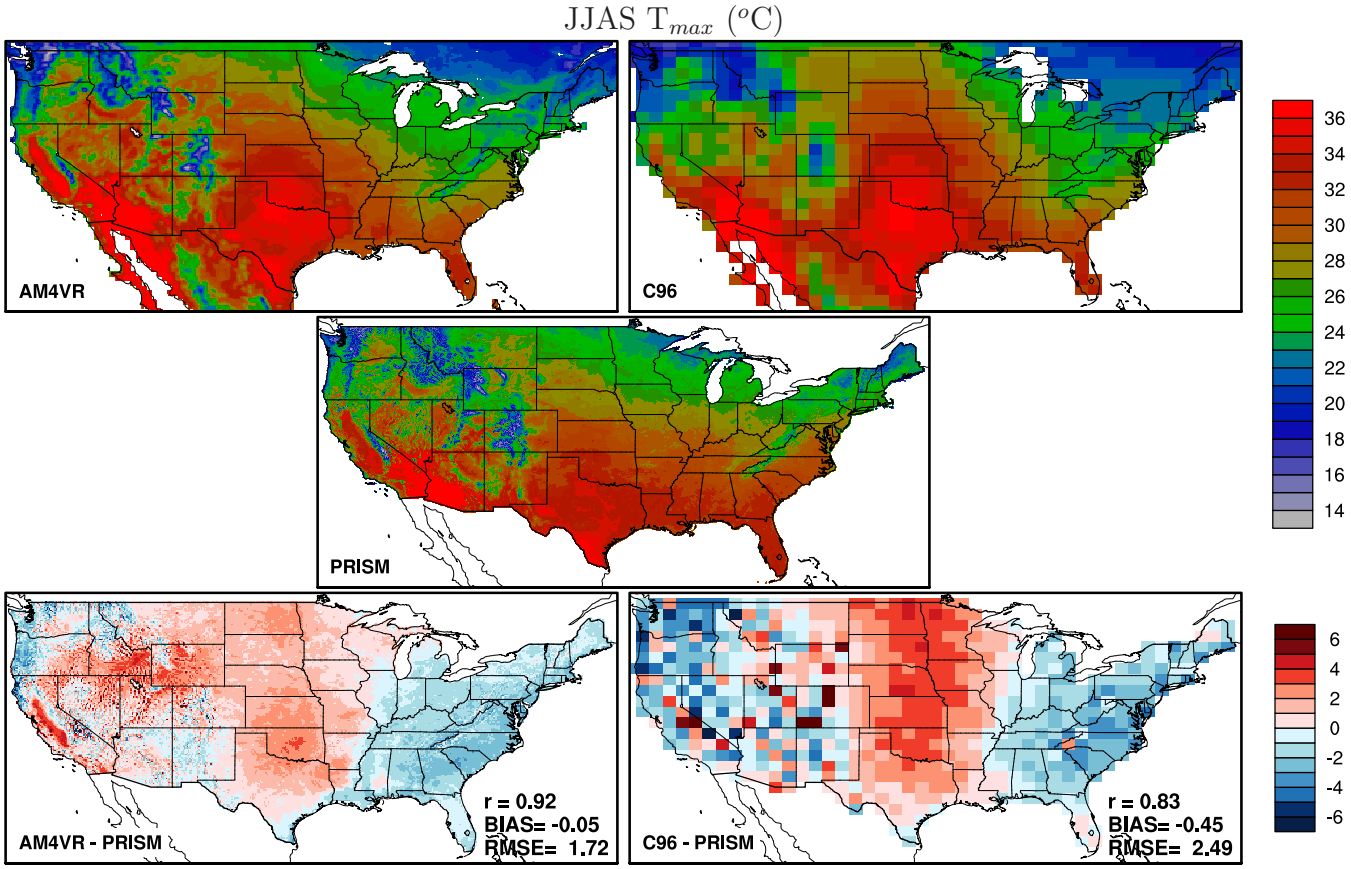

Figure 12. (Top) US JJAS mean daily maximum 2m temperature (^{o}C) for 1990-2020 from AM4VR (13 km, $\epsilon_1 = 0.6$ km^{-1}) and C96 (100 km) AMIP simulations; (Middle) PRISM observations (4 km); (Bottom) Differences between simulated and observed results.

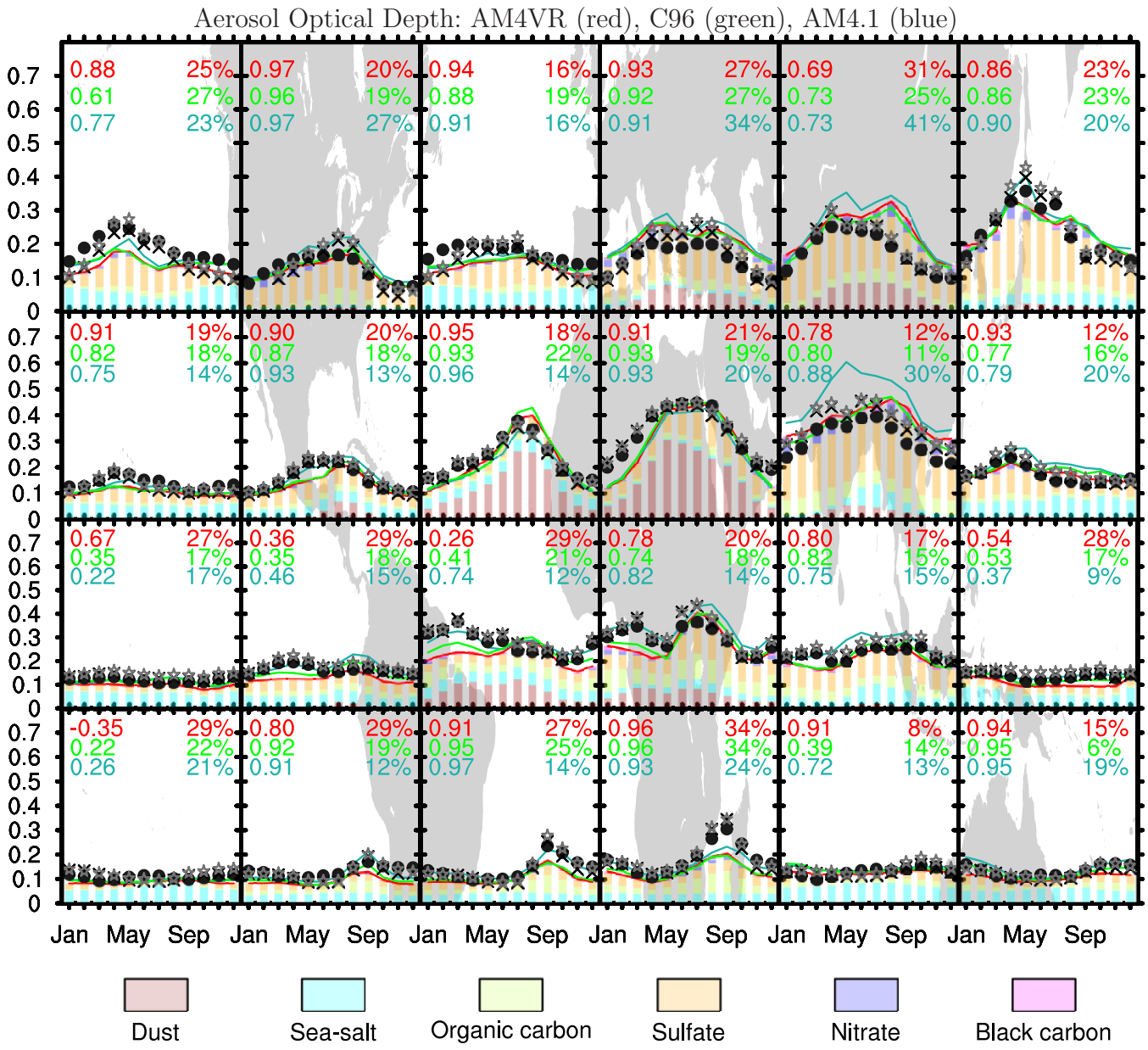

Figure 13. Monthly climatology (2000-2014) of aerosol optical depth simulated by AM4.1 (blue line), C96 (green line) and AM4VR (red line) and measured by MODIS (TERRA: star, AQUA: cross) and MISR (filled circles) satellite instruments. Each panel represents a spatial average over the corresponding region on the background map. The vertical bars represent the contribution from different aerosol components in AM4VR simulation. The numbers in each box show the correlation coefficients (left) and normalized root mean square error (right) compared to MODIS-AQUA (blue: AM4.1, green: C96, red: AM4VR).

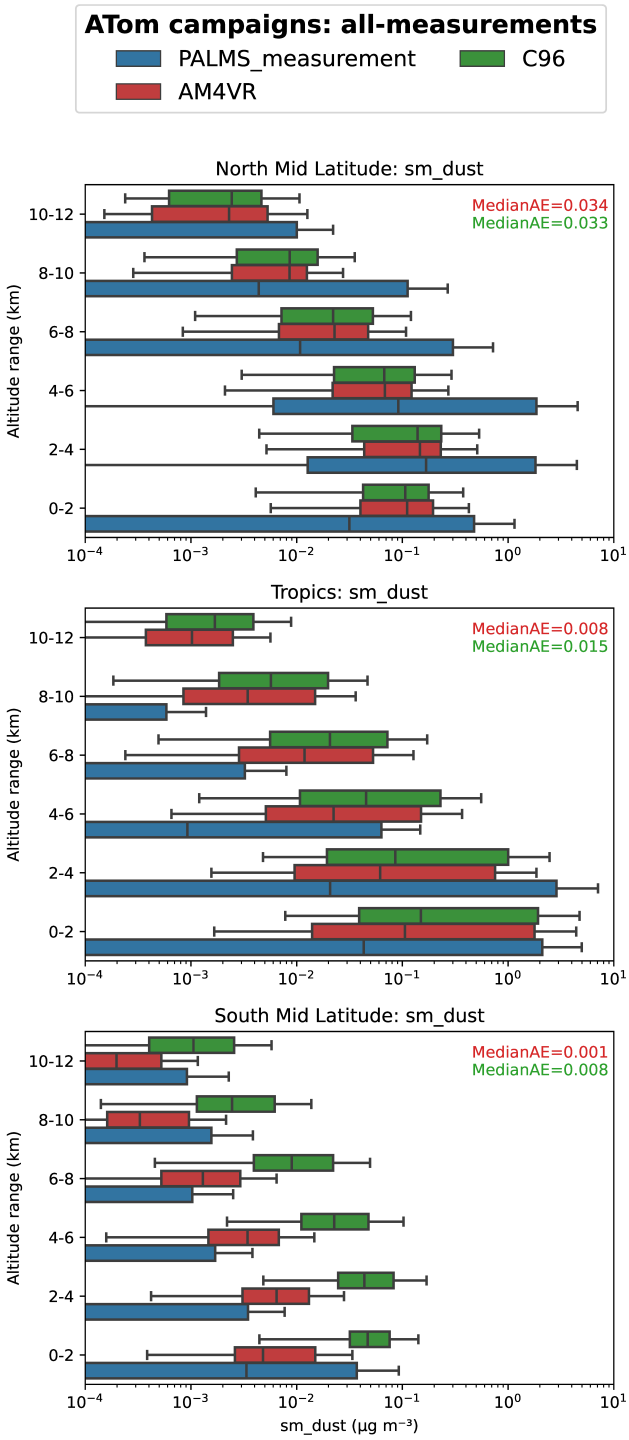

Figure 14. Comparison of fine dust vertical profiles (μg m^{-3}) from ATom aircraft measurements (blue; 2016-2018), C96 (green) and AM4VR (red) AMIP simulations (2000-2014 monthly climatology) sampled along the ATom campaigns flight track in northern mid-latitudes (30^{o}N to 60^{o}N), tropics (30^{o}S to 30^{o}N), and southern mid-latitudes (30^{o}S to 60^{o}S). The box represents the 25th percentile, median, and 75th percentile of data points for each 2 km altitude bins, and the whiskers extend to the minimum and maximum values, excluding the outliers. Median absolute error is reported.

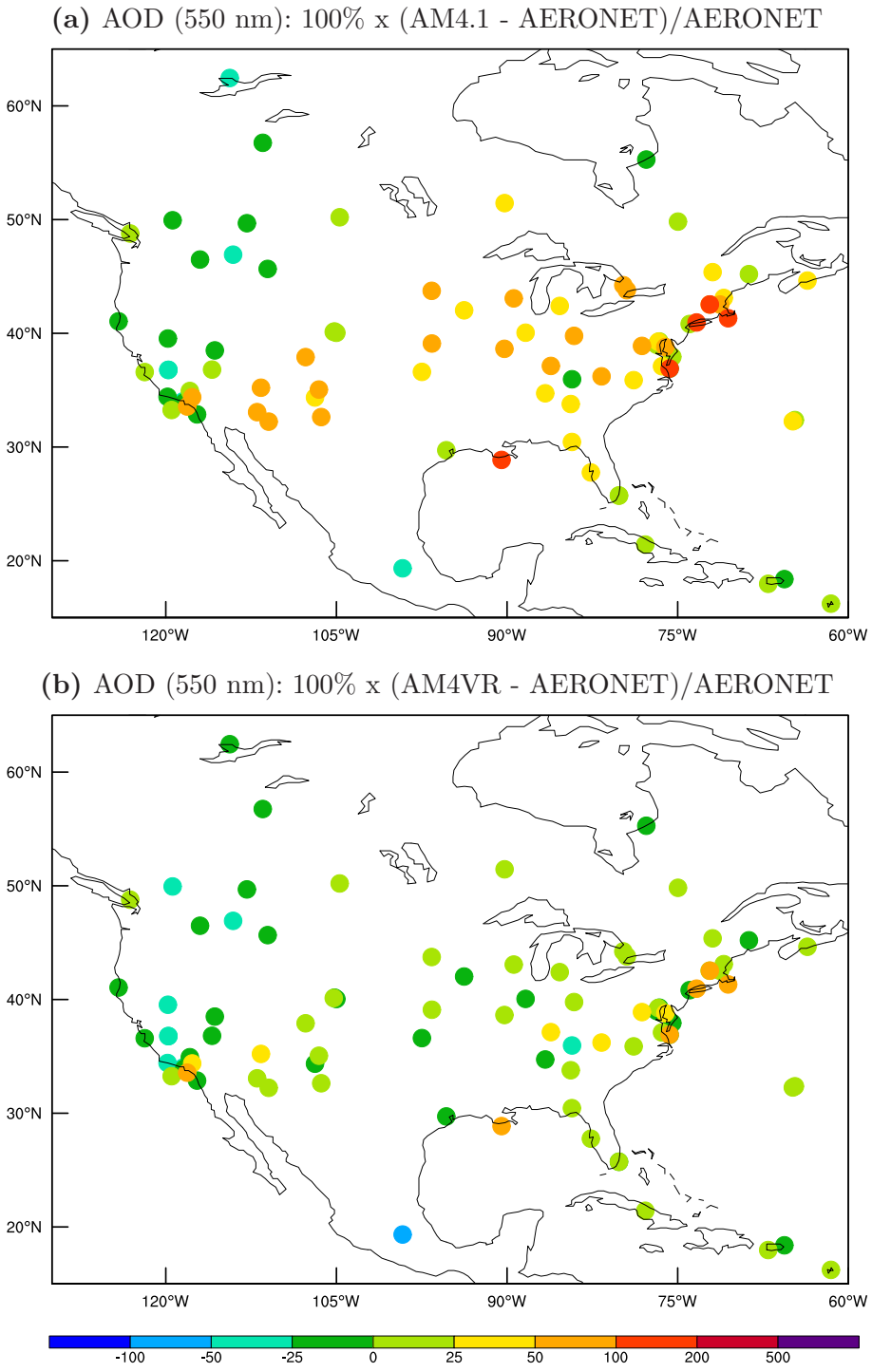

Figure 15. Comparison of simulated AOD (550 nm) with AERONET observations over the 2000-2014 period for AM4.1 and AM4VR AMIP simulation. Sites with at least 5 years of observations are shown.

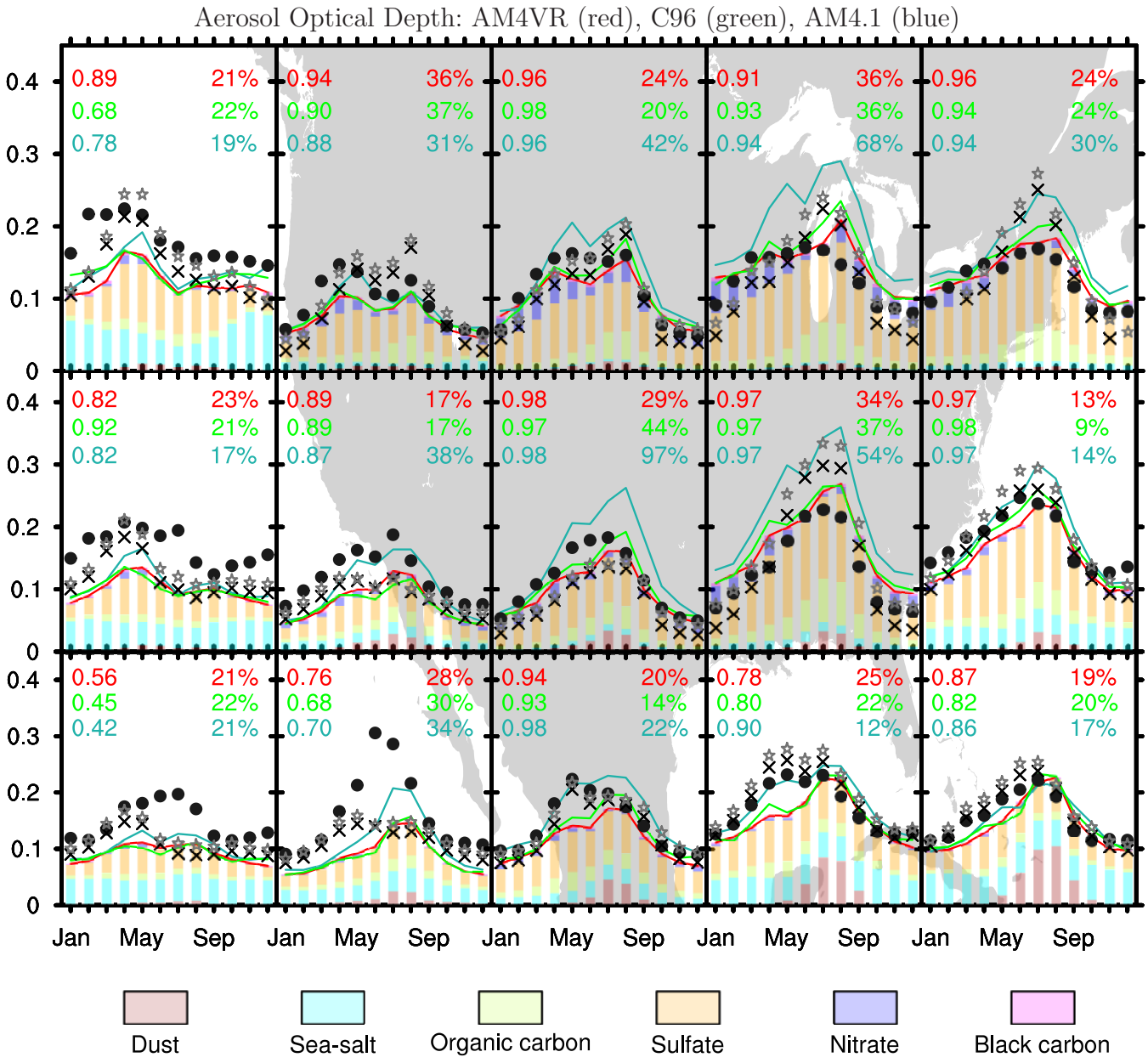

Figure 16. As in Fig. 13 but for CONUS.

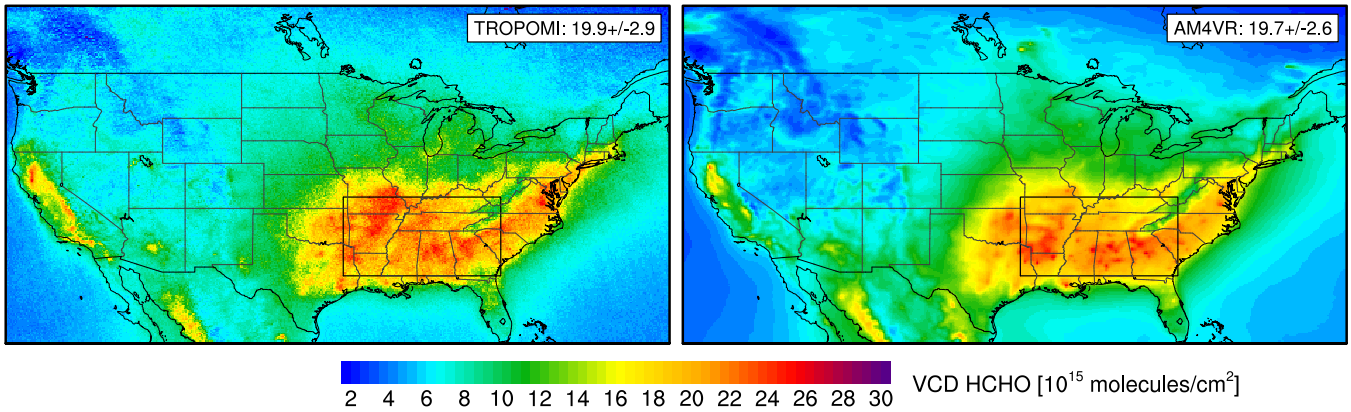

Figure 17. Tropospheric HCHO columns during JJA 2018-2020 retrieved from TROPOMI (bias-corrected, regridded to 13 km) and computed from AM4VR (nudged, 13km) sampled on TROPOMI overpass time (1:30PM). The mean value over the SEUS (box on map), as well as standard deviation across the nine months in JJA 2018-2020, is reported on each graph.

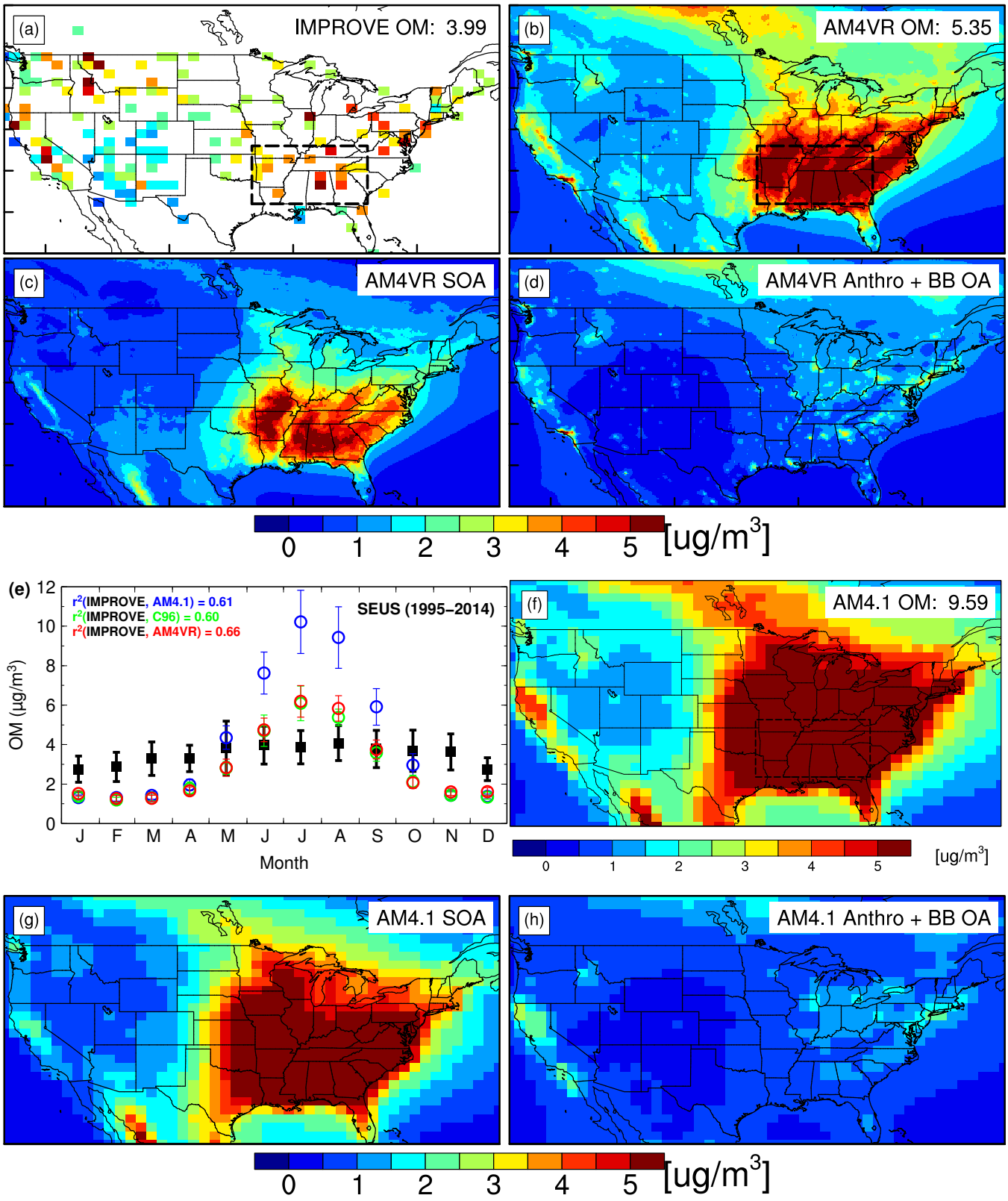

Figure 18. JJA mean surface organic matter (OM) concentrations (μg m^{-3}) for 1995-2014 from IMPROVE observations, AM4VR and AM4.1 simulations (a,b,f), along with the simulated contributions from biogenic precursors (c,g) and from anthropogenic and biomass burning emissions (d,h). Also shown is observed and simulated monthly climatology (1995-2014) of OM for the southeast US (box on map), with the vertical bars representing interannual standard deviations (e). JJA mean values for the Southeast are reported on the top right corner of (a), (b), and (f).

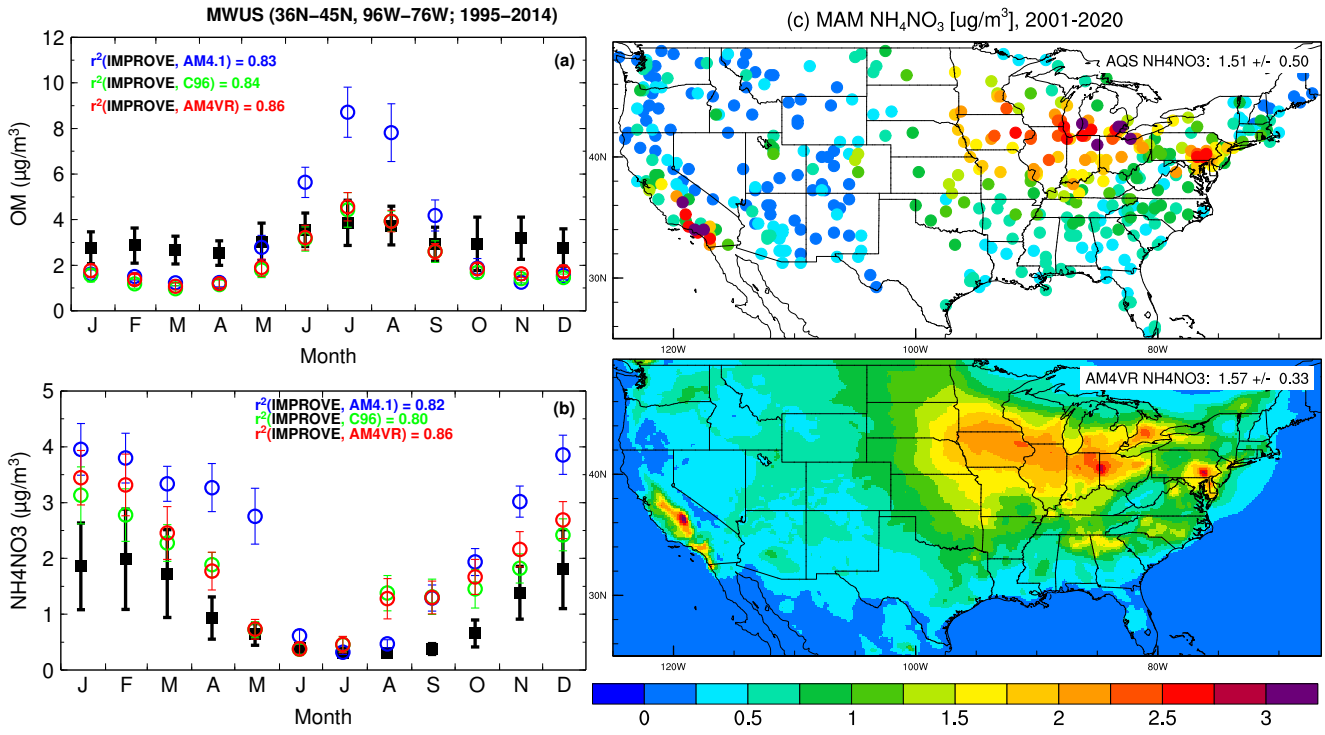

Figure 19. (a-b) Monthly climatology (1995-2014) of surface organic and NH_4NO_3 aerosol concentrations in the Midwest US from IMPROVE observations and model simulations. The vertical bars represent interannual standard deviation. (c) Springtime climatology of surface NH_4NO_3 aerosol concentrations from AQS observations and AM4VR simulation.

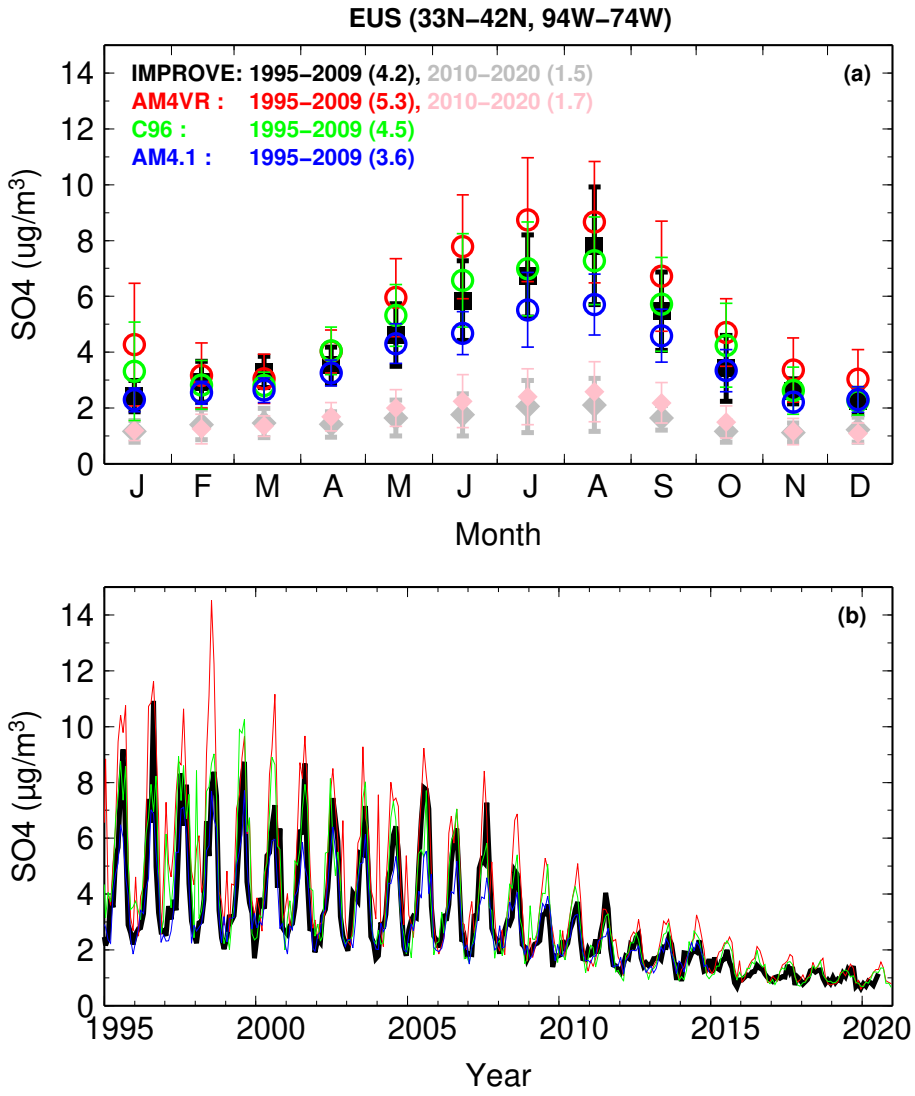

Figure 20. (a) Monthly climatology of surface sulfate concentrations for 1995-2009 versus 2010-2020 from IMPROVE observations and AM4VR simulations. Results from C96 and AM4.1 for the 1995-2009 period are also shown for comparison. (b) Time series of monthly mean sulfate concentrations from 1995 to 2020 from observations and model simulations.

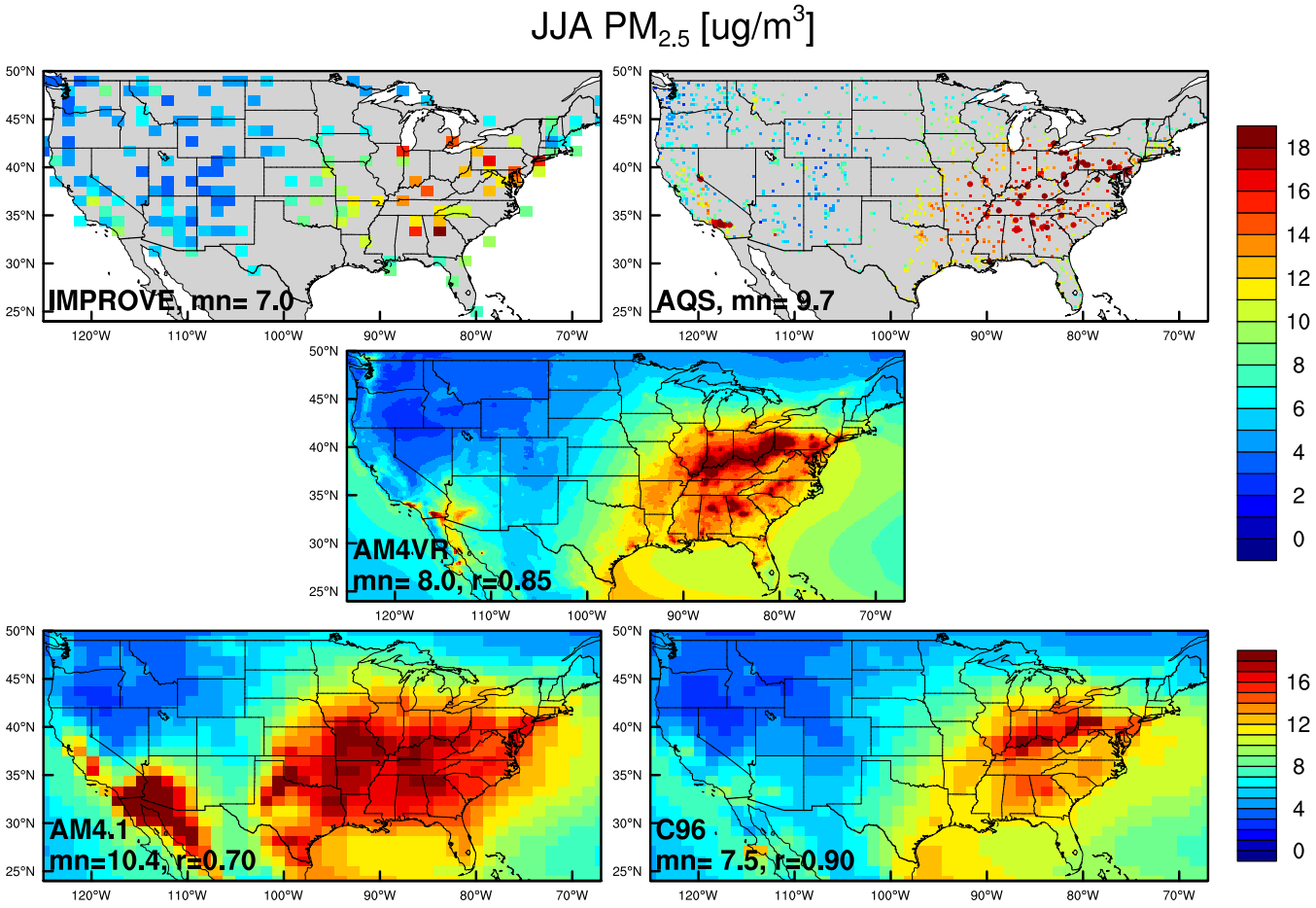

Figure 21. Summer $PM_{2.5}$ concentrations in US surface air averaged over 2000-2014 from IMPROVE and AQS observations and from model simulations. The observed-model correlations (r) and means (mn) sampled at IMPROVE sites are reported. For illustrative purposes, AQS sites with $PM_{2.5}$ greater than 17 $\mu g/m^3$ are ploted as larger circles.

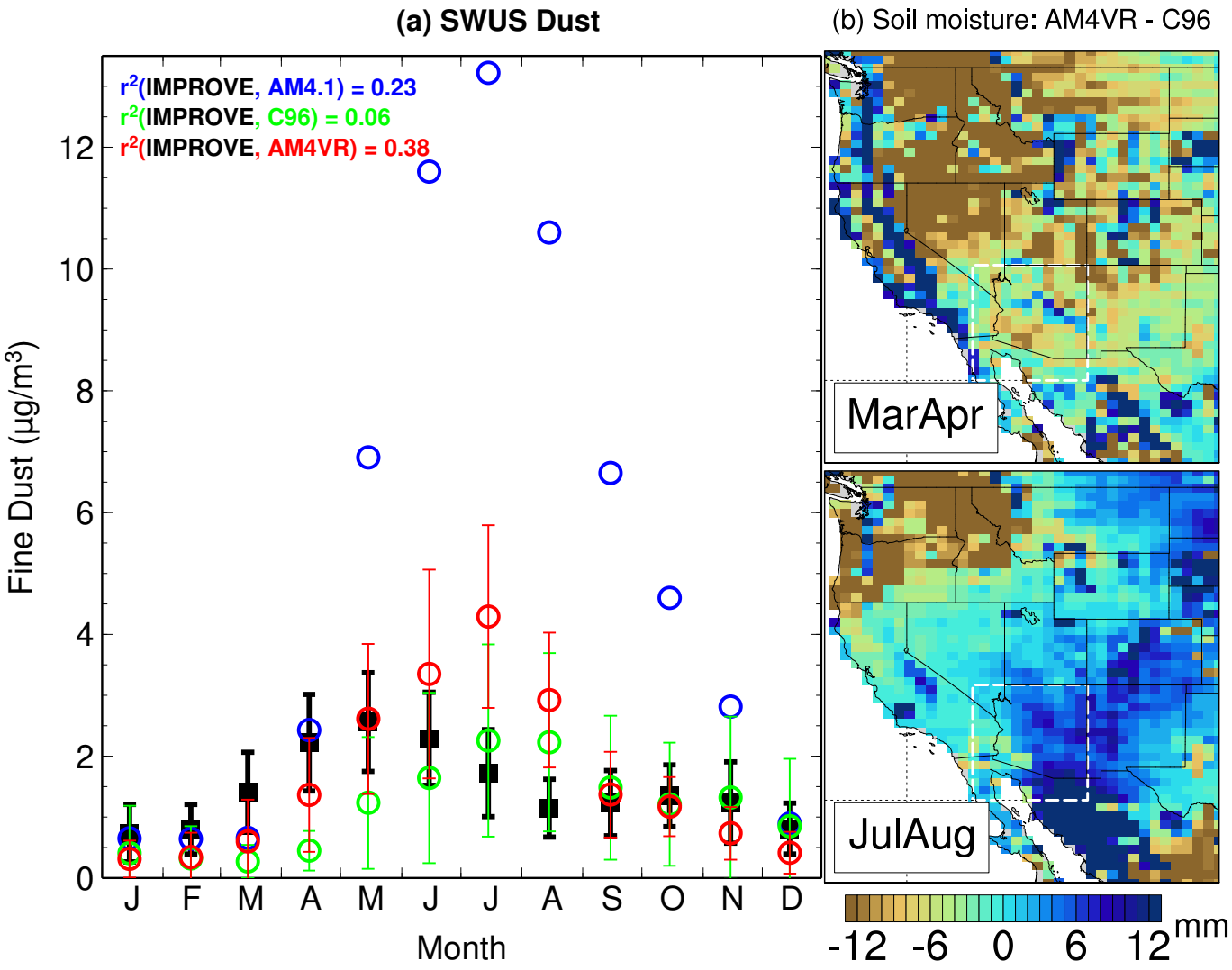

Figure 22. (a) Monthly climatology (1995-2014) of surface fine dust concentrations at IMPROVE sites in Arizona (box on map) from observations and model simulations. The vertical bars represent interannual standard deviation. (b) Difference in top 15-cm soil moisture between AM4VR and C96 (regridded to 50 km for comparison) for March-April and July-August.

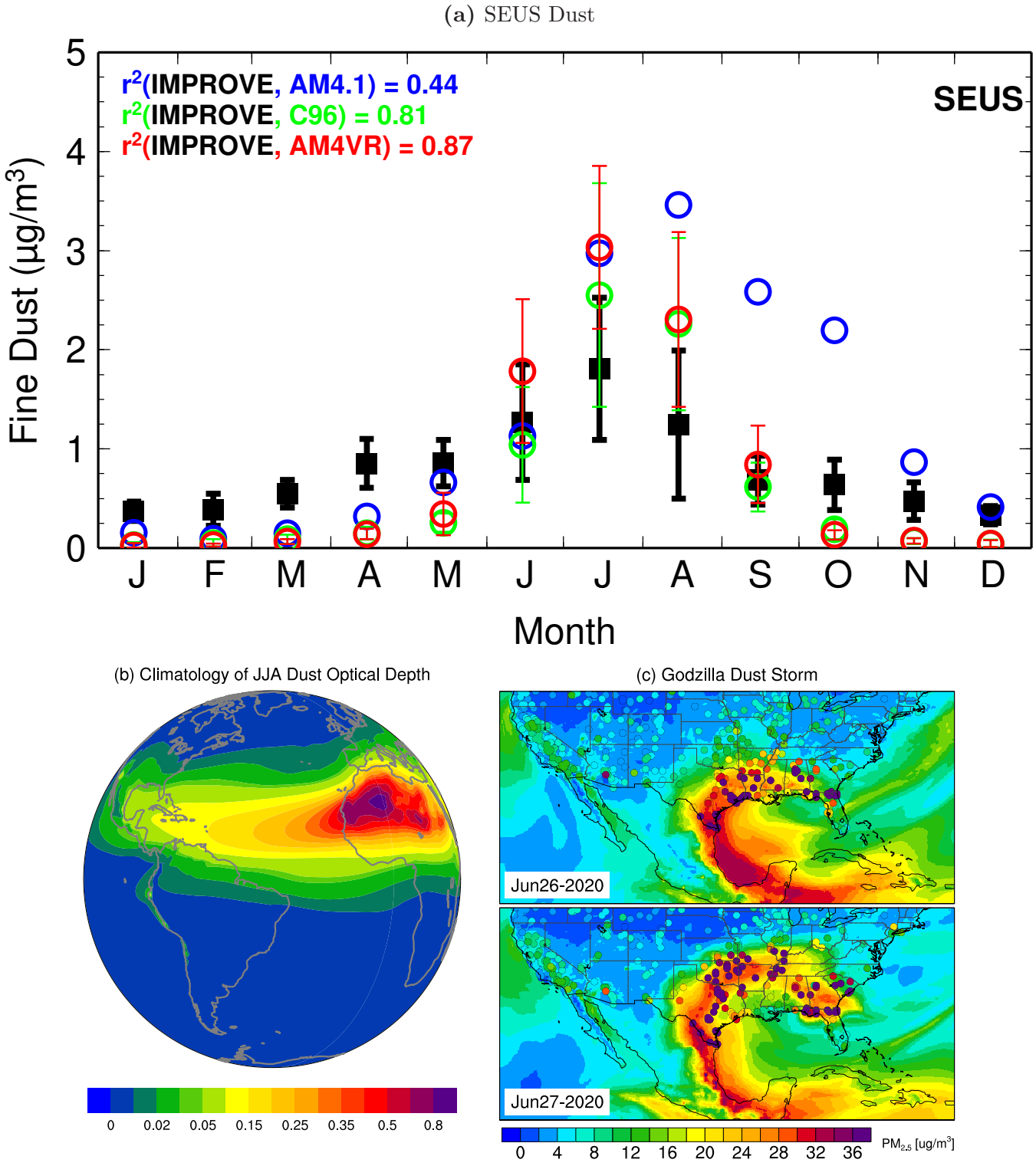

Figure 23. (a) Monthly climatology (1995-2014) of surface fine dust concentrations in the Southeast US from IMPROVE observations and AMIP simulations with AM4.1, C96, and AM4VR. The vertical bars represent interannual standard deviation. (b) Climatology (1990-2020) of JJA mean dust optical depth in AM4VR AMIP simulation. (c) Surface concentrations of 24-h average $PM_{2.5}$ on June 26-27, 2020 from AQS observations (filled circles) and an AM4VR nudged simulation.

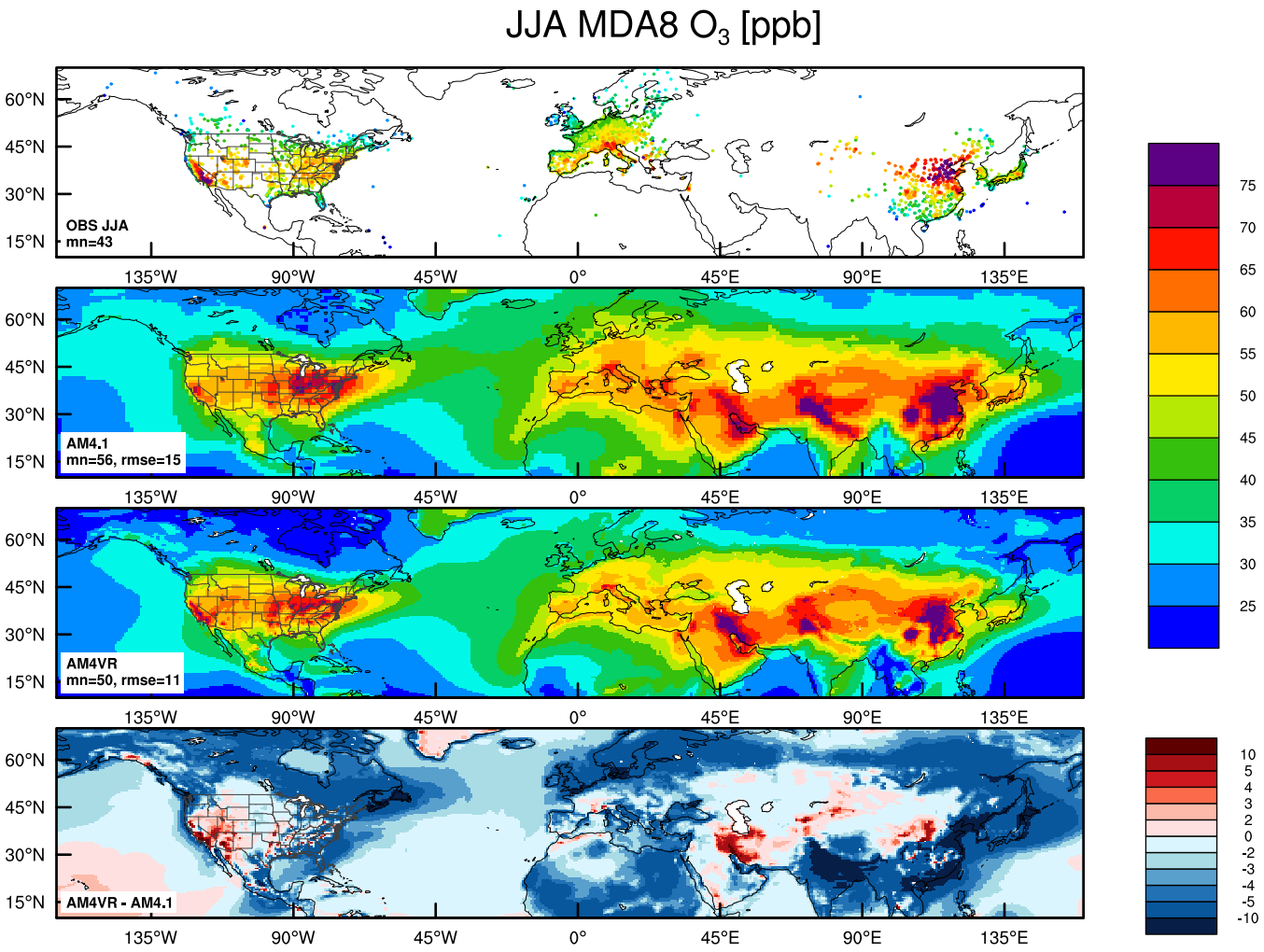

Figure 24. Summer mean surface daily maximum 8-hour average (MDA8) ozone (ppb) for the northern hemisphere from observations, AM4.1 (100 km) and AM4VR (remapped to 50 km globally) AMIP simulations (2000-2014) sampled in the lowest model layer, and differences between AM4VR and AM4.1. The rmse and model means (mn) sampled at observational sites are shown.

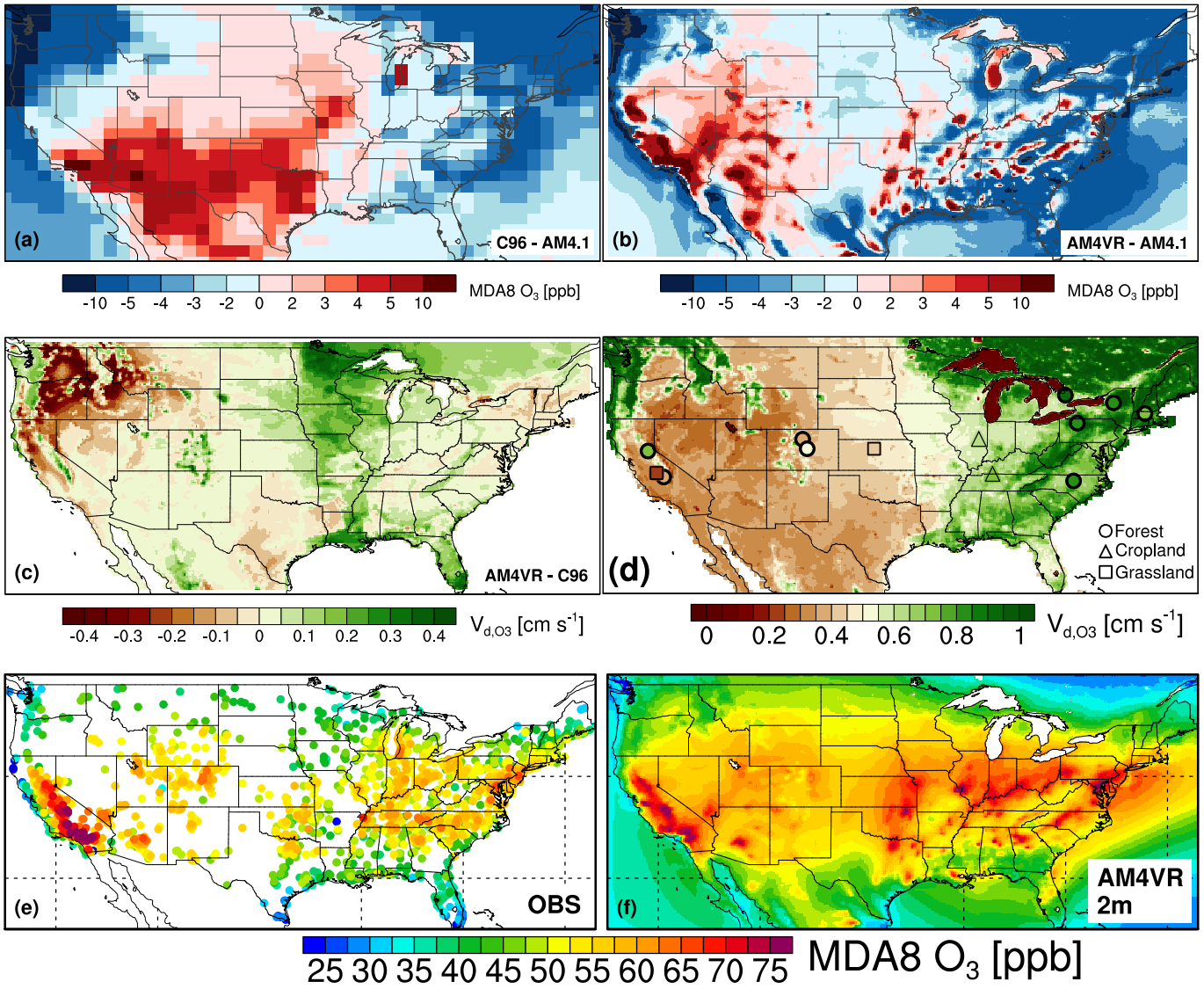

Figure 25. (a-b) Differences from AM4.1 for long-term JJA mean MDA8 ozone in C96 and AM4VR AMIP simulations sampled in the lowest model layer. (c) Differences in simulated summer daytime (9-15LT) mean ozone dry deposition velocities ($V_{d,O3}$) to secondary vegetation between AM4VR and C96 AMIP simulations. (d) Summer daytime (9-15 LT) mean $V_{d,O3}$ averaged across all land-cover types simulated in AM4VR. The color-coded symbols denote values derived from ozone flux measurements for forests (circles), croplands (triangles), and grasslands (squares). (e-f) JJA mean MDA8 ozone from AQS observations and AM4VR computed at the 2m level (Text S7).

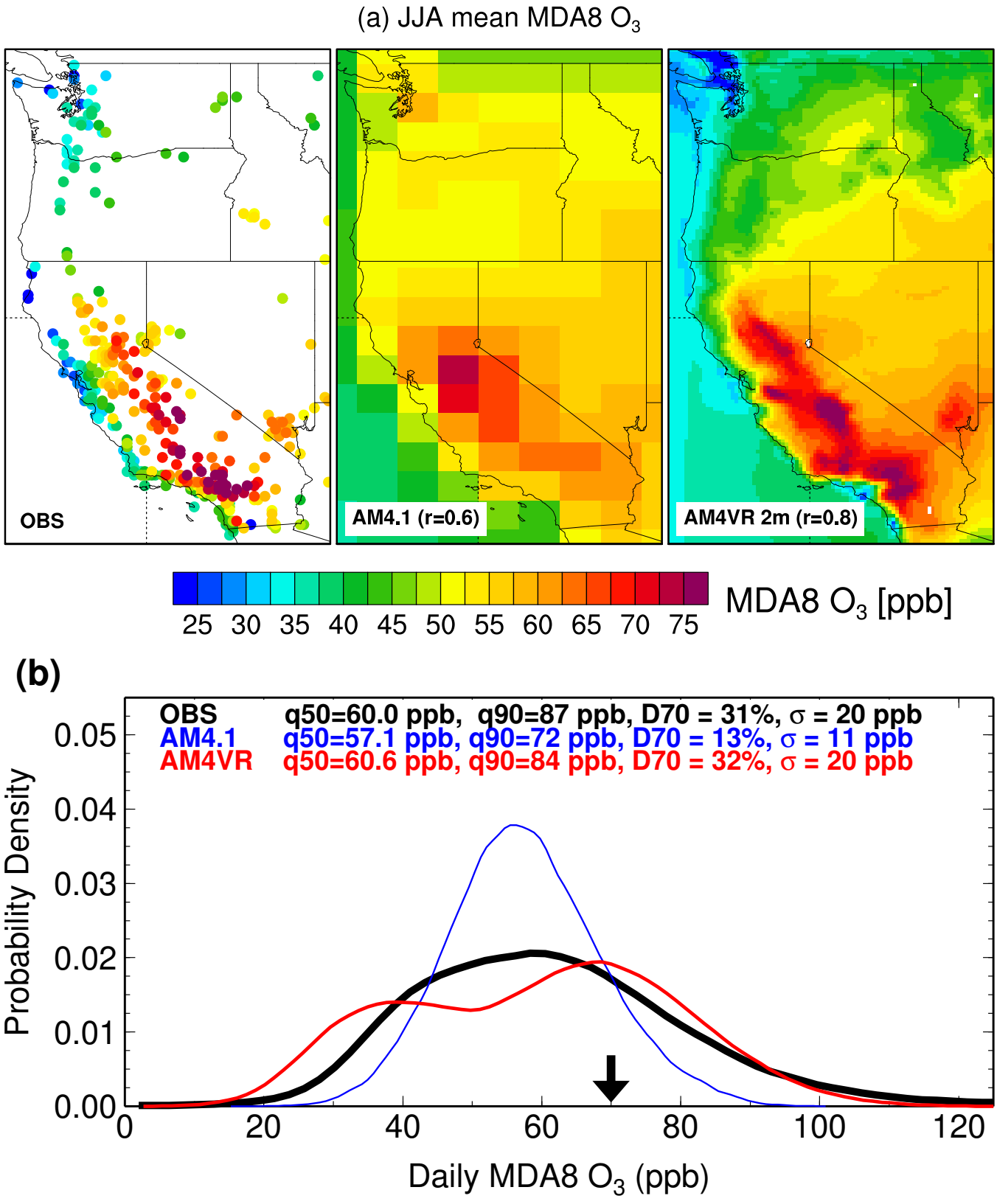

Figure 26. (a) JJA mean surface MDA8 ozone for 2000-2014 from observations, AM4.1 (100 km) sampled in the lowest model layer, and AM4VR (13 km) computed at the 2m level. Spatial correlations between observed and simulated results are reported. (b) Probability distributions for observed and simulated JJA daily MDA8 ozone sampled in the lowest model layer at sites in Southern California (32.5-37.5N; 120-114W). The median (q50), the 90th percentile (q90), standard deviation (σ), and the percentage of site-days $\geq$ 70 ppb (D70) are shown.

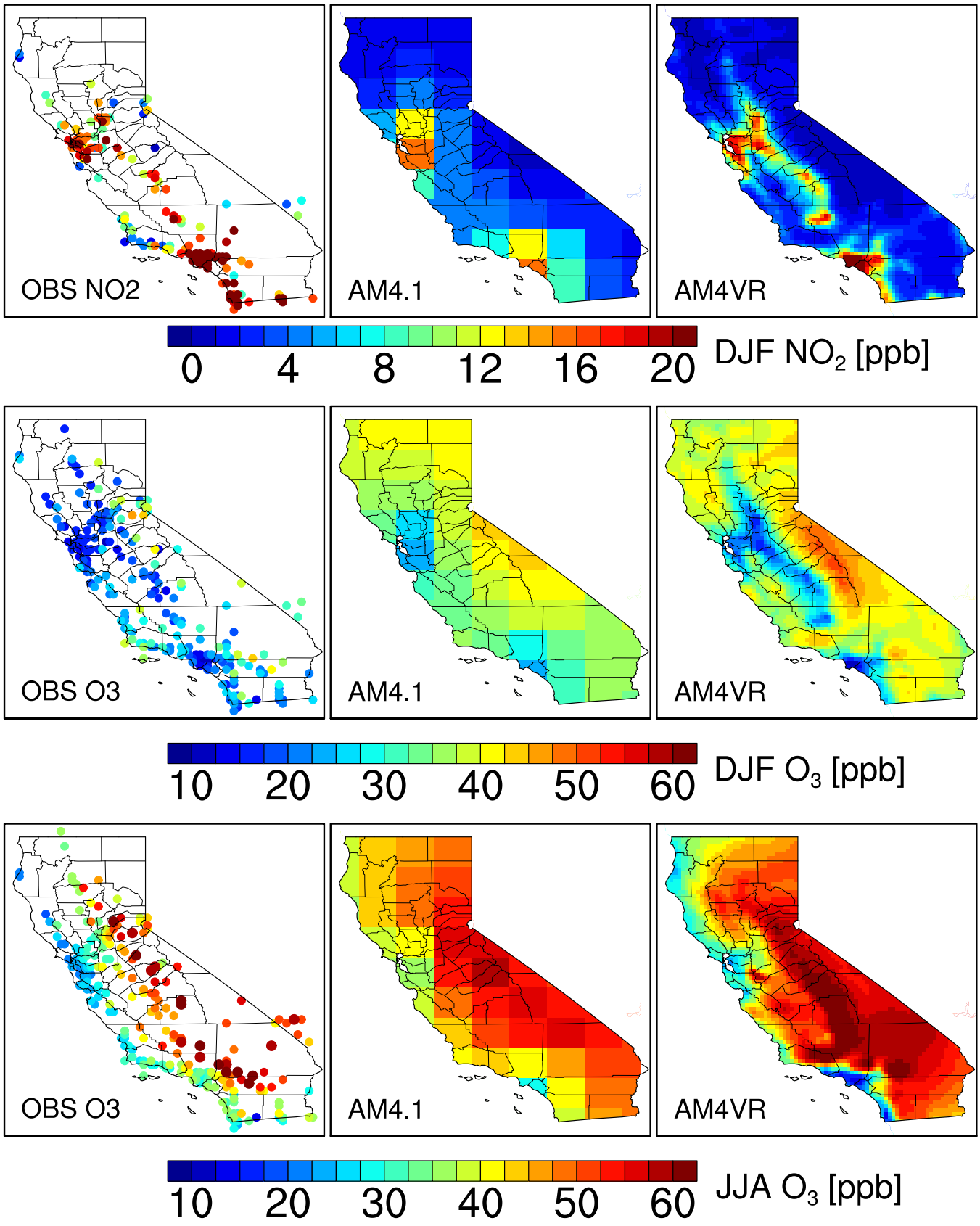

Figure 27. Surface concentrations of DJF 24-h average NO_2, DJF 24-h average ozone, and JJA 24-h average ozone in California during 2000-2014 from observations and model simulations sampled in the lowest model layer.

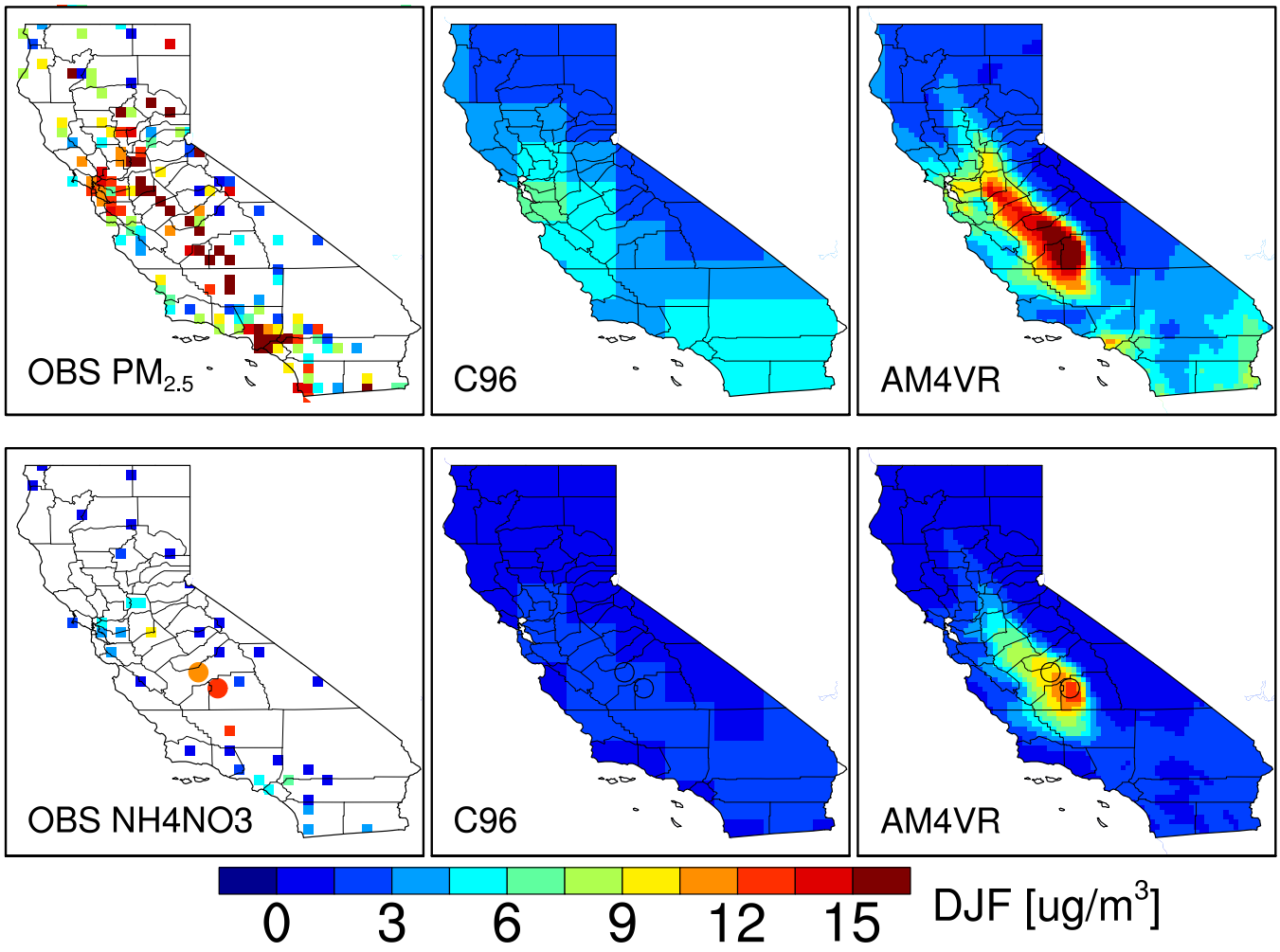

Figure 28. Wintertime (DJF) surface concentrations of total $PM_{2.5}$ and NH_4NO_3 aerosols in California during 2000-2020 from observations (25 km), C96 (100 km) and AM4VR (13 km) AMIP simulations. The circles denote locations of Fresno and Visalia analysed in Fig. 29.

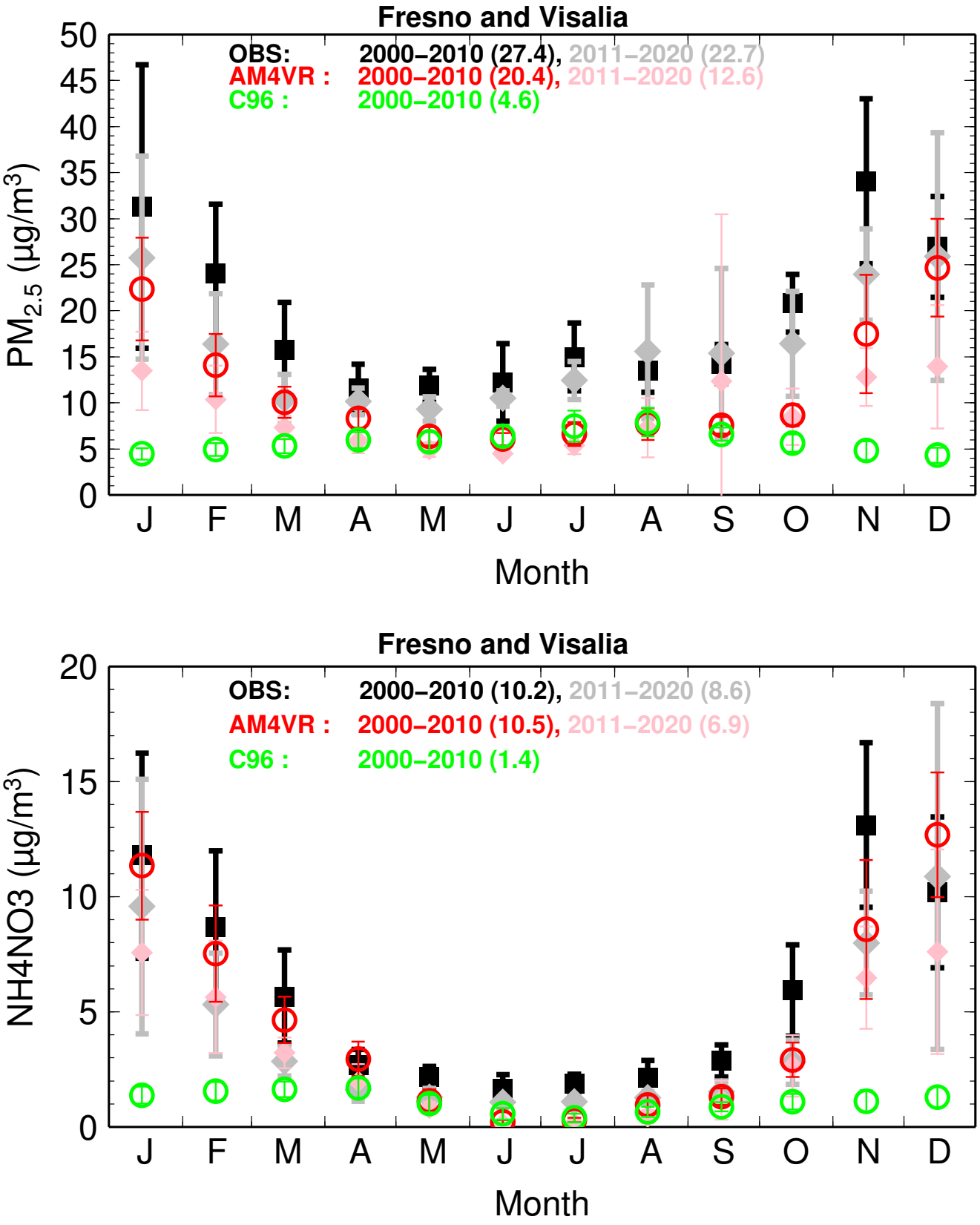

Figure 29. Monthly mean $PM_{2.5}$ and NH_4NO_3 aerosols sampled at Fresno and Visalia in the San Joaquin Valley for 2000-2010 and 2011-2020 from observations and model simulations. The vertical bars represent interannual standard deviations.

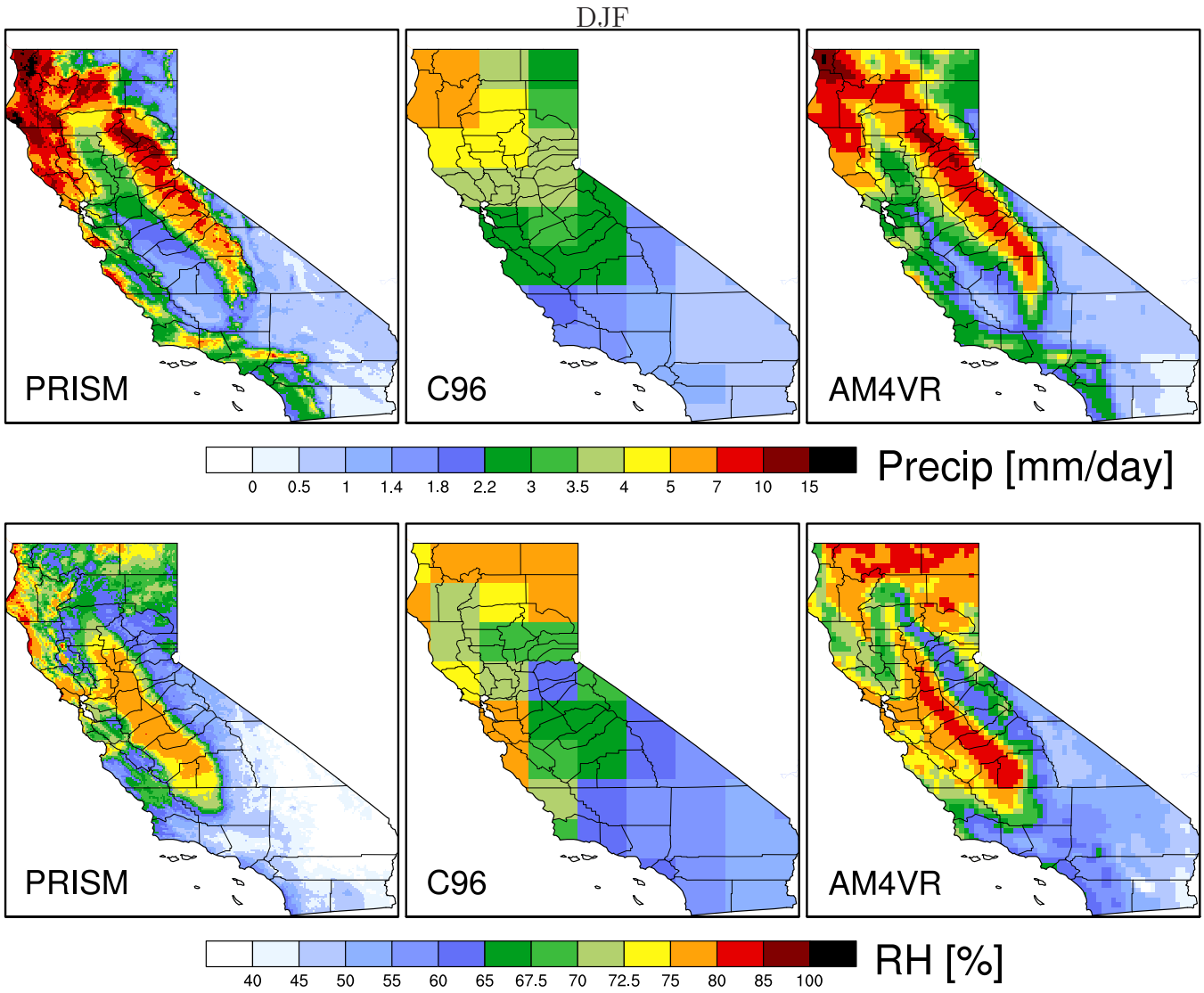

Figure 30. Wintertime (DJF) precipitation and 2 m relative humidity in California averaged over 1990-2020 from PRISM observation-based estimates (4 km), C96 (100 km) and AM4VR (13 km) AMIP simulations.